# Biomechanical graph matching for hepatic intra-operative image registration

Jaime Garcia Guevara

## To cite this version:

Jaime Garcia Guevara. Biomechanical graph matching for hepatic intra-operative image registration. Computer Vision and Pattern Recognition [cs.CV]. Universite de Lorraine, 2019. English. NNT : 2019LORR0238 . tel-02408339

HAL Id: tel-02408339
https://hal.science/tel-02408339v1

Submitted on 13 Dec 2019

École doctorale IAEM Lorraine

# Biomechanical graph matching for hepatic intra-operative image registration

## THÈSE

présentée et soutenue publiquement le 2 Décembre 2019

pour l'obtention du

**Doctorat de l'Université de Lorraine**
**(mention informatique)**

par

Jaime Garcia Guevara

**Composition du jury:**

| | | | |
|---|---|---|---|
| *Encadrants:* | Marie-Odile Berger | - | INRIA Equipe MAGRIT |
| | Stéphane Cotin | - | INRIA Equipe MIMESIS |
| *Rapporteurs:* | Patrick Clarysse | - | CNRS CREATIS (Lyon) |
| | Stephanie Speidel | - | National Center for Tumor Diseases (NCT) |
| *Examinateurs:* | Jean-Francois Mari | - | Université de Lorraine |
| | Ingerid Reinertsen | - | SINTEF Digital, Health Research |

**Institut National de Recherche en Informatique et en Automatique - Nancy**

# Acknowledgments

I wish to thank my advisors Stéphane Cotin and Marie-Odile Berger for their continuous support and direction during my thesis. Their guidance and advice were fundamental to my work. It has been a great pleasure working with you both for the past years.

Importantly, I would like to convey my thank and gratitude to the thesis committee: Patrick Clarisse, Stephanie Speidel, Jean-Francois Mari and Ingerid Reinertsen for the time reading my thesis, useful insights and constructive questions.

I would also like to thank all my lab mates from Inria, the MIMESIS team, and the IHU Strasbourg. I have enjoyed meeting and working together with everyone. Thank you for all the support, help, and fun times.

Finally, I would like to thank my family and Anais for their love, support and encouragement. I truly would not have been able to succeed without having them by my side.

Thank you all!

# Abstract

This thesis presents the development of an automatic elastic registration method based on matching of vascular graphs extracted from both pre-operative and intra-operative images. The method can fuse accurate pre-operative information onto an organ undergoing small to large deformations during surgery, to compensate for the limited details provided by intra-operative imaging modalities and improve the visualization of tumor(s), vasculature and other important internal structures. Although methods dedicated to non-rigid graph matching exist, they are not efficient when noise, topology changes, and large intra-operative deformations are present. The first contribution presented is a biomechanical graph matching method (BGM) that builds on the work of Serradell et al. (2015). BGM combines the Gaussian Process Regression (GPR) matching with a biomechanical model of the organ, as a mean to discard matching hypotheses which would lead to non-plausible deformations (Garcia Guevara et al., 2018). However, BGM is not robust to noise, only matches limited size graphs and has a high computation time. The second contribution is the Adaptive Compliance Graph Matching (ACGM) method (Garcia Guevara et al., 2019), which allows to efficiently find the best graph matches with a novel compliance-based search and an adaptive rigid to soft approach. This reduces the computation time by predicting first the most plausible matching hypotheses. It also reduces the sensitivity on the search space parameters and improves the registration quality. The proposed registration methods are evaluated with realistic synthetic and real porcine datasets, showing that ACGM is compatible with intra-operative constraints.

**Keywords:** Non-rigid registration, biomechanics, data fusion, augmented reality, graph matching

# Résumé de la these

Le foie est un organe vital situé dans l'abdomen. Il s'agit d'un organe mou (sauf en cas de cirrhose), doté d'une anatomie complexe avec un réseau vasculaire dense. Le cancer du foie est la cause d'environ 780000 décès de par le monde en 2018, rangeant cette pathologie au $4^{ieme}$ rang des maladies mortelles (Bray et al., 2018).

Le traitement de ce cancer dépend de plusieurs facteurs dont le stade de la maladie, l'état de santé général du patient et la taille de la tumeur. A un stade précoce, les principales options cliniques proposées sont la chirurgie, l'ablation par radio fréquence, les techniques ablatives percutanées et la radiothérapie. Pour toutes ces options, disposer de la visualisation des vaisseaux sanguins et du foie est essentiel pour permettre au praticien un geste clinique précis en toute sécurité. Ces traitements intra-opératoires nécessitent en effet la définition d'une marge de sécurité autour de la tumeur et la connaissance des vaisseaux pouvant être coupés en préservant la fonction hépatique. Un des pré requis essentiel pour effectuer ces procédures est de disposer de moyens d'imagerie fiables et précis permettant à la fois de planifier le geste en préopératoire et de le réaliser en per-opératoire.

De manière générale, les petites lésions et les vaisseaux sont mieux identifiés dans les imageries préopératoire de type angioscanner ou IRM en raison de la résolution de ses images et de leur contraste bien supérieurs à la plupart des imageries per-opératoires (Kingham et al., 2018). Dans ce travail, les imageries per-opératoire considérées sont l'imagerie ultrasonore 3D et l'imagerie CBCT qui ne permettent cependant de visualiser que les lésions les plus grandes et partiellement l'anatomie du foie.

Chaque imagerie apportant des informations différentes et complémentaires, fusionner les images ou les structures correspondant à ces différentes imageries apporte un bénéfice important au clinicien. Depuis longtemps, le concept de réalité augmentée permettant d'ajouter des éléments détectés en pré-opératoire sur des images per-opératoires a été identifié comme un moyen prometteur pour l'assistance au geste clinique. Des applications concernant le suivi de vaisseaux, la navigation, la détection de tumeurs ont en particulier été considérées, permettant une amélioration des traitements associés (Mauri et al., 2015; Paul et al., 2015b).

En dehors des difficultés traditionnelles de recalage entre images issues de modalités différentes, une autre difficulté est liée aux déformations que peut subir l'organe pendant l'opération. Dans le cadre de chirurgies ouvertes par exemple, la procédure requiert une mobilisation complète du foie qui mène à des déformations importantes de l'organe par rapport à l'image préopératoire.

Aussi bien en chirurgie ouverte qu'en chirurgie laparoscopique, une approche fréquemment suivie consiste à recaler les données pré-opératoires sur la surface tridimensionnelle du foie, reconstruite par exemple par un dispositif stéréoscopique.

La partie visible du foie en laparoscopie est cependant petite, ce qui induit un faible nombre de d'indices images disponibles, et conduit fréquemment à des ambiguïtés ou de fortes incertitudes sur le recalage. Pour pallier à ces problèmes, des travaux ont proposé l'usage de modèles biomécaniques afin d'apporter des contraintes de nature physique dans le recalage, ce qui nécessite d'introduire des conditions aux limites sur la surface per-opératoire. Les travaux décrits dans Haouchine et al. (2015); Suwelack et al. (2014); Plantefève et al. (2016) ont ainsi montré des résultats prometteurs dans certains cas mais le problème reste mal posé en raison de la faible information de surface de l'organe disponible.

Il semble donc préférable, quand cela est possible, de considérer davantage d'informations que celles sur la surface de l'organe. Le développement d'imageries per-opératoires 3D présente ainsi beaucoup d'avantages dans l'optique de pouvoir recaler avec plus d'informations et donc plus de précision les images pré et per-operatoires. Des systèmes récents pour l'aide au geste dans le foie ont ainsi montré leur capacité à identifier des tumeurs. Ces systèmes sont cependant incapables à l'heure actuelle de prendre en compte de grandes déformations de l'organe, ce qui réduit leur usage.

Idéalement, on attend d'une procédure de recalage du foie qu'elle soit capable de prendre en compte de grandes déformations et qu'elle soit robuste à la présence d'inhomogénéités dans l'intensité et à la présence d'artefacts. Elle devrait pouvoir être utilisée avec les imageries 3D couramment utilisées (ultrason 3D, CBCT, IRM, angioscanner) et être entièrement automatisée, sans besoin d'une estimée initiale, d'un capteur ou d'interaction avec l'utilisateur. Enfin, le recalage doit être assez rapide pour être compatible avec le workflow clinique. De façon générale, ce temps devrait être inférieur ou égal au temps d'acquisition de l'image per-opératoire Mauri et al. (2015).

Le recalage d'images consiste à établir des correspondances spatiales entre différentes acquisitions et à trouver la transformation optimale permettant de passer d'une image à l'autre. Le choix d'une méthode de recalage dépend la plupart du temps des modalités d'images utilisées et de leurs conditions d'acquisition. Le recalage multi-modalité dans lequel les intensités des pixels ou voxels n'ont pas la même signification physique est évidemment plus complexe. De plus, les images per-opératoires ont la plupart du temps un champ de vue réduit, présentent davantage d'artefacts et un rapport signal/bruit plus faible en raison des conditions d'acquisition non optimales.

Le foie peut subir de grandes déformations par rapport à l'imagerie pré-operatoire lors de gestes cliniques, par exemple lorsque le patient est positionné sur le coté ou lors de l'insufflation de gaz en laparoscopie. La nature de la déformation conditionne évidemment le type de méthodes à mettre en oeuvre pour le recalage (Sotiras et al., 2013). Les modèles de diffusion, les modèles de type plaques minces, ou les modèles basées sur des B-splines ou des modèles biomécaniques sont couramment employés. Les modèles basés sur la diffusion sont des modèles non paramétriques régularisés par l'application d'un filtre gaussien permettant de générer un champ de déplacement lisse (Vercauteren et al., 2009). Ils ont été utilisés en recalage multi-modalité par Heinrich et al. (2012) conjointement avec un descripteur de voisinage MIND relativement indépendant de la modalité, ainsi que dans Reaungamornrat et al. (2016) dans le cadre d'un recalage multi-modalité pour la colonne vertébrale. Les modèles de type free-form deformation sont courants en recalage et permettent de calculer un champ lisse de déformations avec un nombre réduit de degrés de liberté. Ils ont par exemple été utilisés dans (Rueckert et al., 1999) couplé avec des B-splines cubiques. Ils ont également été utilisés avec des métriques de similarité diverses telles que l'information mutuelle (Klein et al., 2008), ou des variantes du rapport de corrélation (Rivaz et al., 2015; Fuerst et al., 2014). En pratique, ces méthodes ne sont cependant pas utilisées dans le cadre de grandes déformations ni pour des imageries per-opératoires bruitées.

Les déformations que subit un organe pendant une intervention peuvent être larges et de nature complexe. Les modèles intègrent donc un nombre élevé de degrés de liberté pour prendre en compte cette complexité. Cependant le champ réduit en laparoscopie ainsi que le rapport signal/bruit élevé ne permettent pas l'extraction d'indices en nombre suffisant pour déterminer correctement les paramètres du modèle. Les modèles de transformation cités précédemment ne prennent par ailleurs pas en compte les propriétés physiques des organes et notamment l'hétérogénéité ou l'anisotropie des tissus. Dans l'optique de générer des solutions plausibles, des modèles de mouvements dédiés ou des atlas statistiques de forme ont été proposés (Peters et Cleary, 2008) et permettent d'obtenir, pour certains types de déformation, des solutions précises et robustes. Cela nécessite néanmoins d'adapter les algorithmes et leurs paramètres à chaque cas envisagé, ce qui rend ces modèles difficiles à utiliser sur des populations variées de patients ou au cas de grandes déformations. Une solution prometteuse, que nous étudions dans cette thèse, est d'effectuer le recalage avec un modèle biomécanique issu des données patients (Peters et Cleary, 2008).

Les modèles biomécaniques ne garantissent pas forcément d'obtenir des solutions correctes de recalage car il n'est pas forcement possible de modéliser mécaniquement la complexité d' un ensemble d'organes et de leurs interactions. Néanmoins, ces modèles sont guidés par des paramètres élastiques qui peuvent être mesurés sur patient ou ont des valeurs bien connues dans la littérature. Ils sont, pour cette raison, plus génériques que les modèles précédents et plus facile à contrôler. Ils nécessitent cependant l'intégration de conditions aux limites, qui sont déterminés dans ce travail à partir des images.

Les modèles biomécaniques ont donc le potentiel de permettre un recalage précis tout en générant des transformations plausibles. Leurs limitations résident cependant dans le coût des calculs des transformations et dans la difficulté de de connaître les propriétés physiques de l'objet. Des simulations en temps réel ont cependant pu être réalisées avec un modèle corotationnel (Courtecuisse et al., 2010) pour recaler des surfaces issues de données stéréoscopiques (Speidel et al., 2011; Bano et al., 2013), pour du recalage basé intensité avec un modèle d'insufflation (Oktay et al., 2013) et pour du recalage de surfaces via un algorithme de type ICP (Peterlík et al., 2018). Ces méthodes sont cependant limitées par le fait qu'elles ne font intervenir que la surface des objets, ne donnant ainsi aucune garantie sur le recalage à l'intérieur de l'organe, ou parce qu'elles utilisent des modèles spécifiques d'insufflation soit enfin parce qu'elles nécessitent une interaction avec l'utilisateur incompatible avec les gestes per-opératoires.

Dans de nombreuses modalités, le réseau vasculaire est visible ou peut être rendu visible grâce à l'injection d'un produit de contraste alors que les structures environnantes sont homogènes ou peu différenciantes. Le réseau vasculaire étant dense dans le foie,les vaisseaux, et en particulier les bifurcations, constituent ainsi des indices forts pour le recalage multi-modalité. La mise en correspondance des arbres vasculaires est cependant rendue délicate par le fait que le critère de similarité ne peut être basé que sur la longueur des vaisseaux et la géométrie ou la topologie des bifurcations. Dans le cas de grandes déformation, la conservation des longueurs n'est pas strictement vérifiée. Par ailleurs, il existe de nombreuses bifurcations avec la même topologie, ce qui accroît la combinatoire des hypothèses possibles.

Les approches basées sur le réseau vasculaire pour le recalage d'images 3D utilisent soit directement l'intensité soit l'extraction préalable du réseau. Les approches basées sur l'intensité utilisent toute l'information disponible dans l'image et on peut espérer qu'elles soient plus précises que celles basées sur des indices extraits. Cependant, les intensités des zones inter-vasculaires sont relativement homogènes et contribuent peu au recalage, voire le dégradent. Les approches par intensité de Suh et al. (2010) and Robben et al. (2012) modifient la métrique de similarité de manière à prendre en compte les propriétés des vaisseaux. Cependant Suh et al. (2010) ne peut prendre en compte les ambiguïtés de mise en correspondance tandis que Robben et al. (2012) imposent des longueurs constantes aux vaisseaux et ne peuvent prendre en compte des changement de topologie entre les images. De manière générale, les approches par intensité peuvent difficilement prendre en compte les différences d'apparence d'un organe entre deux images et requièrent le plus souvent une initialisation.

A l'opposé, les méthodes basées sur l'extraction d'indices peuvent prendre en compte ces différences d'apparence. Le caractère épars mais cependant bien réparti des vaisseaux dans l'image rend le processus de recalage à la fois plus rapide, plus générique que les méthodes basées sur l'intensité et beaucoup plus précis que les méthodes analysant seulement la surface des organes. L'extraction du réseau vasculaire peut cependant se révéler délicate selon l'imagerie utilisée et la qualité du contraste comme c'est le cas pour l'imagerie ultrasonore ou CBCT. Dans ce cas, le réseau est extrait de manière incomplète et de fausses détections peuvent être présentes. Les réseaux extraits en pré ou per-opératoire peuvent alors être très différents, les différences pouvant concerner le nombre, la longueur, la topologie ou le rayon des vaisseaux. Les fortes déformations modifient par ailleurs la géométrie des bifurcations, rendant l'identification de similarités difficile.

Parmi les méthodes utilisant les vaisseaux pour la segmentation, on distingue les approches qui visent à recaler les ligne de centre et les approches par mise en correspondance de graphes qui exploitent pleinement la topologie des vaisseaux. Lange et al. (2003) et Reinertsen et al. (2007) sont des exemples significatifs des approches de recalage par lignes de centre extraites dans les deux modalité. La déformation considérée est faible dans les exemples considérés et basée sur une estimation initiale à partir de quatre points manuellement mis en correspondance. Une approche de type ICP est ensuite utilisée pour recaler les lignes de centre. Le déplacement faible considéré ici permet d'avoir peu d'ambiguïté dans les correspondances. Dans Morin et al. (2017) et dans le cas du brain shift, des contraintes de contact (avec la dure-mère) sont prises en compte dans le modèle biomécanique pour mettre en correspondance des vaisseaux. Cette méthode est cependant limitée à de petites déformations et requiert une initialisation. Les méthodes de graph matching (GM) visent quant à elles à s'affranchir de la connaissance d'une estimée initiale et utilisent pleinement l'information topologique des bifurcations. Leur performance est cependant liée à la capacité à extraire de manière robuste les bifurcations. C'est cette approche qui est étudiée dans cette thèse.

**Segmentation des vaisseaux**

Nous utilisons dans cette thèse une représentation des vaisseaux sous la forme d'un graphe pour la mise en correspondance multi-modalité. Ces graphes sont issus des segmentations des images CTA, CBCT et ultrason 3D. Dans une première étape, nous utilisons la méthode de segmentation basée modèle proposée par (Smistad et al., 2014). Un graphe est ensuite déduit de la segmentation en utilisant l'approche proposée dans (Plantefève et al., 2017). La méthode ne nécessite aucune interaction avec l'utilisateur. Il faut cependant préciser que le temps requis pour traiter des images US est très élevé et incompatible actuellement avec les besoins du per-opératoire. Il est probable que dans l'avenir des méthodes de segmentation, basées en particulier sur des techniques de machine learning, puissent améliorer cet état de l'art.

Les images per-opératoires sont beaucoup plus bruitées et contiennent ainsi beaucoup plus d'erreurs de détection que les images pré-opératoires. Des fausses détections, des segmentations non connexes et globalement des imprécisions sur la position des bifurcations sont ainsi présentes à l'issue de la segmentation. Ces incorrections sont étudiées dans le chapitre III sur des données acquises sur un cochon.

Les techniques usuelles de mise en correspondance de graphes reposent sur des métriques de similarité pour élaguer l'arbre des correspondances possibles. Elles sont souvent basées sur l'apparence locale, comme la géométrie des bifurcations, ou sur des contraintes telles que le rayon des vaisseaux. Dans le cas des images per-opératoires et en particulier pour les images US, le rayon ne peut être extrait de manière fiable et cette contrainte n'est utilisée que pour écarter des mises en correspondances manifestement erronées. La distance géodésique entre les bifurcations est aussi communément utilisées comme métrique de similarité. Dans notre cas, avec des mouvements de grandes ampleurs et des fortes imprécisions sur la position des bifurcations, cette contrainte ne peut être pleinement utilisée.

Nous développons dans la suite des méthodes robustes permettant de recaler les arbres vasculaires en dépit d'erreurs affectant ces segmentations per-opératoires. Nous montrons aussi comment effectuer ce recalage en un temps compatible avec la clinique malgré la combinatoire du problème.

**Mise en correspondance de graphes**

En raison de l'impossibilité d'extraire des structures pertinentes et communes aux imageries pré et per-opératoires, nous avons adopté une technique basée sur les graphes pour le recalage. Nous proposons dans le chapitre IV un état de l'art des techniques et une description des limitation des méthodes génériques (Leordeanu et Hebert, 2005; Zhou et De la Torre, 2015; Torresani et al., 2008). Les méthodes dédiées aux vaisseaux sont classées en trois catégories. La première repose sur une initialisation connue de la transformation (Nam et al., 2011; Charnoz et al., 2005), la seconde utilise des propriétés géométriques et topologiques (Tschirren et al., 2005; Deng et al., 2010; Smeets et al., 2010; Robben et al., 2013; Pinheiro et al., 2017; Moriconi et al., 2018) et la troisième vise à obtenir le meilleur ensemble de correspondances entre bifurcations via la mise à jour de la transformation (Serradell et al., 2011, 2015; Pinheiro et Kybic, 2018).

La topologie et la forme des graphes pre et per-opératoire sont très différentes en raison de la déformation subie et du bruit présent dans les images qui altère la segmentation. Il n'y a que peu de méthodes considérant ce difficile problème. Parmi elles, les travaux de Seradell sur le recalage non rigide à base de graphes Serradell et al. (2015) sont le point de départ de nos travaux. Lors du parcours de l'arbre des hypothèses de correspondances potentielles, le nombre de correspondances potentielles est progressivement réduit grâce à l'évaluation de la qualité d'un ensemble d'hypothèses par des processus gaussiens (GPR). Ceci permet d'écarter des hypothèses de correspondances incohérentes avec l'ensemble courant et d'explorer d'autres hypothèses de l'arbre. Cette méthode permet ainsi de générer itérativement des hypothèses tout en restreignant l'espace de recherche. La solution est raffinée progressivement au fur et à mesure de l'ajout d'hypothèses de correspondance. Cette méthode a été testée sur des données réelles avec succès. Cette méthode ne nécessite aucune initialisation et elle est capable de prendre en compte des graphes ayant des différences topologiques.

La méthode GPR présente cependant deux inconvénients majeurs: le temps de calcul nécessaire pour traiter de grands graphes est très élevé et il est donc impossible d'envisager un usage clinique. Par ailleurs, les déformations possibles modélisées par processus gaussiens ne permettent pas un contrôle fin des déformations autorisées. On peut ainsi parvenir à des déformations incompatibles avec la physique d'un l'organe.

Pour résoudre la première limitation sur le temps de calcul de la méthode GPR, nous avons conçu la méthode iGPR qui introduit des contraintes permettant d'élaguer les hypothèses de correspondances. Des contraintes sur les rayons des vaisseaux en correspondance ainsi sur des caractérisation topologiques des arbres sont ainsi introduites pour réduire la combinatoire. De plus, l'espace de recherche est réduit dès le début du processus de mise en correspondance par une réduction de la covariance produit par les GPR, qui est, à ce moment très largement surestimée. Des expériences sur données synthétiques et données réelles sont effectuées, qui montrent une réduction importante du temps de calcul. Nous avons cependant observé l'incapacité du modèle à produire des résultats corrects avec de grandes déformations et observé également l'obtention de résultats parfois incompatibles avec les propriétés mécaniques de l'organe. Nous avons donc dans la suite de ce travail utilisé une estimation des transformations via un modèle biomécanique afin de remplacer les GPR qui ne caractérisent qu'implicitement les déformations.

**Mise en correspondance biomécanique**

Le modèle GPR est relativement générique et permet de simuler de nombreux types de déformations. Il est cependant, de par sa structure, incapable de générer des déformations anisotropiques ou présentant de fortes non linéarités. Les vaisseaux, qui sont plus rigides que le parenchyme, créent en particulier de telles hétérogénéités, qui ne peuvent être prises en compte correctement que via l'usage d'une modèle biomécanique. Deux modèles biomécaniques ont été utilisés dans ce travail. Le premier est un modèle co-rotationnel du parenchyme du foie. Le second est un modèle composite de foie vascularisé, beaucoup plus réaliste. Il est en particulier utilisé pour calculer la compliance en chaque point, qui est utilisée en remplacement de la matrice de covariance utilisé dans l'algorithme initial. C'est un des points originaux de ce travail qui vise à utiliser des contraintes mécaniques directement pour apprécier la compatibilité des hypothèses de correspondance. Ces modèles font l'objet du chapitre V.

La première contribution proposée est d'abord de remplacer l'estimation de la transformation faite par GPR par un modèle biomécanique de l'organe, avec l'idée qu'une estimation plus proche de la physique permet de mieux éliminer les hypothèses erronées (Garcia Guevara et al., 2018). Cette méthode appelée BGM permet de réduire l'erreur de recalage mais elle reste peu robuste au bruit et a encore un coût de calcul trop élevé.

L'utilisation d'une mise en correspondance basée sur la compliance est la seconde contribution de ce chapitre. Deux algorithmes ont ainsi été développés. VCGM est basé sur le modèle vascularisé du foie pour le calcul de la transformation et le calcul de la compliance. L'introduction de la mise en correspondance basée sur la compliance s'est révélé beaucoup plus efficace que l'usage de la covariance. La méthode développée ensuite, appelée ACGM, vise à réduire encore le temps de calcul grâce à une stratégie adaptative consistant à développer en premier lieu les hypothèses de mise en correspondances les plus plausibles. Cette stratégie réduit par ailleurs la sensibilité de l'algorithme au choix des paramètres de la méthode et améliore la qualité du recalage.

Les méthodes utilisées ont été testées avec des jeux de données synthétiques ainsi que sur des données réelles avec comme données préopératoires des scanners et pour données per-opératoires des images CBCT et ultrasons 3D.

# Contents

# List of Figures

## Chapter I

# Image-guided liver surgery

With a length of about 20 cm for an average weight of 1.5 kg, the liver is one of the largest organs of the human body. It is a vital organ, with a complex anatomy, and is particularly exposed to diseases because of its detoxification role in the organism. As a result, liver cancer caused 780,000 deaths in 2018 worldwide, making it the $4^{th}$ most lethal cancer (Bray et al., 2018). The liver is situated in the right upper quadrant of the abdominal cavity and has a soft consistency (if not cirrhotic). The rib cage surrounds and protects it almost completely. The liver is located under the diaphragm and is attached to it by the left and right triangular ligaments. It is also attached to the ventral wall by the falciform ligament (Tortora et Derrickson, 2008). The liver has also a dense and intricate vascular architecture, consisting mainly of two large veins: the portal vein (PV) and the hepatic vein (HV). Other important inner structures are the bile duct and the hepatic artery (HA) that usually run parallel to the PV, as shown in Fig. I.1.

The blood flow enters to the liver through the HA and PV. At the smallest HA and PV vessels (about 7 $\mu$m radius), the incoming blood mixes and reaches the hepatic lobule (the liver's smallest functional unit). The blood subsequently leaves the hepatic lobules and the liver through the hepatic vein. Figure I.2 shows 3D reconstructions of the liver vessels and highlights the complexity and density of the vascular network (Debbaut et al., 2014). We can also see that it gives a general idea of the shape of the organ, making it a structure of interest for registration problems, as we will see in the following sections.

## I.1 Treatment and imaging options

Cancer treatment options depend on several factors, such as the degree of progression of the disease, patient's overall health, or tumor size among other factors. In a relatively early disease stage, the options for tumor treatment are surgery, radio-

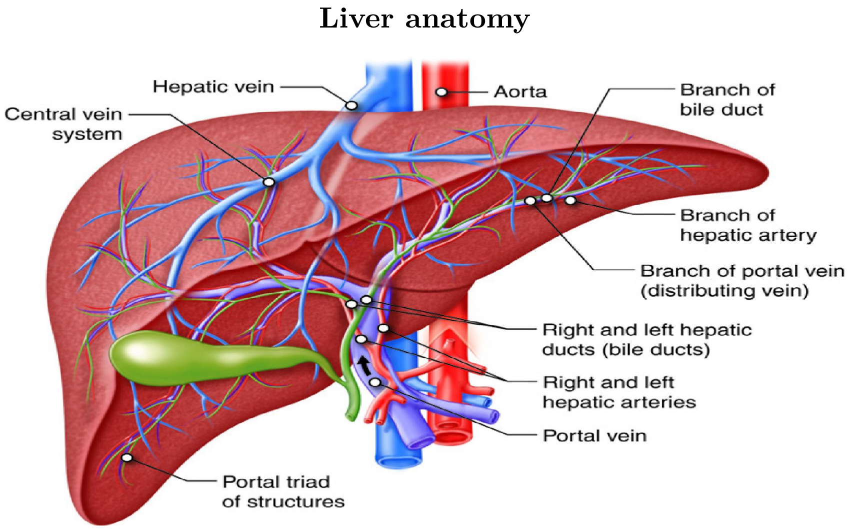

**Figure I.1:** Liver anatomy showing its important vascular structures (veins and arteries) and and bile ducts (in green) Atlanta Vascular and Vein Clinic (2019).

frequency ablation (RFA), percutaneous procedures, and radiation therapy. Surgery (also called hepatectomy) consists in removing the tumor along with its surrounding tissue. Among other treatments, surgery is one with the most favorable outcomes, specially when tumors are confined in small portions of the liver and can be removed without highly affecting the liver function. However, this is not always possible and alternative options need to be sought. Heating and destroying tumors with RFA or microwave therapy are other possible treatments, which are applied percutaneously, through laparoscopic or surgical interventions. Other approach to destroy cancer cells is to percutaneously inject ethanol into the tumor. This procedure is simple and particularly effective for small tumors. Radiation therapy destroys tumors of up to 5 cm with high-energy targeted X-rays. Other treatments are less effective but may prolong the life of the patient, such as Trans-Arterial Chemo-Embolization (TACE) a type of chemotherapy treatment where the feeding artery of the tumor is obstructed by drugs injected within the artery.

In all options above, the visualization of the patient's liver anatomy (including its blood vessels), at the time of the procedure, is essential to correctly and accurately deliver the therapy. To ensure accurate and complete destruction of tumors, percutaneous procedures require defining safety margins for ablation using various anatomical landmarks. For intra-arterial procedures, vascular selectivity is essential to reach the correct tumor-feeding vessels and maximize the treatment effectiveness. It also needs the exclusion of non-target vessels to preserve the rest of the hepatic arterial tree and avoid overtreatment (Ronot et al., 2016). Tumor resection, either laparoscopic or open, requires the definition of safety margins around the tumor

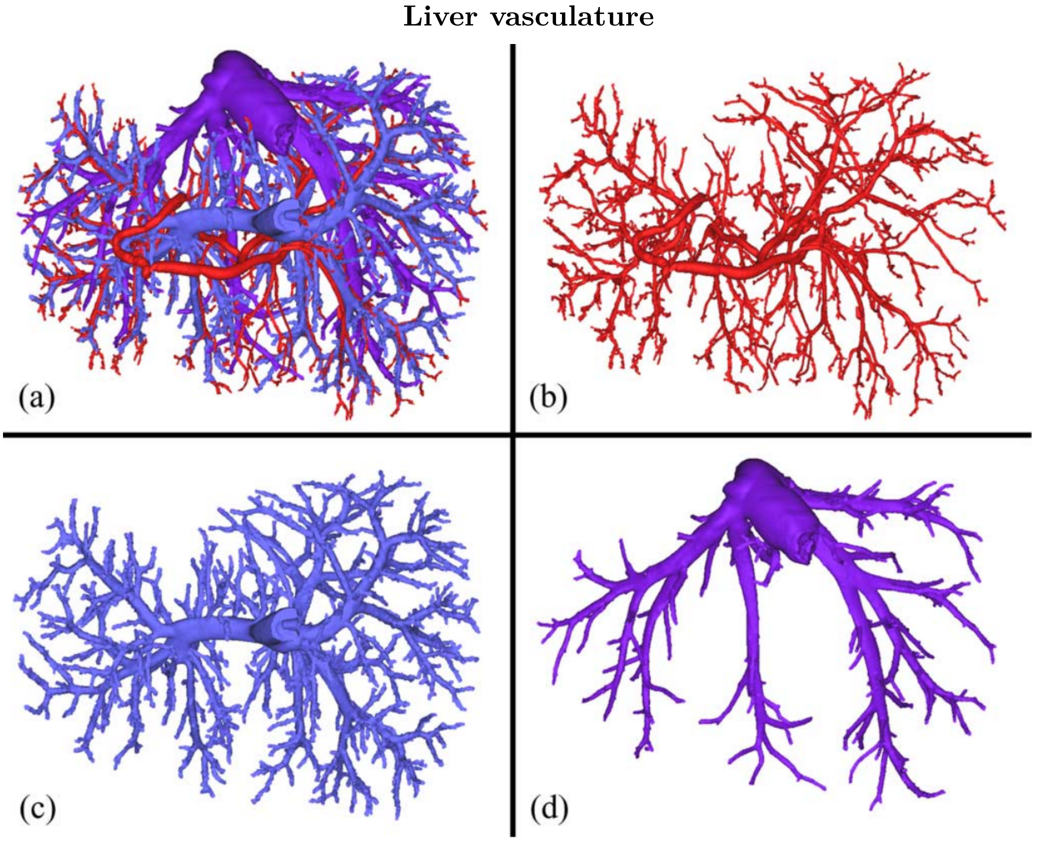

**Figure I.2:** 3D reconstructions of HA (b), PV (c) and HV (d) trees. The vessels shown have radii ranging from 13.2 mm to 0.6 mm. The lengths along the vessels in between closest bifurcations range from 74.4 mm to 16 mm (Debbaut et al., 2014).

and the determination of which vessels to cut to preserve the hepatic function and allow the liver to regenerate after surgery. Once correctly planned, liver surgery remains hard to accomplish because it is difficult to detect and reach subsurface anatomy.

The essential premise to achieve good results in all these procedures is therefore the availability of precise and reliable imaging techniques for accurate preprocedural planning and intra-procedural targeting. Before these intra-operative procedures, the clinical workflow includes standard available preoperative data to identify lesions within the liver parenchyma. The following is a relevant description of commonly used liver preoperative imaging:

- Computed tomography (CT) is a robust and rapid imaging modality useful in detecting liver tumors and extrahepatic metastases. Computed Tomography Angiography (CTA) includes the injection of an intravenous contrast agent to make blood vessels visible and to better identify liver metastases, which are hardly noticeable on non-contrast CT. The commonly used contrast injection and acquisition protocol results in arterial and late portal (hepatic) phase images. From the arterial phase image, the arterial structures and hypervascular tumors are visible. In the hepatic phase image shown in Fig. I.3.a, the parenchyma is enhanced through the blood supply of the PV. Some enhancement of the HV can also be obtained (Smithuis, 2014).

- Magnetic resonance imaging (MRI) detects different types of normal and pathological tissue depending on its physical properties and the pulse sequence that generates the image. With respect to CT, MRI captures images with better contrast on soft tissues but often with more artifacts. Different pulse sequences are generally used to generate images of the liver, usually acquired before (shown in Fig. I.3.b) and following the administration of an intravenous contrast agent. In general, the spatial resolution of CT is superior to MRI, so it is often preferred for planning and tumor identification. However, novel higher resolution MRI combined with diffusion-weighted imaging (DWI) and hepatocyte-specific contrast agents can detect sub-centimeter liver metastases better than CT (Frankel et al., 2012).

Once preoperative image acquisition and procedure planning have been performed, the actual treatment can begin. Depending on the type of intervention, different imaging options can be used to control its progress. During surgery (open or laparoscopic), the use of interventional imaging is often limited to ultrasound (US) unless the operating room is equipped with an MR or CT scan. US imaging allows to visualize the vascular anatomy and the largest lesions. For other types of interventions, CT or CBCT remain the main imaging modality. MRI is less often used because of the additional constraints it puts on the operative protocol, in particular the use of non-ferromagnetic instruments. Generally, small lesions (and vessels) are best identified in preoperative (CTA and MRI) images, due to a higher resolution or contrast images compared to most intra-operative imaging modalities (Kingham et al., 2018). In this thesis, CBCT and US are the common intra-operative modalities considered, and their main properties and limitations are presented below:

- Cone beam computed tomography (CBCT) is an accessible imaging technique in which the X-ray tube and detector panel rotate around the patient. CBCT is an imaging modality that is more available in the operating room than CTA or MRI. However, the contrast to noise ratio in CBCT is about half than that in CTA. CBCT also suffers motion artifacts, beam hardening, partial volume, and ring effects. Thus, certain important lesions and soft tissue structures are

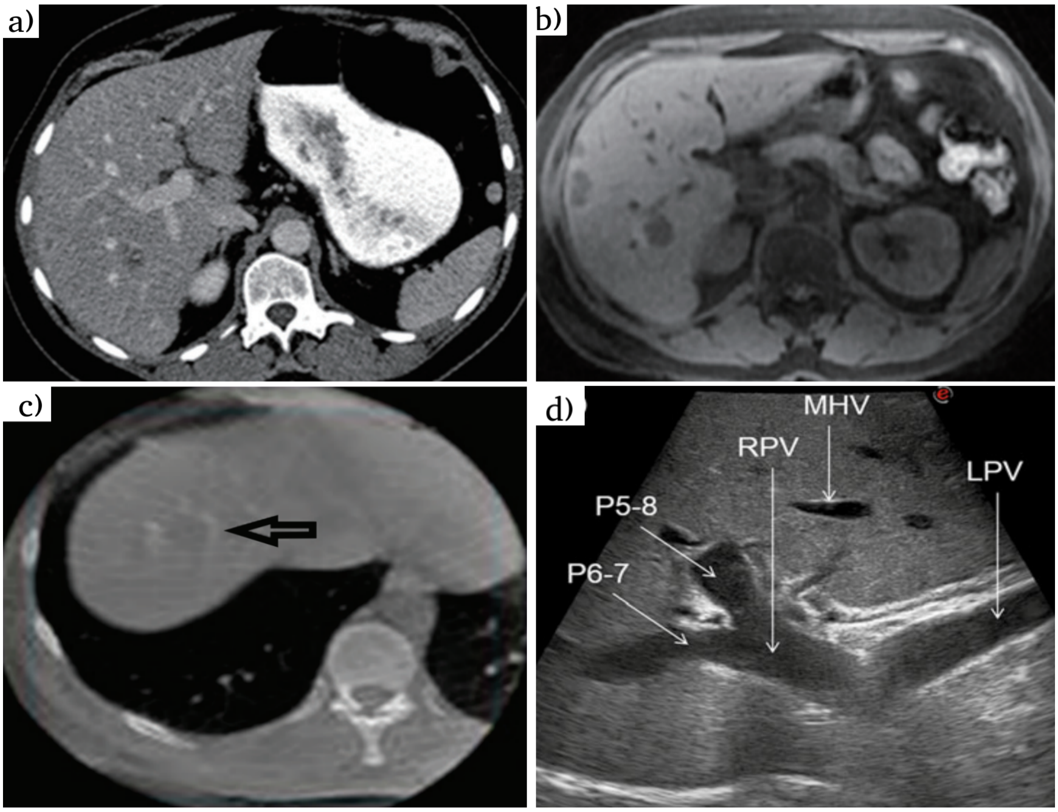

**Liver imaging**

**Figure I.3:** Pre-operative images of human liver in a) CTA and b) MRI, T1 weighted pre-contrast (Frankel et al., 2012). Intra-operative liver images c) CBCT with injected contrast agent (Paul et al., 2015a) and d) US with branch segments (P5-8, P6-7), right (RPV) and left (LPV) portal vein and middle hepatic vein (MHV) (Torzilli et al., 2014).

not visible in the CBCT image (Tacher et al., 2015). CBCT acquisitions in the liver are mostly obtained following intravascular contrast agent administration, either through a catheter positioned in the vessel of interest (directly connected to or inside the liver) or in peripheral veins. Various CBCT contrast injection protocols exist, and result in different types of images of the liver anatomy, in particular if they are taken during arterial, portal venous (shown in Fig. I.3.c), or even delayed phases (Bapst et al., 2016).

Intra-arterial procedures require an in-depth assessment of the hepatic arterial network and the ability of the operator to properly identify, reach and treat the tumor-feeding vessels and to preserve the rest of the hepatic arterial tree. However, because of imaging artifacts and low resolution, feeder vessels smaller than 1 mm diameter or where contrast agent accumulates close to the tumor are very hard to detect (Iwazawa et al., 2013). Moreover, CBCT significantly reduces the detectability of small hepatic tumors (i.e. less than 5 mm in diameter) compared to preoperative images (Paul et al., 2015b).

- US is commonly used to guide percutaneous ablations and resections. Because it is real time, simple to set up, has no ionizing radiation, is less expensive and provides in-depth information of the organ structures. From the several US modes available, 3D B-mode US based on mechanical scanning was used in the experiments presented in this thesis. The 3DUS reconstructs a 3D image from a series of 2D images (shown in Fig. I.3.d) acquired with a linear transducer that is rotated with a motorized mechanism. In the liver, US has sufficient soft tissue contrast to visualize some lesions and vessels. However, some tumors are undetected intra-operatively because of their location, small size, or echogenicity. A similar problem happens with small vessels (Mauri et al., 2015). For example, Kim et al. (2012) reported that 25% of small ($< 3$ cm) tumors diagnosed on CTA/MRI reported were not visible on US. Thus, it is common that surgeons experience important difficulties locating hepatic tumors in the operating room.

## I.2 Organ motion and deformation

Besides the choice of imaging modality, all the treatment options presented previously are also impacted by intra-operative organ motion or deformation. For instance, during percutaneous procedures, a different patient pose, and the respiratory motion, can lead to important differences in the location of the tumors and vessels between the pre and intra-operative images. In 95% cases, the reported magnitude of non-rigid deformation ranges from 2.5 mm to 9 mm. In the other cases, the difference can go up to 44 mm (Luu et al., 2018). With laparoscopic procedures, it is necessary to increase the working space by infusing carbon dioxide ($CO_2$) gas into the abdominal cavity (pneumoperitoneum), as seen in Fig. I.4. The insufflation causes distension and displacement of the diaphragm, ligaments are pulled into tension as the abdominal cavity expands (Malbrain et al., 2016). Intra-operative deformation is further complicated by the organ mobilization and possible dissection of some ligaments. For the partial liver surface visible during laparoscopy, non-rigid deformations ranging from 4 to 26 mm were reported (Heiselman et al., 2017).

In the case of open surgery, the procedure requires complete mobilization and exposure of the liver, which leads to significant organ deformation compared to the preoperative image. In that context, deformations up to 60 mm have been reported Heizmann et al. (2010). This obviously impacts intra-operative navigation

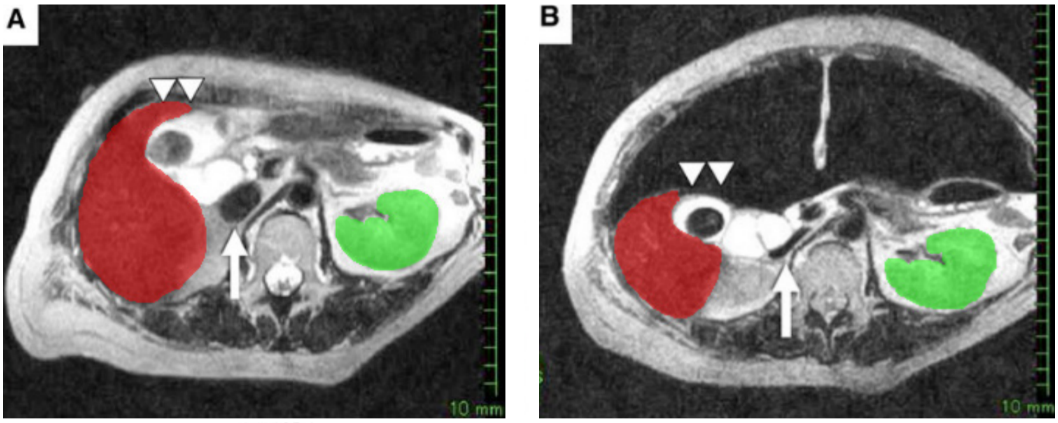

**Deformation induced by the pneumoperitoneum**

Norifumi Tsutsumi et al. - Surg Endosc - 2013

**Figure I.4:** The liver (in red) is strongly deformed while the shape of the left kidney (in green) is almost the same in both images (source Tsutsumi et al. (2013)).

during liver resection and calls for solutions to provide visual guidance during such interventions, using combinations of registration and augmented reality.

## I.3 Image fusion and augmented reality

### I.3.1 Clinical benefits

Since each imaging modality provides different and often complementary information on tissue structures as well as deformation changes, fussing in a common coordinate system pre and intra-operative images provides added benefits. For example, adding the subsurface anatomy visualization during laparoscopy improves the surgical navigation and resection (Heiselman et al., 2017). Interventions augmented with preoperative data are commonly easier and better guided, obtaining increased target localization accuracy while reducing invasiveness (Peters et Cleary, 2008). Augmented intra-operative images can allow accurate localization of small tumors and guidance during ablations or resections. Here, the augmented or fused image helps to follow the safety margins around the tumor.

When using CBCT, the fused information can be very useful to provide better soft-tissue details than CBCT alone thus improving the identification of hepatic tumors (Paul et al., 2015b). During surgery, multiple image acquisitions, and possibly contrast agent injections, are needed to provide information about the tumor location and surrounding vessels. An accurate image fusion method could reduce this number of image acquisitions and consequently lower patient exposure to contrast agent toxicity and radiations (Ronot et al., 2016). In addition, during intra-arterial procedures, such as Trans-arterial Chemo-embolisation, augmented CBCT can reduce navigation time and the dependence on interventional operator skills. The complex nature of the hepatic vasculature makes it difficult to identify the arterial branches, and multi-modality fusion has been identified as an effective solution for vessel-tracking and navigation (Paul et al., 2015b).

Real-time US fused with CTA or MRI can also increase the detection of small tumors and vessels, making targeting and monitoring of these structures more accurate (Mauri et al., 2015). 3DUS can be used to understand the spatial relationship between tumors and vascular structures. However, this imaging technique has a limited field of view. Also, speckle noise, low contrast-to-noise ratio and artifacts make it difficult to get useful 3D information from its direct visualization. Augmented 3DUS can compensate for these limitations and improve the spatial visualization and understanding of the anatomy. This can be obtained by generating a more complete (fused or augmented) image that includes small vasculature and vessels located outside of the US field of view. Such an augmentation can allow intra-arterial procedures to be fully guided by US instead of CBCT. When acquiring liver images with US, the interference from the patients' ribs make it difficult to image the posterior and lateral parts of the liver. An augmented US image can be a solution for visualizing these structures during percutaneous interventions (Kim et al., 2012).

### I.3.2 Challenges

One important difficulty when performing image fusion or augmented reality for hepatic surgery comes from the (large) deformations that often take place between the two image acquisitions, as mentioned previously. Handling these deformations requires nonrigid registration methods to align the preoperative models or images onto the intra-operative images. The choice, complexity, and accuracy of the registration method highly depends on the type of data to register (3D to 3D image, 3D model to 3D image, 3D to 2D image, etc...). Here are some scenarios when considering the liver.

In the context of open or laparoscopic surgery, the general approach is to register the preoperative data into the 3D surface stereo reconstruction of the liver. In this scenario, the portion of the liver visible during the laparoscopy is small; thus, surface reconstruction techniques only provide limited information of the intra-operative organ shape. Also, the lack of salient features, which would lift ambiguity in the registration process, introduces additional uncertainty. The deformation of both the invisible surface and inner critical structures thus remains relatively unknown, which is an issue for guidance.

To compensate for these issues, previous works have used biomechanical models, to bring physics-based regularization in the registration process. Therefore, the problem is solved by defining boundary conditions based on intra-operative data. This has shown promising results but only to a certain extent. In a phantom study, Haouchine et al. (2015) reported a TRE of 9.26 mm. The error increases when the target is far from the reconstructed surface and when the deformation is larger. The lack of inner information and the surface reconstruction uncertainty due to the small stereo baseline affect the TRE. Suwelack et al. (2014) reported a similar result in another phantom study. They registered a biomechanical model of the liver into the intra-operative surface using an electrostatic potential field. Although results are visually satisfactory in a silicone phantom dataset[1], the TRE remains large (8.7 mm).

To improve the elastic registration, Haouchine et al. (2016) segmented the intra-operative 3D point cloud and used it to automatically define the boundary conditions of a biomechanical liver model. Using this method in one synthetic experiment, the error obtained from 5 internal targets ranged from 4 to 12 mm. This method requires additional validation, on real data, to assess its accuracy and robustness. More generally, the question of validation, using patient ground truth data, remains a limiting factor to compare results. Some remarkable efforts, presented by Collins et al. (2017), have been made recently in this direction, such as the Sparse-Data Image-to-Physical Liver Registration Challenge [2] which consists of 112 sparse point clouds patterns taken from the operating room and transposed onto a quantitative liver phantom with similar deformation patterns as the operating room. The phantom has 159 subsurface 1mm diameter targets to assess the accuracy of registration algorithms.

Yet, when relying only on partial surface information, registration errors are higher in areas that are not covered by the surface, and computing an accurate displacement field in the volume remains an ill-posed problem. Therefore, it seems preferable, when possible, to consider more than the surface information. To this end, intra-operative 3D imaging is attractive to get accurate registration in AR guided procedures. Current liver 3D image guidance systems have showed the ability to identify hepatic tumors in several procedures. However, these systems are currently unable to handle large nonrigid deformation, therefore limiting their accuracy in a number of clinical cases. For instance, in a percutaneous augmented US intervention study, 13 out of 295 cases reported registration errors from 8 to 16 mm (11±3 mm). This resulted in unsuccessful targeting of lesions (Mauri et al., 2015). In another augmented US tumor resection study, 50 cases reported a 5.5±5.6 mm registration error. Although this is not a direct measurement of accuracy, errors above 5 mm are usually considered as clinically relevant (Kingham et al., 2018).

---

[1] https://opencas.webarchiv.kit.edu/?q=PhysicsBasedShapeMatching

[2] https://sparsedatachallenge.org

### I.3.3 Vessel-based registration

To increase registration accuracy when dealing with large deformations, and to avoid the ill-posed nature of registration problems only based on partial surface information, a natural direction is to rely on in-depth information provided by the vascular network of the organ. The liver, which we consider as our main target, seems well suited for this type of approach, as illustrated in Figure I.1. From the considered pre and intra-operative imaging modalities, vascular structures need to be identified. While this is often done at the preoperative stage to perform the surgical planning (and define resection planes that will preserve as much as possible of the vascularization of the organ), this is significantly more challenging to do intra-operatively. This is mainly due to clinical and imaging constraints.

The registration method should therefore be able to handle image intensity inhomogeneities or artifacts and should satisfy intra-operative clinical constraints. It should ideally be compatible with common image modalities (such as 3DUS, CBCT, MRI, and CTA, only 3D to 3D vessels registration is considered) and be fully automatic without initialization, external sensor, nor user interaction. The registration process should be sufficiently fast such that it does not compromise the workflow during the procedure. The process time should be less than or equal to the intra-operative acquisition time, i.e. a few minutes as reported by Mauri et al. (2015).

### I.3.4 Our proposal

In this thesis, we address the development of an automatic elastic registration method suited for vascularized organs undergoing small to large deformations, using vascular graphs extracted from both the pre and intra-operative images. The intra-operative vascular tree is in general deformed, noisy, and incomplete. These characteristics, the lack of distinctive features and the large number of bifurcations make the matching of the pre and intra-operative graphs a challenging task. Although methods dedicated to non-rigid graph matching exist, they are not efficient when large intra-operative deformations of tissues occur. Serradell et al. (2015) proposed a matching method that uses a Gaussian Process Regression (GPR) and the current set of matching hypotheses to determine the transformation and a new compatible match. So it iteratively generates matching hypotheses while refines the search space.

The first contribution is a biomechanical graph matching method (BGM) that builds on the work of Serradell et al. (2015). BGM combines the GPR matching with a biomechanical model of the organ, as a mean to discard matching hypotheses which would lead to non-plausible deformations (Garcia Guevara et al., 2018). However, just replacing the GPR by a biomechanical model was not robust to noise, only matched limited size graphs and the computation time was still above intra-operative constraints.

The second contribution is the Adaptive Compliance Graph Matching (ACGM) method, which allows to efficiently find the best graph matches with a novel compliance-based adaptive search. The matching hypotheses are adaptively generated in a rigid to soft approach using a better and novel metric, which is based on the notion of compliance, the inverse of the stiffness. ACGM further reduces the computation time by predicting first the most plausible matching hypotheses and reduces the sensitivity on the search space parameters. This contribution improves the registration quality and meet intra-operative timing constraints.

The proposed registration methods are evaluated with realistic synthetic and real porcine datasets. The porcine CTA, CBCT and US images were acquired during two experimental sessions in the IHU Strasbourg under institutionally approved animal ethics protocol. This thesis does not contain patient data. The evaluation, using both real and synthetic datasets, shows that the elastic registration is compatible with intra-operative constraints.

## I.4 Manuscript organization

The manuscript continues with a background on multi-modality image registration state-of-the art followed by a description of vessels features' extraction and its influence on the registration process. Then, details about the matching methods developed in this thesis are presented, along with validation experiments. The fundamental elements of the complete registration pipeline, shown in Fig. I.5, are described as indicated in the following chapters description:

- Chapter II summarizes the deformable multi-modality registration state-of-the-art with special interest of vascularized deformed 3D images.

- Chapter III describes the segmentation pipelines used to segment vessels and extract graphs from CTA, CBCT, and US images. It presents the segmentation and graph extraction results and shortcomings. It also shows the graph characteristics that directly impact the matching methods.

- Chapter IV reviews the graph matching methods state-of-the art focusing on their limitations regarding the application considered. The GPR graph matching method (Serradell et al., 2015) is summarized because it is the base of the contributions presented in Chapter V. Then, an improved graph matching algorithm (iGPR Garcia Guevara et al. (2018)) is presented. This method significantly reduces the matching time and is used for automatic initialization.

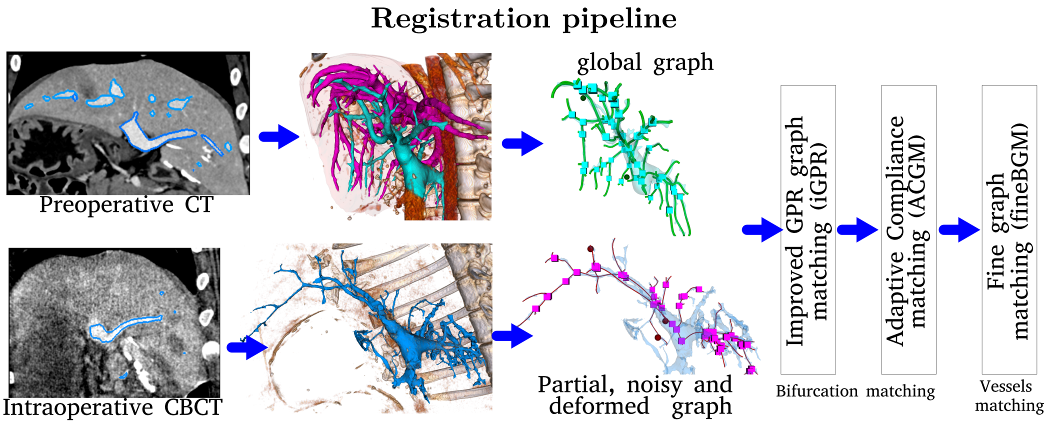

**Figure I.5:** Description of the complete registration pipeline: The graphs are extracted from the vessels segmentation of pre and intra-operative images (CTA and CBCT in this example). Then, the graphs bifurcations are matched (mostly rigid and incompletely) with iGPR. This first matching is used to initialize ACGM, which finds a complete deformable bifurcations match very efficiently. This compliance-based matching (ACGM) is the main contribution described in this article. Finally, the fine FEM-based alignment (fineBGM) of the graph edges is performed.

- Chapter V describes the biomechanical model used and then presents the two main contributions of the thesis: 1) the biomechanical graph matching registration method BGM which matches graphs even when large deformation occur using the biomechanical model (Garcia Guevara et al., 2018). 2) An adaptive compliance graph matching (ACGM) method that reduces the search space by using the compliance, while finding most of the bifurcations matches including those with large deformations. The fine alignment of graphs edges using the biomechanical model (Garcia Guevara et al., 2018) is presented as well.
- Chapter VI concludes this thesis and presents some directions for future work, such as matching of disconnected, noisy, and large deformation graphs within intra-operative timing constraints.

Chapter II

# Multi-modality deformable registration

## II.1 Introduction

Image registration consists in establishing spatial correspondences between different acquisitions and finding the optimal transformation that brings together images into a common coordinate system. Depending on the application, two or more images can be registered. Among other applications, performing registration can be useful to model the anatomical variability of the population, to study temporal anatomical changes, and to assist medical diagnosis and therapies (Sotiras et al., 2013).

As described in Chapter I, augmented image-guided procedures integrate complementary information (acquired from different modalities) by registering pre-operative (source) into intra-operative (target) images. The alignment of different image modalities is known as multi-modality registration. The choice of registration method is often directly related to the image modality used and its acquisition conditions. The voxel or pixel intensities of common intra-operative modalities (US, CBCT) do not have a simple relationship with the pre-operative ones. Moreover, intra-operative images generally have smaller fields of view, more artifacts and lower contrast to noise ratio, due to non-optimal acquisition conditions.

Besides the multi-modality problem, one important consideration in intra-operative procedures is the deformation of the organ. Brain surgery has already benefited from image-guided registration since the brain shift is relatively small and the (rigid) skull offers a mean to define a common reference frame (Kingham et al., 2018). However, depending on the procedure the liver undergoes large intra-operative deformation and motion. Figure II.1 shows the rigidly aligned pre an intra-operative vessels of the liver where the nonlinear deformation reaches up to 6 cm (Heizmann et al., 2010). This large deformation is an important challenge

**Intra-operative open surgery nonlinear deformation**

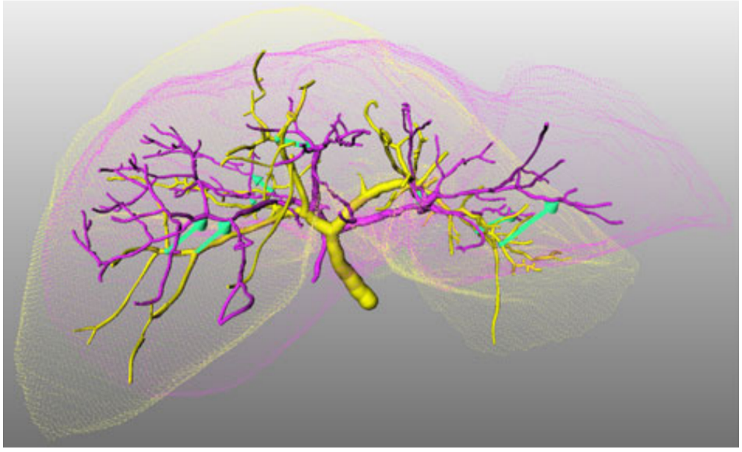

**Figure II.1:** Illustration of the amplitude of the nonlinear deformation that can occur during open surgery. Yellow: liver reconstructed from the preoperative image. Purple: liver reconstructed from intra-operative imaging (Heizmann et al., 2010).

of intra-operative registration. Generally, the nature of the expected deformation helps to select an appropriate transformation.

Considering the clinical environment and requirements, the registration needs to be fully automatic, robust and accomplished in $\sim 5$ minutes. As described by Sotiras et al. (2013), deformable image registration usually has three main parts:

- **Deformation model.** A nonlinear dense transformation establishes the relationship between the images to be registered. This transformation can be specified by an explicit function, or a non-parametric deformation represented by a dense displacement field. This transformation is a mapping function of locations from the target to the source images. The transformation used considerably defines and limits the registration solution (Sotiras et al., 2013). Diffusion models, thin-plate splines, Free-form deformations with b-splines and biomechanical models are common transformation models used in deformable image registration and briefly are described in Section II.2.

- **Objective function.** In general, two terms compose the objective function. The first term is commonly known as the matching criterion, (dis)similarity metric or distance measure, it quantifies how well the source image is transformed to match the target. The second term attempts to specify desired properties of the solution by regularizing the transformation, with the goal of reducing the complexity of this ill-posed problem. Based on their matching criterion, the registration methods can be divided in three groups:

1) Feature-based registration requires from both source and target images accurate extraction of corresponding and distinctive features. These algorithms measure the alignment of corresponding structures and usually minimize a distance metric between corresponding features.

2) Intensity-based algorithms operate directly on voxel intensities and rarely require any prior object identification. These algorithms are very often based on an optimization process that assesses the fitness of trial deformations using corresponding intensity distributions similarity as a metric. With multi-modal images the criterion should take into account the dissimilarity of image intensities.

3) Hybrid registration methods try to obtain the advantages of both the intensity- and feature-based methods by using complementary information. So specific features can directly contribute to the registration and the whole deformation (even parts without features) relies at least on the images intensity. The extra processing is a drawback of these methods that usually increases their computation time.

- **Optimization method.** The transformation is optimized to produce the best fitting between images maximizing or minimizing, depending on the similarity metric used, the objective function (Sotiras et al., 2013).

The characteristics of the images to be registered determine the deformation model and the objective function required. The optimization strategy is important to efficiently find registration results and avoid local minima in the inherently ill-posed problem. Creating and/or putting together the proper components that satisfy registration needs is a challenging problem (Peters et Cleary, 2008). The registration of the pre and intra-operative images can be handled in many different manners depending on the application, the image modality, the parameter space, or the optimization process.

In general, pre and intra-operative registration usually requires the identification of feature correspondences in both images or an image similarity metric that is robust to the intensity difference, noise and artifacts. Therefore, it is really important to consider how the anatomical properties of the considered organ are imaged in each modality. Feature-based algorithms are usually faster than intensity-based registration, thus they are more appropriate for intra-operative applications. However, false or insufficient corresponding features can produce inaccurate registration results. Specially, deformable registration with large degrees of freedom can not robustly be determined without sufficient detected features. To tackle this difficulty associated with the ill-posedness of the problem, the transformation can be regularized incorporating task specific constraints (smoothing or statistical models, for example) (Peters et Cleary, 2008).

Sotiras et al. (2013) broadly surveyed and classified deformable registration methods, which is an active and vast research area. This Chapter focuses only on 3D/3D registration methods that attempt to handle non-linear deformation of different image modalities and partially comply with the clinical constraints described in Section I.3.3.

Section II.2 presents general multi-modality deformable registration methods grouped by their transformation models and describing its similarity metrics. Then, Section II.3 focuses on approaches that use vessels' information into the registration.

## II.2 Intra-operative registration

The following are relevant methods that try to address the intra-operative multimodal deformable registration. These methods are grouped by the type of transformation used. Their similarity metric evaluated over the whole image domain is described.

### II.2.1 Registration with transformation derived from diffusion models

The transformation of the algorithms described in this section impose a diffusion model regularization. This transformation is inspired by the Demons framework, where a nonparametric deformation model is regularized by applying a Gaussian filtering to generate a smooth displacement field (Vercauteren et al., 2009). Aside from relying on similarity metrics that are intrinsically more suitable to disparate modalities, images can be transformed into a consistent representation in which voxel values capture some characteristics of the original images. The ability to encode such local structural information is increased by using a descriptor (vector) representation.

Heinrich et al. (2012) presented a new modality-independent neighborhood descriptors (MIND) for registration. The descriptor is based on non-local means (NLM) to capture local structure from different imaging modalities. The similarities among nearby patches form the novel descriptor and its vectorial difference serves as matching metric. Then, the MIND descriptor within a diffusion-based registration method has shown to provide nonlinear mappings between MR and CT images of the lung.

For robust MR-CT registration, Reaungamornrat et al. (2016) assumed that viscoelastic mappings (i.e., a combination of elastic and fluid deformations) as approximated by Demons, could improve the ability to resolve large deformation within noisy data. They propose a symmetric diffeomorphic deformable registration algorithm incorporating the modality-independent neighborhood descriptor (MIND) and a robust Huber metric. The method accurately registered realistically noisy data achieving 1.4 mm TRE outperforming other state-of-the-art methods. The method is not tested with large deformation (rigid TRE of the data is 4.3 mm) nor with common noisy intra-operative modality.

### II.2.2 Registration with transformations derived from interpolation theory

Thin-Plate Splines (TPS) is the first transformation considered in this class. It uses interpolation theory, so the deformation of the whole image is interpolated from a set of image points. These control points can be irregularly placed and their corresponding displacements are known. Lange et al. (2009) combined a TPS registration using manually selected landmarks with a fast non-parametric diffusion registration by formulating a constrained discrete joint optimization. It uses a normalized gradient field to measure the power Doppler US and CT images similarity.

The other transformation considered in this class is the Free-form deformation (FFD) coupled with cubic B-splines. This transformation model is simple, can efficiently provide smooth local deformations using only few degrees of freedom. It is a deformation model commonly used in medical image registration. The registration proposed by Rueckert et al. (1999) searched for the set of control point displacements that minimized the cost function, which includes a Normalized mutual information intensity similarity measure and a TPS bending energy.

The rest of methods described in this section use the FFDs as a transformation. The main difference in between these methods is the similarity metric used which is highlighted in their description. While Mutual information (MI) and its normalized variants are prevalent similarity metrics for multi-modality imaging (Andronache et al., 2008), a disadvantage of this metrics is that they sample the entire image to establish the statistical relationship. This significantly limits their application when this relationship changes spatially, e.g., in the common intra-operative presence of intensity inhomogeneity due to scatter or shading artifacts.

To reduce this spatial variation sensitivity, the metrics can be evaluated locally in a large enough spatial neighborhood that contains enough samples for reliable MI estimations (Klein et al., 2008). However, the spatial intensity inhomogeneity in intra-operative images is very large and this inhomogeneity makes the application of local MI (LMI) challenging due to its requirement for relatively large spatial neighborhoods. Furthermore, the computation time of LMI linearly increases with the number of local MI estimates, making it significantly slower than MI.

Another common statistical similarity metric is the correlation-ratio (CR), which uses a functional relationship between the modalities (Roche et al., 1998). To address the spatial intensity inhomogeneity in the US images, Rivaz et al. (2015)

estimated a highly local and reliable variant of the CR similarity metric on small patches. The orientation of this metric gradient is used to suppress false correspondences. Finally by using an efficient optimization method, the MR image is non rigidly registered to 3D US of the brain in only 30 seconds.

Wein et al. (2008) introduced the Linear Correlation of Linear Combination ($LC^2$) similarity measure, which assesses the correlation of combining signals extracted from CT with ultrasound, without knowing the influence of each signal. This metric was only used to rigidly register CT images based on the modalities characteristics. Then, Fuerst et al. (2014) adapted the $LC^2$ similarity measure to non-rigidly register freehand 2D US with MRI of the brain, where the $LC^2$ correlates the US image with MRI intensity and spatial gradient magnitude.

In general, there is a large number of potential deformations that can generate images that resemble to each other, however none of these nonrigid registration algorithms can guarantee that their result is the correct one. Moreover, when intra-operative conditions are constrained with a limited field of view, bizarre deformations usually occur outside of the support volume of the transformations derived from diffusion models or interpolation. Because these deformation models are very poor and unstable when extrapolating missing data, despite being fairly good at interpolation (Peters et Cleary, 2008). Other issue of these registration methods is their limited capture range. Due to their nonlinear and non-convex objective functions, the optimization requires a good initialization to avoid local minima.

Deformable transformation requires a large number of degrees of freedom, this implies that the registration is considerably under-determined. This problem is worsened when registering low resolution and low signal-to-noise ratio images, like the ones we consider. When using a rigid or affine transformation, this problem can be directly solved with RANSAC, but accurate and robust registration is difficult when more complex transformations are used and it requires other constraints. Incorporation of plausible deformations via a motion model, statistical shape atlas or biomechanical model are likely to provide robust and accurate solutions (Peters et Cleary, 2008). Our approach uses the latter.

### II.2.3 Registration with transformation derived from biomechanical models

Some deformations that occur during interventions are large and complex. The previous transformation models do not consider physical consistency with organ properties, in particular heterogeneities and anisotropy of the tissues. Models without tissue characteristics tend to diverge from the exact solution. They only guarantee the correct solution if the parameters are adjusted to the specific case, which is difficult to do for complex deformations and in a patient-specific manner.

Moreover, intra-operative noisy and partial images require additional information to constrain the large number of potential registration solutions and register the images accordingly to physically valid deformations. A promising solution is to link registration with a biomechanical model from available pre-operative data prior knowledge (Peters et Cleary, 2008). Biomechanical models do not always guarantee correct solution, but they facilitate parameter settings by relying on real (measured or from literature to appropriate case) values.

The finite element method is appropriate to simulate continuum mechanics throughout the body and incorporate prior knowledge into the registration. The equilibrium conditions of the stress and strain within the body under the influence of external loads can be described with a set of partial differential equations (PDEs) using the elasticity theory. These equations can not be solved analytically for an arbitrarily shaped body, thus a mesh of simple topology elements connected at node points is generated from this body. Given this mesh, the finite element method can solve approximately the continuum mechanics PDEs for the finite number of nodes (Peters et Cleary, 2008).

Force and displacement are the boundary conditions that can be define on the model nodes. Besides gravity, forces are usually unknown however the intra-operative images have very useful information to determine the displacements. Typically, the completeness of the displacement boundary conditions determines the accuracy of a biomechanically-based registration, rather than factors such as the material properties (Peters et Cleary, 2008).

After the mesh generation and boundary conditions definition, it is necessary to determine the stress and strain relationship for the specific tissue using an adequate constitutive law. Hyperelastic models correctly describe the non-linear behavior of biological soft tissues and are able to model properly large displacements, although they usually require significant computation time. Some recent hyperelastic models have near real time computation time, however its parameters characterization is not trivial (Marchesseau et al., 2017b).

Applications that require real-time computations often assume a linear elastic behavior (Cotin et al., 2000). As an alternative for linear elastic materials which can not properly model large displacements, corotational elastic models have been proposed Courtecuisse et al. (2010), in which linear elastic stiffness matrices are rotated for each element, to allow for large displacements. However, the stress-strain relationship remains linear.

Consequently, the following methods used biomechanical models to exploit prior knowledge. Speidel et al. (2011) registered a pre-operative biomechanical models of the liver into intra-operative stereo endoscopic images. A linear and a Neo-hookean elastic model were considered, and the accuracy of registration was assessed on a phantom. The results are slightly better with the second model, but the model is not suitable for real time simulation.

Oktay et al. (2013) coupled a linear co-rotational elasticity biomechanical insufflation model with the local cross correlation intensity similarity measure to register preoperative and simulated intra-operative (random noise and down-sampled) CT images. However, the insufflation models only a specific deformation, and the similarity metric does not handle common intra-operative modalities image intensity variations and artifacts.

In an alternative approach to put aside the intensity variation of CT and CBCT images, Bano et al. (2013) segmented the intra-operative anterior surface of the liver and manually obtained some corresponding landmarks. The pre and intra-operative surfaces were matched using the surface geodesic distance to the landmarks. Then, this matching drove the registration with a biomechanical model of the liver.

Peterlík et al. (2018) presented a surface matching method that incorporates a linear co-rotational biomechanical model into the iterative closest point registration. This allowed to register a detailed 3D model into a largely deformed surface. Both the preoperative model and the intra-operative surface were obtained using a semi-automatic approach. For the two previous methods, the need for user interaction restricts their intra-operative deployment, and in the presence of partial surface, obtained from intra-operative modalities, the displacement constraints are uncertain and inner deformations probably inaccurate.

Despite that anisotropy is important to accurately model brain or muscle tissue, for hepatic healthy tissue the results about the relevance of anisotropy in the nonlinear models diverge (Marchesseau et al., 2017b). The material properties of vessels modeled by non-linear constitutive law does not allow for real-time performance. To go around this limitation, a real-time co-rotational linear composite model of vascularized (Peterlík et al., 2012a) can be used for intra-operative registration.

Biomechanical models have the potential to lead to accurate non-rigid registration while producing a coherent visual deformations. Their limitations reside in their computing cost, although efficient and accurate methods have been proposed. In addition, a prior knowledge of the object physical properties is necessary but generally available from preoperative data.

## II.3 Vessel-based registration

In many imaging modalities, vascular structures are or can be made visible but the tissue intervascular space is usually homogeneous and poorly differentiated. Given that vessels are natural landmarks well distributed throughout several organs, their properties and characteristics are essential for accurate vascular registration. However, the relative motion or deformation makes the vascular matching locally ambiguous, because neighboring vessels usually have similar shape and intensity.

The registration accuracy is also deteriorated in the presence of excessive noise or when the multi-modality image intensity differs (which occurs with intra-operative modalities) because detected features or similarity metrics become less reliable.

There are many vessel registration algorithms for different applications and modalities that have been developed within the last decades using various cost functions, vascular models and geometric transformations. There is no proof that an algorithm performs well under completely different circumstances. Certain applications require additional properties of the transformation, such as a periodic motion for the cardiac interventions.

Matl et al. (2017) has reviewed several vessel registration algorithms. The following sections focus on the approaches that non-rigidly register 3D images, directly using vessels information. First, the algorithms that incorporate vessel information into an intensity-based. Then, the algorithms that extract and use the vessels as intrinsic features for registration are presented, including graph matching approaches and hybrid registration.

## II.3.1 Intensity-based registration of vascular images

Intensity-based approaches use all the information in the images, therefore it is reasonable to expect that they are more accurate than feature-based methods. However, intensity-based methods are limited when registering homogeneous and ambiguous intensities of the predominant inter-vascular tissue, because these methods work better when there are distinctive image intensities for several tissue types. Moreover, intensity-based registration is computationally more expensive.

Suh et al. (2010) encoded a weighting factor to modify the MI similarity measure to give preference to vascular structures. This weighting is defined with a vessel detection algorithm that generates a vesselness image (probability of having a vessel at any given voxel) from MRI. Even if the vessels are considered, they are only used locally to evaluate the matching criteria. This local based criteria is not enough to correctly handle the case of ambiguous matching of contiguous vessels. This ambiguity is common when matching dense, noisy or large deformation vasculatures.

Robben et al. (2012) assumed that deformed vessels can bend but will hardly change their length. Thus, they integrated the geodesic distance from every vessel voxel to a manually selected landmark as an extra feature. Then, they used MI and SSD similarity metrics for the intensity and distance features, respectively. This avoids local optimum and speeds up the optimization. However, the algorithm requires constant and accurate vessels length and it can not handle topology changes. As commonly done, the previous two intensity-based registration methods use first a rigid initialization and then a FFD B-splines deformable registration.

### II.3.2 Vessels as features for registration

Intensity-based registration cannot deal with very different image appearances and needs initialization. Instead, feature-based methods can handle these limitations but require the identification of landmarks and correspondences between the pre- and intra-operative images. Landmark extraction is not much studied in medical images, given that they are not as rich in details as natural images.

Still, being present in many anatomical structures, vessels can be used as features for multi-modal image registration. The sparseness, multi-scale geometric properties, and network configuration of the vessels may make vessel-based registration methods faster and more broadly applicable than intensity-based registration methods. Vessels are often well distributed throughout an organ and thereby capture deformations within that organ unlike surfaces and external landmarks that are poorly correlated with internal deformations. Thus, these intrinsic and natural features are a solution compatible with clinical constraints.

Yet, vessels cannot all be segmented or visible in the images, and therefore are less dense in certain areas. For this reason, it is still required an accurate interpolation method that does not lose much accuracy when the distance from landmarks increases.

When image modalities or acquisition parameters change, the number, portions, lengths, and widths of vessels visible in the images differ and hence the vascular network will appear to change. Even more significant, vessels undergo non-rigid deformations. Moreover, feature-based approaches have to cope with segmentation errors.

The following feature-based methods can be grouped in two classes: Centerline-based methods which only use the centerline points for registration but not the centerline connectivity and graph matching methods that exploit the vessel topology during the registration. Finally, hybrid vessel-based registration methods are presented.

#### Centerline-based methods

While global rigid registration is inaccurate to handle deformations during liver interventions, Song et al. (2015) assumed that local rigid and global deformable transformations produce a comparable local registration error. Thus, they segmented intra-operative b-mode US and extracted centerline points from a localized part of the liver. The intra-operative vessel points were locally registered with pre-operative CT vessels using manually selected landmarks and ICP alignment. This approach is not useful for procedures that require a global registration and probably there are situations with large local deformation where rigid registration is not accurate enough.

The following methods attempt to handle deformation. Lange et al. (2003) and Reinertsen et al. (2007) segmented vessel centerlines in preoperative (MRA or CTA) and intra-operative (Doppler 3DUS) images. They both required an initialization and then they used two modified ICP matching algorithms one for rigid and another for deformable registration. While Lange et al. (2003) used B-splines transformation and user-defined distance threshold to reject outliers, Reinertsen et al. (2007) used a thin-plate spline transformation and least trimmed squares robust estimation to reject outlier points. In both cases, Doppler ultrasound suffers from low acquisition rates and artifacts that can disrupt the centerlines extraction algorithm. Moreover, the deformation was small and the segmented vessels density did not cause significant matching ambiguity, making it easier to discard outliers.

Morin et al. (2017) developed an approach to compensate for craniotomy-induced brain-shift. First, a biomechanical model including boundary conditions is constructed from pre-operative MRI. Then, the vessels and the probe's footprint are extracted from intra-operative US. Finally, relying on a linear constitutive law, a constrained-based co-rotational simulation is used to register both pre and intra-operative vessels and the US probe footprint with the model's brain surface. Since the vessels are spread out over the volume of interest, the mechanical model accurately interpolates intra-vascular tissue deformation. However, this automatic method is limited to deformations smaller than 8 mm and requires initialization.

### Vessels graph matching overview

The previous vessel-based algorithms directly match the centerline points and avoid dealing with scarce and erroneous topological information. A popular way to introduce structural constraints in feature registration is graph matching (GM). Graph-based methods rely on the topological relationship determined by branching (bifurcation) points in the anatomical tree structure. Therefore, robust detection of branching points is critical for the registration performance.

For mono-modal registration of high quality images, GM algorithms based on vascular or airway structures have been developed, for example Tschirren et al. (2005) and Charnoz et al. (2005). However, the topology and shape of pre and intra-operative vascular graphs are very different due to deformation, image quality and feature extraction. This makes GM challenging and only few methods (for example Moriconi et al. (2018) and Serradell et al. (2015)) are able to match deformed and topologically diverse graphs. Section IV.1 presents brief descriptions and limitations of relevant GM approaches (Leordeanu et Hebert, 2005; Zhou et De la Torre, 2015; Torresani et al., 2008; Pinheiro et al., 2017) and the mentioned vascular GM methods.

### Hybrid vessel-based registration methods

The following hybrid methods try to exploit the multi-scale geometric properties and network configuration of the vessels with a model-image registration approach. First, Aylward et al. (2003) extracted, from the source image only, a tubular model of the vasculature using a ridge traversal technique. Then, assuming that blood vessels have high intensity, the similarity metric is the sum of the target image intensities that are inside the transformed tubular model. Thus, this can be applied across several imaging modalities. Finally, the parameters of the rigid transformation are optimized to maximize this metric.

Using the previous tubular model, similarity metric and rigid alignment as an initialization, Jomier et Aylward (2004) combined linear transformations in a hierarchical approach obtaining a piece-wise rigid transformation for each branch in the vessel. The alignment was then further refined with a deformable registration method. However, it seems unlikely that this method handles intra-operative alignment ambiguities produced by large network changes or large deformations.

## II.4 Conclusion

The multi-modality registration techniques presented have shown interesting results however they are not applicable in our context as they can not deal with very noisy and incomplete images, can not recover large deformations or require reliable initialization.

Deformable image registration for multi-modality intra-operative large deformation is challenging. In the case of images with vessels, a promising deformable registration approach is to use these vascular features together with a pre-operative biomechanical model. Given the specific requirements of our intra-operative registration we decided to use GM methods. Thus, Chapter III highlights the properties and characteristics of the extracted graphs and Section IV.1 presents a review GM methods.

Chapter III

# Vessels segmentation and representation

Graph structures accurately represent vessels in multiple image modalities. Therefore, the matching methods developed in Chapter V use graphs as features to achieve multi-modal registration.

Graphs are automatically extracted from CTA, CBCT and 3DUS image modalities. The extraction is described in two sections. First, the Section III.1 describes the model-based vessel segmentation (MBVS) (Smistad et al., 2014) and the specific processing pipelines used for each image modality. Then, the Section III.2 describes how the centerline and graphs are generated from the vessel segmented images (Plantefève et al., 2017). The description of these methods helps to understand the characteristics of the graphs obtained. These characteristics are important because they directly affect the computation time and accuracy of matching algorithms.

The Section III.3 shows the generated graphs from real data. It presents the possible false detection, incompleteness, disconnectedness, and inaccurate characteristics of intra-operative graphs. The extraction methods presented do not require any user interaction for processing the intra-operative data. However, the Section III.3 assesses how well the pipelines comply with intra-operative timing constraints, especially the shortcomings of US segmentation. Finally, the Section III.4 summarizes the obtained graph characteristics that the matching algorithms have to handle.

## III.1 Vessels segmentation

Segmentation of vessels from noisy intra-operative images belongs to an active area of research. State of art machine learning segmentation methods usually need large training datasets (Moccia et al., 2018). This is out of this thesis scope, thus other competitive and recent segmentation approaches were used. These fully automatic methods allow us to test our matching algorithms in realistic situations.

The Section III.1.1 describes the model-based vessels segmentation (MBVS) used (Smistad et al., 2014). This method is the main component of the modality specific pipelines implemented for the segmentation of vessels. The Section III.1.2 describes the specific pipeline used for segmenting the CTA and the CBCT images. The Section III.1.3 describes the 3DUS vessels segmentation pipeline, which includes the necessary speckle filter.

### III.1.1 Model-based vessels segmentation (MBVS)

All the intra-operative and pre-operative segmentation pipelines use the real-time model-based segmentation (Smistad et al., 2014). This method efficiently computes the Gradient Vector Flow (GVF), finds an estimate cross-sectional plane of the vessel, fits a circle on the vessel contour and finds the centerline with a ridge traversal method. The following description of the method's parts highlights its modality dependent parameters.

- **Preprocessing.** First a lower and upper thresholds ($I_{min}$ , $I_{max}$) remove unnecessary gradient information. This is especially useful for CTA and CBCT, which have a large range of intensity values. Then image noise is blurred with Gaussian smoothing with the standard deviation ($\sigma$).

  Afterwards, the gradient vector field is created and normalized using a threshold ($V_{max}$) for contrast invariance. The level of contrast and noise in the image determines the required value of $V_{max}$ . For example, CTA image has higher contrast to noise ratio, so a higher $V_{max}$ is used, while the lower CBCT contrast to noise ratio requires a lower $V_{max}$.

- **Gradient vector flow.** This tube detection method, as many others, uses the Hessian matrix. This matrix needs gradient information present in the center of the tube to detect it. However, thick tubes don't have gradient information in the center. The Gradient Vector Flow (GVF) propagates the gradient information to the center while preserving features. The GVF creates scale-invariance of tube detection filters and make the segmentation less sensitive to noise and vessels contrast and size (Bauer et Bischof, 2008).

- **Tube detection filter (TDF)**

  This part detects tubular structures and calculates a probability that a specific voxel is inside a tubular structure. First, the eigenvectors of the Hessian define the cross-sectional plane of the tubular structure. Then, the TDF fits a circle and defines how well it fits the gradient information (Krissian et al., 2000).

The circle fitting starts with the minimum radius ($r_{min}$) and is increased by a step ($r_{step}$) until it reaches the maximum ($r_{max}$).

The GVF eliminates the gradient information of some small tubes with low contrast. Thus, the TDF runs twice, once on the initial vector field to identify the small low-contrast vessels (using a small radius $r_{min}$) and once with the GVF vector field to identify the vessels smaller than the maximum radius ($r_{max}$). The tube detection of large and small structures uses two amounts of Gaussian blur ($\sigma_{small}$ and $\sigma_{large}$).

- **Centerline extraction** The method does a ridge traversal in the TDF results to extract the centerline (Bauer et Bischof, 2008). Then, from graph component labeling, unconnected centerlines that are shorter than the threshold ($L_{min}$) are filtered.

- **Segmentation** Smistad et al. (2014) proposed two segmentation approaches. The first one uses the centerlines as seeds for a parallel region growing procedure. The second segmentation targets noisy Doppler 3DUS. This approach defines a sphere in each point of the centerline using the radii found by the circle fitting. Then, all voxels inside the spheres are segmented as vessels.

This method already results in vessel segmentation. However, the intra-operative data segmentation is often noisy and incomplete. To improve these results, the following sections present implemented modality specific processing pipelines. The centerlines detected by the MBVS method are noisy. Thus, the graphs to be matched are generated (as detailed in Section III.2) from the segmentations obtained with modality specific pipelines.

### III.1.2 CTA and CBCT segmentation

The pipeline, shown in Fig III.1, segments the vascular tree in both the pre-operative CTA and the intra-operative CBCT images. The following description of each pipeline's component summarizes the modality dependent processing.

- *MBVS high* and *MBVS low.* Using different vessel detection parameters, the MBVS method (Smistad et al., 2014) segments twice the input image. The segmentation using the *MBVS high* parameters results in a more complete but noisy segmented vessels image $Im_{high}$. While, using the *MBVS low* results in a less noisy but more incomplete segmented image $Im_{low}$. The first and second part of Table III.1 list the CTA and CBCT parameters used, respectively.

- *Liver labels.* The Fig. III.2 shows the vessels (in red) and tissue (in green) labels that form the liver labels image. The low vessel sensitivity segmentation

**Table III.1:** MBVS segmentation parameters for each image modality

| Parameter | $I_{min}$ | $I_{max}$ | $V_{max}$ | $\sigma_{small}$ | $\sigma_{large}$ | $r_{min}$ | $r_{max}$ | $L_{min}$ |
|---|---|---|---|---|---|---|---|---|
| $CTA_{low}$ | 150 | 180 | 0.01 | 0.3 | 1.0 | 2.0 | 15 | 20 |
| $CTA_{high}$ | 120 | 200 | 0.01 | 0.4 | 1.0 | 1.0 | 15 | 10 |
| $CBCT_{low}$ | 100 | 300 | 0.01 | 0.4 | 1.0 | 1.5 | 15 | 10 |
| $CBCT_{high}$ | 70 | 340 | 0.01 | 0.5 | 1.0 | 1.0 | 15 | 20 |
| $CBCT_{MBVS}$ | 90 | 200 | 0.4 | 0.2 | 1.0 | 1.0 | 15 | 20 |
| $US_L$ | 900 | 1450 | 0.06 | 2.0 | 5.0 | 5.0 | 20 | 5.0 |
| $US_M$ | 900 | 1450 | 0.03 | 4.0 | 6.0 | 5.0 | 15 | 1.0 |
| $US_S$ | 900 | 1450 | 0.08 | 0.5 | 2.0 | 1.0 | 7.5 | 5.0 |

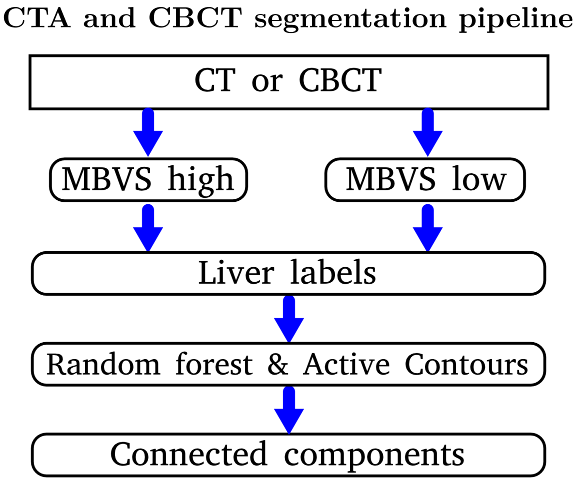

**Figure III.1:** CTA and CBCT segmentation pipeline

image $Im_{low}$ is directly assigned as the vessel label. While, the tissue label is defined as $Im_{tissue} = \neg(Im_{low} \parallel Im_{high} \oplus k_3) \ominus k_6$ where, $k_n$ is a spherical structuring element of $n$ voxels used in the erosion and dilation binary morphological operations.

- *Random forest and Active contours.* ItkSnap uses the liver labels image to train, automatically, a random forest classifier. It uses the coordinates for training and 500 trees with a maximum depth of 100. Then, the posterior probability classification result is used to compute the speed image that drives the vessel segmentation based on the active contours (Yushkevich et al., 2016).

- *Connected components.* The contrast injection acquisition allows the visual-

**Labels image for random forest and active contours segmentation**

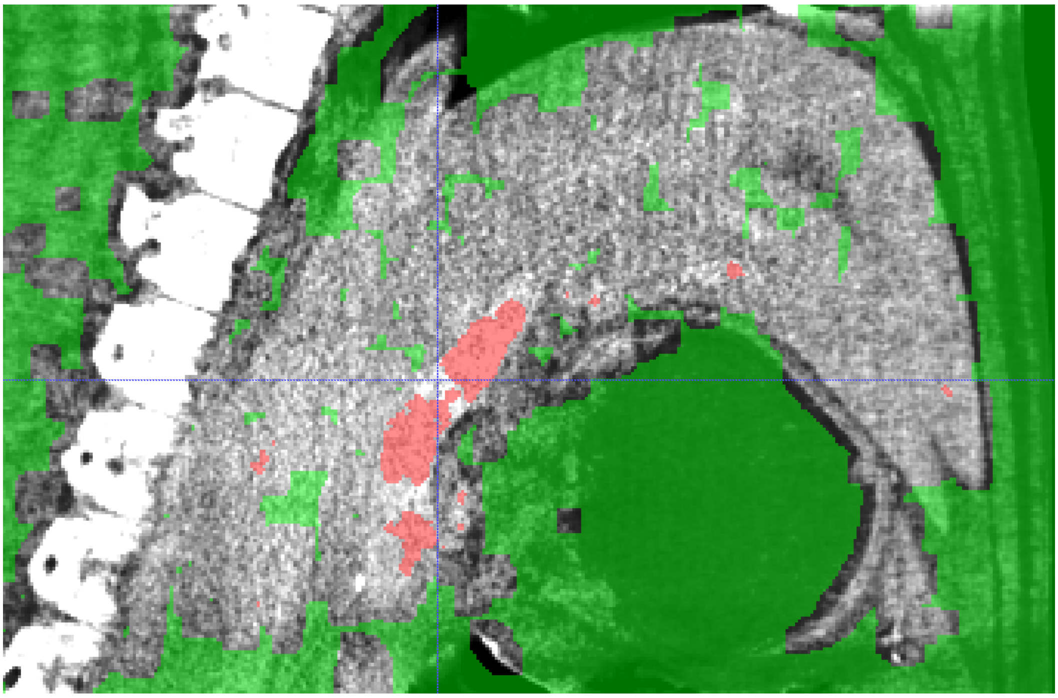

**Figure III.2:** Liver labels image has the vessels in red and the tissue in green. It is the input of the *Random forest and Active contours* component.

ization of the vessels in both the CTA and CBCT images. In the CBCT, due to its low contrast to noise ratio, only the PV is clearly visible. Thus, the biggest connected component is the PV. With CTA, the PV and HV are usually both visible. Sometimes, both veins are connected at the end of some thinner vessels. When this happens the PV and HV are manually disconnected. Finally, the two biggest connected components are the hepatic and portal veins.

### III.1.3 US segmentation

There are several US modes that provide visualization of vessels. Power Doppler US mode is straightforward to segment, but it usually misses several vessels due to its lower spatial resolution, low sensitivity to small flow velocities and high susceptibility to motion artifacts (Lindseth et al., 2013; Schneider et al., 2011). More complete vessels are visible in B-mode 3DUS, thus this mode is used. However, it is more complicated to segment because it has low contrast to noise ratio and speckle noise.

Either with B-mode or Doppler, the segmentation methods proposed by Smistad et al. (2014) did not result in enough detected vessels for automatic graph matching. The pipeline shown in Fig. III.3 segments B-mode 3DUS filters some of the specular noise and allows to obtain better vessels segmentation. The following description of each pipeline's component summarizes the US segmentation.

- *Mask Generation.* The background of the image is segmented using region growing, and the inverse is considered as the US mask. Also, the US image intensity is scaled 100 times to fit better the GPU numerical type (int16) range and avoid rounding errors in the GPU processing.

- *Speckle anisotropic filter.* The 3D US data is processed using the anisotropic diffusion filter with memory based on speckle statistics (ADMSS) (Ramos-Llorden et al., 2015). This filters the speckle and motion artifacts inside the vessels but preserves it in the liver parenchyma.

- *MBVS L, M and S.* The speckled filtered US image is segmented three times using the MBVS method (Smistad et al., 2014) with different vessel detection parameters. The Table III.1 lists all these parameters. The *MBVS L* component segments thick (radii from 5 to 20 mm) and long (larger than 5 mm) vessels with high contrast, this results mostly in an incomplete, unconnected but correct segmentation image $Im_L$. The *MBVS M* component segments medium thickness vessels (radii from 5 to 15 mm ) with less contrast, however it uses higher smoothing to avoid some noise. This component results in the image $Im_M$. Some of these medium vessels are correct while few others are due to noise. Finally, *MBVS S* component segments thin (radii from 1 to 7.5 mm) and long (larger than 5 mm) vessels with high contrast. The results is the image $Im_S$ with few disconnected small vessels correctly detected and several false detection due to the low smoothing ($\sigma$) of noise. The following processing joins these images, avoiding the noisy segmentations while maintaining the correct ones.

- *Largest CCs.* The connected components (CCs) of $Im_L$ are computed. For each CC its length (the longest edge of its oriented bounding box) and volume are computed. The CCs that are longer than 2 cm and that have a volume larger than 8.0 $cm^3$ are kept in the image $Im_{Lcc}$. These are frequently disconnected parts of the HV and PV. However, some of these components are segmented due to noise.

- *Hole filling.* The $Im_{Lcc}$ and $Im_M$ are joined ($Im_{Lcc} \parallel Im_M$). This joined segmentation has several holes, due to the large image intensity variation within the vessels. Thus, a hole filling process (Lehmann, 2007) is applied and results in $Im_{HF}$.

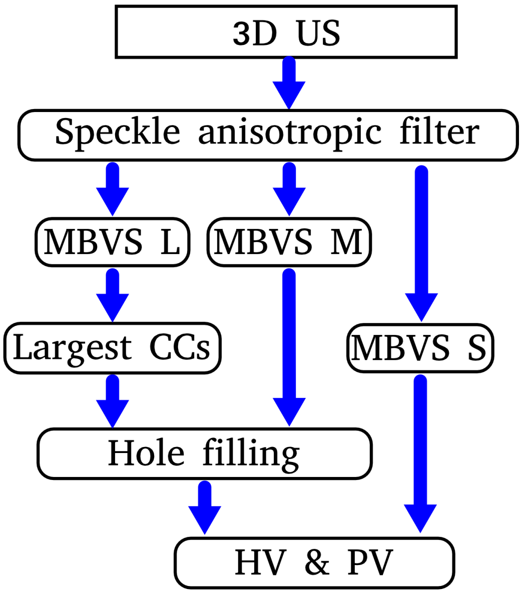
**Pipeline for 3DUS vessels segmentation**

**Figure III.3:** Pipeline for 3DUS vessels segmentation

- *HV & PV*. Again, the CCs of $Im_{HF}$ are computed. The noisy connected parts are usually flat and round so these parts are filtered out (Lehmann, 2007). The second longest CC is the PV and is joined with the $Im_S$ and results in the final PV image ($Im_{PV}$). The other (all except the second longest) CCs are usually disconnected parts of the HV and are also joined with the $Im_S$ resulting in the $Im_{HV}$

## III.2 Graph generation

From the vessels segmentation, each vein (maintaining the portal and hepatic differentiation) is converted to a graph $\mathcal{G} = (\vec{X}, \vec{E})$. Where $\vec{X}$ is the set of nodes (tree bifurcations) and $\vec{E}$ is the set of edges. The disconnected parts of the segmentations, especially in the 3DUS, can improve the registration. However, the generation and matching of disconnected graphs require several modifications in the complete pipeline. Currently, the graph is extracted only from the biggest connected component of each vessel.

The graph is obtained from a centerline extraction method (Plantefève et al., 2017), which is an extension to the method presented by Verscheure et al. (2013). The method uses the shortest distance from the boundary to each segmented voxel ($DFB$) and the Dijkstra minimum cost spanning tree to generate the graph. At the generated graph points ($p$), the $DFB(p)$ is kept as an attribute and used as the vessel radius.

The graph obtained is actually a rooted tree. Thus, in both the pre-operative and intra-operative image the root is determined automatically. First, the root is the segmented voxel that is closest to the image origin and it is used to generate a first tree. From this tree, the thickest centerline point is considered as the new root, and the final tree is generated from here.

An important parameter of the method is the branch minimum length factor ($L_{TH}$). This parameter rejects from the graph the branches starting at $p$ that have a length smaller than $L_{TH} \times DFB(p)$. This allows extracting short branches from thin vessels, while rejecting false short branches that are due to noise in thick vessels. The branch minimum length factors used are $L_{TH} = 1.5$ for the CTA and CBCT and $L_{TH} = 2.0$ for the US . Finally, each branch of the trees is smoothed and sampled using a Bezier function.

## III.3 Segmentation and graph extraction results

Porcine pre and intra-operative images were acquired during two experimental sessions, in the first session (PA) one CTA and one CBCT images were acquired, while in the second session (PB) there were one CTA, two 3DUS and one CBCT. The CTA and CBCT images were acquired using contrast agent injection. The characteristics of each of these images are summarized in Table III.2 The vessels of these porcine images (CT, CBCT and 3DUS) were segmented using the modality specific pipelines previously presented and the parameters listed in Table III.1. Then, from these segmentations graphs were extracted. These results are presented for two images of each modality. Then, a summary of important properties of the pre and intra-operative graphs to be matched are compared.

### III.3.1 CTA

Most of the portal and hepatic veins are visible in each pre-operative CTA image. The obtained segmentations and graphs are complete, accurate, and almost noiseless. The Fig. III.4 and Fig. III.5 show the results of sessions PA and PB, respectively.

### III.3.2 CBCT

In each intra-operative CBCT image, most of the PV is visible. From the CBCT image of session PA, two segmentations were done using only the MBVS method (Smistad et al., 2014). The first segmentation($MBVS_{0.4}$) used the $CBCT_{MBVS}$ parameters from Table. III.1, while the second ($MBVS_{0.3}$) used almost the same

**Session PA porcine CTA segmentation**

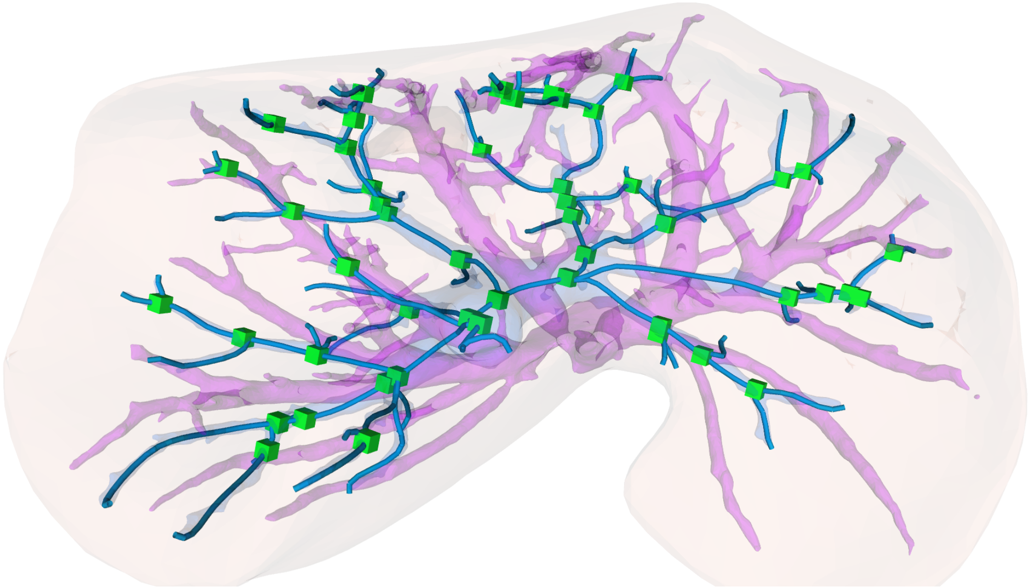

**Figure III.4:** The automatic vessels segmentation and graph extraction from CTA of session PA. Only the HV segmentation is shown and not the graph, given that the corresponding intra-operative graph is not visible in the CBCT image. The PV graph (in blue) has 60 bifurcations (green cubes).

parameters except for $V_{max} = 0.3$. A third segmentation ($CBCT_{pipe}$) was done using the complete pipeline presented in Section III.1.2. The Fig. III.6 shows these segmentations and their respective graphs.

The cross-sectional planes of Fig. III.7 show that the $CBCT_{pipe}$ segmentation is more complete and has less noise. While, the MBVS method alone results in less complete and noisier graphs. Even with the same image and using similar segmentation parameters, the corresponding centerlines and bifurcations are not detected in the same position. This affects the path length along the edges between two bifurcations (geodesic distance), specially where there are thick vessels, as shown in the blue ellipse of Fig. III.7.a.

A second CBCT image, obtained in session PB, is much noisier and has less contrast than the previous one. As shown in Fig. III.8, the segmentation has mostly thick principal vessels and some medium branches are missing. From the smaller branches segmented, it is likely that some of them are due to noise, as shown in Fig. III.9.

The CBCT graphs and its obtained features are not highly discriminant for matching. Moreover, due to the noisy and missing branches, accurate graph matching is challenging.

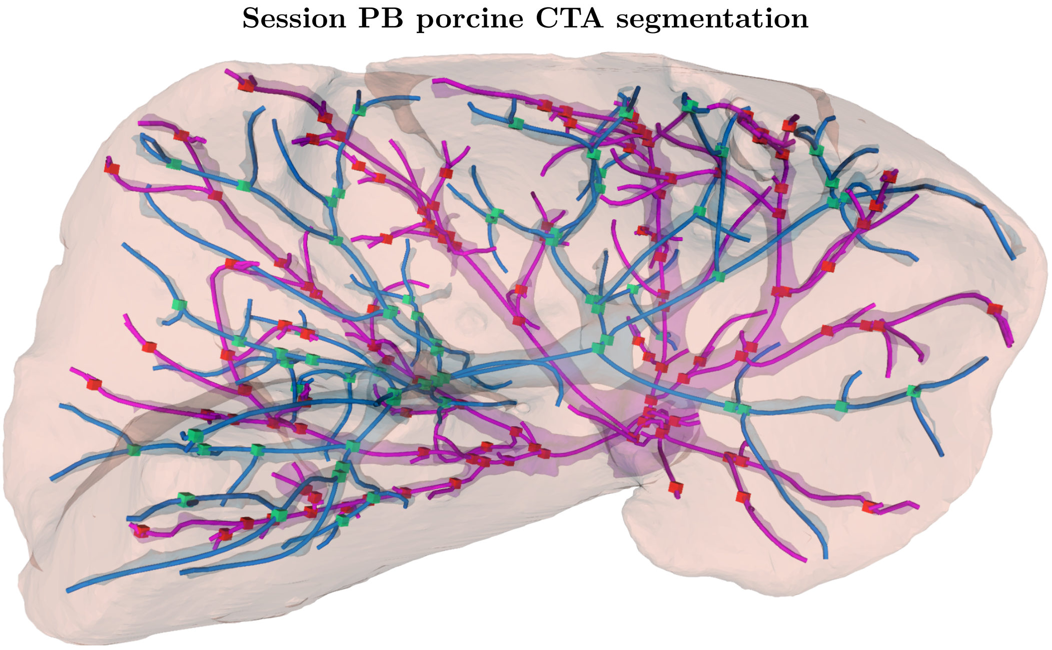

**Figure III.5:** Automatic vessels segmentation and graph extraction from CTA of session PB. The HV (in magenta) and the PV (in blue) graphs have 118 (red cubes) and 66 (green cubes) bifurcations, respectively.

### III.3.3 3DUS

The 3DUS images were acquired digitally using standard imaging preset for the abdomen. The PV and HV are partially visible in both of the acquired 3DUS. As often done, voxel scale is assumed isotropic (Chen et al., 2015). It was obtained by manually selecting 5 pairs of landmarks in the US and the corresponding ones in pre-operative CT. The selected landmarks are reliable and unambiguous features from thick parts of the PV. Moreover, the distance between the landmarks pair is smaller than 1.8 cm and is considered constant between both image modalities. From the average ratio of the Euclidean distances between landmarks, the resulting US scale is 0.28 mm/voxel.

In a real scenario, the scaling should be obtained with ultrasound calibration. The anisotropic calibration (Chen et al., 2015) is a good option. It considers the physical separation of transducer elements and the speed of sound in the medium. However, even with this anisotropic calibration, the US scale distortion remains due to the variable speed of sound in the scanned medium. Specially, further from the transducer where the distortion accumulates.

Besides the US scale distortion, image noise and artifacts are an important issue considered. Without speckle filtering, the segmentation is very noisy and incom-

**Comparison of CBCT segmentations and graphs extraction**

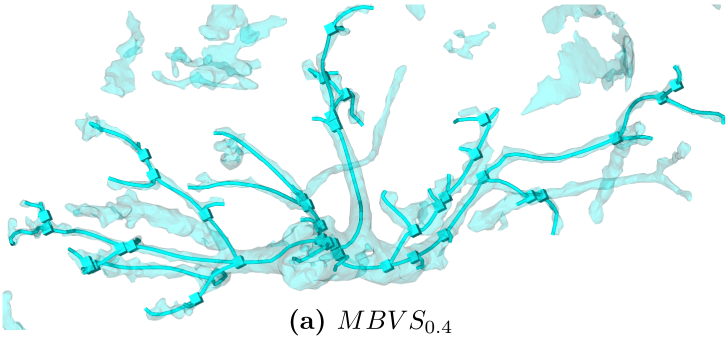

**(a)** $MBVS_{0.4}$

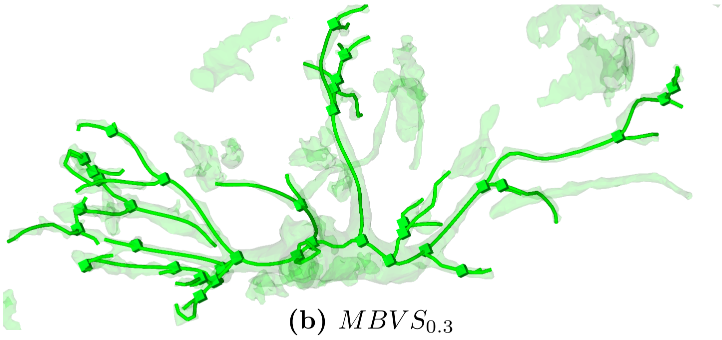

**(b)** $MBVS_{0.3}$

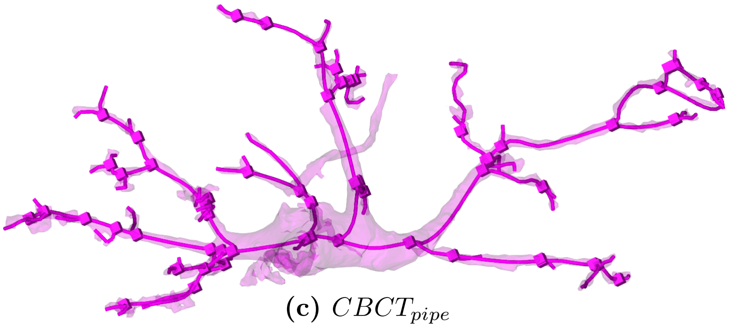

**(c)** $CBCT_{pipe}$

**Figure III.6:** From the CBCT acquired in session PA, the obtained segmentations $MBVS_{0.4}$, $MBVS_{0.3}$ and $CBCT_{pipe}$ have 36, 38 and 47 bifurcations plotted with cubes, respectively.

plete. The ADMSS filter (Ramos-Llorden et al., 2015) improves vessels segmentation and allows extracting graphs for matching; however, its processing time was 15.4 hours. As an alternative the detail preserving anisotropic diffusion (DPAD) filtering (Aja-Fernandez et Alberola-Lopez, 2006) was tested, however the segmentation and graph obtained is worse than with ADMSS. This is a critical part of the segmentation US pipeline. The ADMSS filtering is far from complying with intra-operative timing constraints. This area is out of the thesis scope, and it is left as an open and important issue. It is likely that novel state-of-the-art methods,

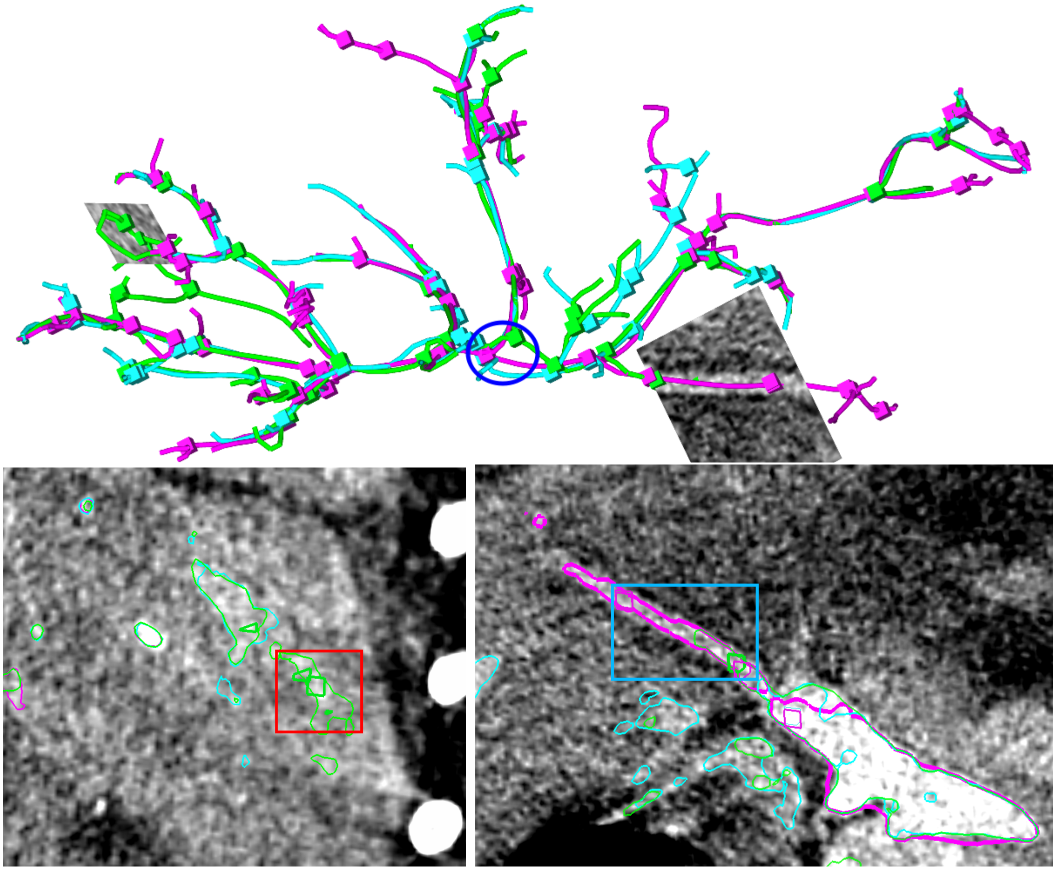

**Extracted graphs difference from the CBCT acquired in session PA**

**Figure III.7:** Inside the blue ellipse, the green cube bifurcation is detected far from the corresponding bifurcation in the other segmentations. This is an important variation of the centerlines position and the geodesic distances with respect to this bifurcation. The cross-sectional plane in the left shows that the $MBVS_{0.3}$ graph (in green) detects some small vessel branches (inside the red rectangle) that are probably due to noise, while the $CBCT_{pipe}$ graph (in magenta) does not. The cross-sectional plane in the right shows that the $CBCT_{pipe}$ graph correctly detects the vessels inside the blue rectangle, while the other MBVS segmentations do not (better seen in the digital document).

similar to the segmentation presented by Smistad et Løvstakken (2016), allow to segment B-mode US images faster. Thus, it is assumed that it is possible to get similar US graphs within intra-operative timing constraints.

The Fig. III.10 shows the PV and HV obtained with the US segmentation pipeline presented in Section III.1.3. The HV and the PV graphs have 73 and 38 bifurcations, respectively. However, several of these bifurcations are due to noise. The Fig. III.10.a shows the segmentation obtained with the *MBVS S* component in

**Partial CBCT extracted graph**

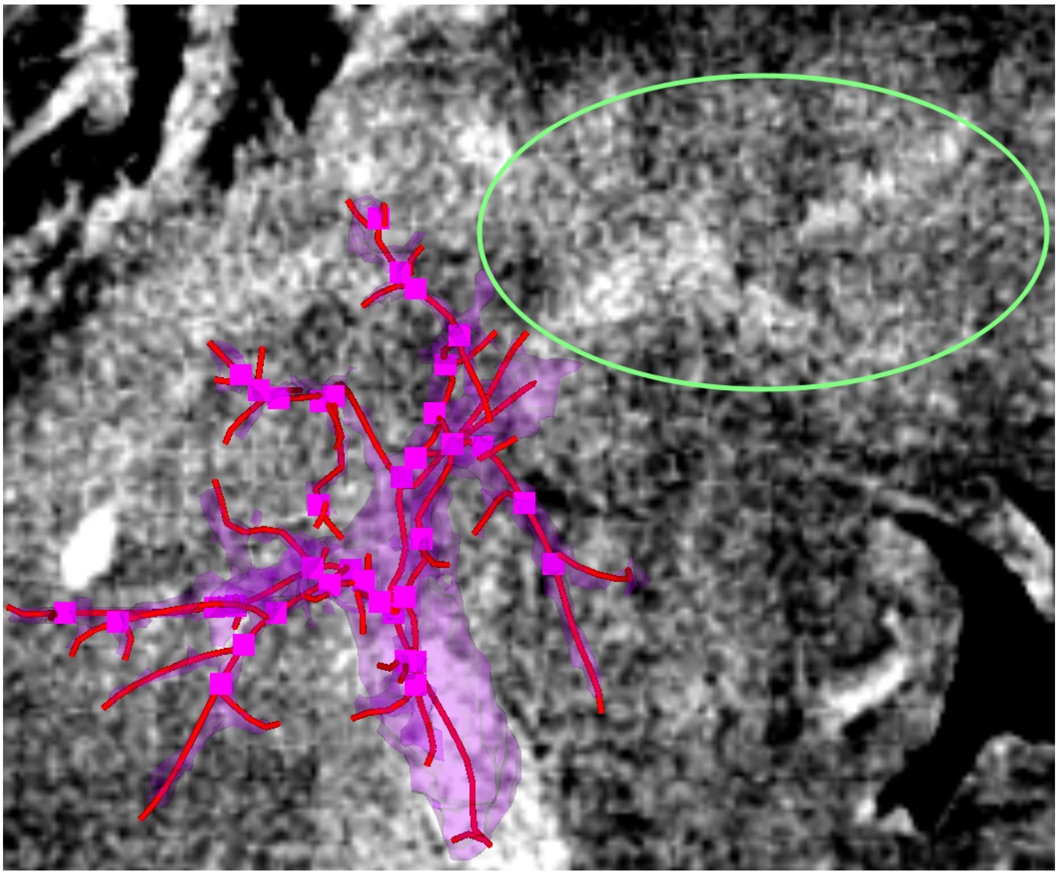

**Figure III.8:** The CBCT image, from session PB, has low contrast and is noisy. The segmented PV has mostly thick principal vessels. On the ellipse, a large disconnected branch is missing from the segmentation.

a brighter color. This part of the segmentation has mostly thin branches, and it is likely that several of them are due to noise. The cross-sectional plane in Fig.III.10.a and the red rectangle in Fig. III.10.b show an example of likely noisy segmentation. There are still enough correct branches detected that allow matching; however, the noise makes it very challenging.

The Fig. III.10.c shows a segmentation error, where a branch is disconnected from the principal HV (green circle) and it is connected by some noisy segmentation (red circle). This creates a large change in graph topology and a large variation in the geodesic distances between bifurcations in this branch and the rest.

A second US image was obtained in experiment session PB; it has less contrast than the previous. The segmentation detects less correct small branches and more

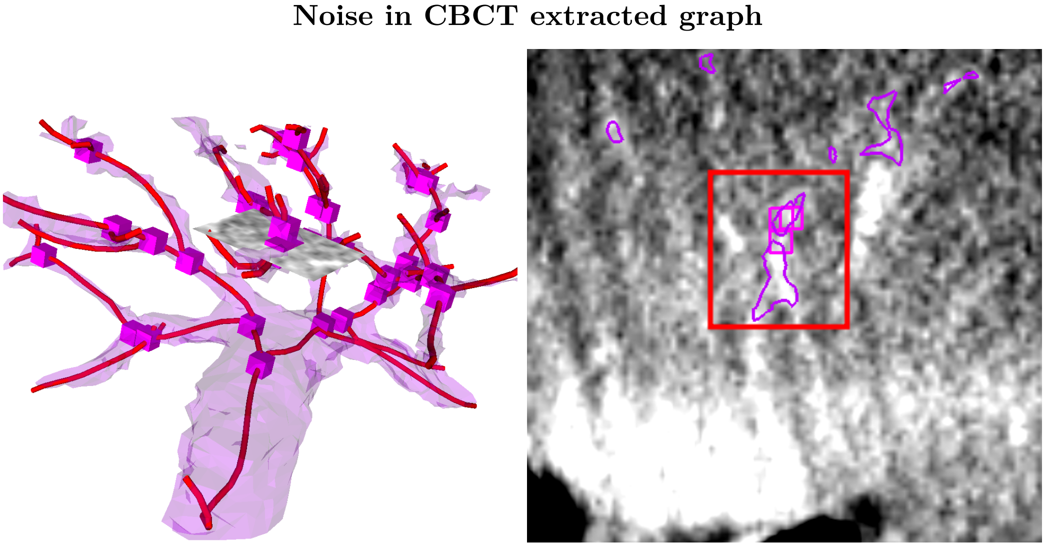

**Figure III.9:** The CBCT from session PB where some small branches are probably due to noise. This is the case of the cross-sectional plane with three bifurcations (pink squares) really close to each other.

noise, as shown in Fig. III.11. It also results in a disconnected segmentation of the HV. The disconnected branches imply a big challenge during matching because the geodesic distances to the other disconnected parts are unknown. This issue can be attenuated by the matching method proposed in Chapter V. However, the current graph extraction and matching implementations only handle connected graphs.

### III.3.4 Extracted graphs properties for matching

Four different porcine liver graph datasets are used to evaluate the matching methods. Each of the first two datasets, PA and PB which were respectively acquired from the corresponding sessions, has one CTA image acquired pre-operatively in supine position and one CBCT image acquired after pneumoperitoneum on flank position. In both modalities the portal vein is visible, however, the CBCT image has fewer portal vessel branches visible than the CTA (as shown in Fig. III.12) and several false branches were segmented due to noise (see figures III.7 and III.9). Each of the third ($PB_{UP}$) and fourth ($PB_{UH}$) datasets has one graph extracted from the preoperative CT and other from the intra-operative open surgery 3DUS. The intra-operative graphs are extracted from the first good quality and complete 3DUS acquisition shown in Fig. III.10. Where $PB_{UP}$ has the portal vein and $PB_{UH}$ has the hepatic vein graphs. The intra-operative conditions of all these datasets generated a large deformation. Table III.2 summarizes some of the graph properties relevant for matching.

**Table III.2:** The vessels characteristics of the porcine images.

| Porcine dataset | | Number of nodes | veins radii [mm] [min, max] | Vessels intensity [HU] $\mu \pm \sigma$ | Liver intensity [HU] $\mu \pm \sigma$ | Voxel size [mm] | Image size |
|---|---|---|---|---|---|---|---|
| PA | $CT_{PV}$ | 60 | [1.6, 10.3] | 194.2±19.9 | 135.7±20.9 | 0.559 | 344x236x280 |
| | $CBCT_{PV}$ | 47 | [1.2, 8.8] | 176.7±39.2 | 103.8±39.8 | 0.653 | 344x236x224 |
| PB | $CT_{PV}$ | 39 | [1.8, 7.5] | 189.1±23.4 | 117.0±25.2 | 0.770 | 344x184x256 |
| | $CBCT_{PV}$ | 36 | [1.1, 6.5] | 144.9±46.2 | 113.8±53.8 | 0.653 | 344x224x264 |
| $PB_{UP}$ | $CT_{PV}$ | 39 | [1.8, 7.5] | 189.1±23.4 | 117.0±25.2 | 0.770 | 344x184x256 |
| | $US_{PV}$ | 38 | [1.3, 6.4] | 1209.9±76.2 | 1284.8±379.8 | ≈ 0.28 | 560x452x604 |
| $PB_{UH}$ | $CT_{HV}$ | 118 | [1.8, 7.5] | 189.1±23.4 | 117.0±25.2 | 0.770 | 344x184x256 |
| | $US_{HV}$ | 73 | [1.2, 8.8] | 1179.7±79.2 | 1284.8±379.8 | ≈ 0.28 | 560x452x604 |

### Variation in pre and intra-operative graph features and properties

The Fig. III.12 shows the CTA and CBCT segmentations of the PV obtained in session PA; it also shows their vessels' radii color-mapped in the graphs. Similarly for session PB, the Fig. III.13 shows the PV segmentations and graphs obtained from CTA and US. The corresponding vessels have different radii in each modality. This is mainly because of the CBCT artifacts and lower signal-to-noise ratio, and because of US artifacts, distortion, and noise. In session PA, the radii range in the CTA is [1.6, 10.3] mm and in the CBCT is [1.2,8.8] mm. While in session PB, the radii range in the CTA is [1.8,7.5] mm and in the US is [1.3, 6.4] mm. Even if the corresponding vessels radii vary among modalities, it still is a "soft" discriminant appearance feature for matching.

Compared to pre-operative data, intra-operative extracted graphs commonly lack correct branches and add noisy ones. For example, the CBCT graph is missing a few branches on the right side of Fig. III.12. In addition, some small CBCT leaf branches on the left side are probably due to noise. This issue is even worse in US data as shows the Fig. III.13. On its left side, the US graph does not have several branches, which are outside the limited field of view. Moreover, several small US leaf branches are probably due to noise.

Another important issue is the position variation of corresponding bifurcations, especially in the principal thick branches. The Fig. III.12 shows an example. Here, the red arrows point to corresponding bifurcations. In the CTA case, this bifurcation coincides with the neighbor bifurcation pointed with the green arrow, while in the CBCT those corresponding bifurcations are 5.8 mm apart. The bifurcations position variation produces different geodesic distances in between corresponding bifurcations. For example in Fig. III.12, the geodesic distance in between the bifurcations pointed by the green arrows is 27.2 mm in the CTA and 21.1 mm in CBCT. Similarly, in Fig. III.13 the geodesic distance is 18.2 mm in the CTA and 26.1 mm in US. This important graph property has a large variation, and it becomes less discriminant when matching.

## III.4 Conclusion

The vessels segmentation methods used are perfectible and for the 3DUS it is assumed that novel state-of-the-art methods can obtain similar graphs within intra-operative time constraints.

The characteristics of the extracted graphs directly affect the matching problem complexity. The intra-operative graphs, especially the US ones, have several false vessel branches and thus have false bifurcations. This increases the matching computation time, due to the combinatory nature of matching. Moreover, the false vessels can be wrongly matched and decrease the quality of the registration.

At the same time, the matching methods rely on graph similarities to prune the combinatory search space. The pruning can be done using local appearance features like the vessels radii. However, the intra-operative graphs radii is only a "soft" discriminative feature. The geodesic distance between nodes is usually the main pair-wise similarity extracted from the vessels to reduce the search space. However, the generated graphs have inaccurate geodesic distances. Thus, these graphs' similarities are not enough to reduce the search space.

Despite these undesirable characteristics, enough information is available to register the pre and intra-operative graphs. The Chapter V shows how the matching method overcomes these limitations and correctly registers these graphs within the timing constraints. The generation and matching of disconnected graphs is a clear implementation improvement left for future work.

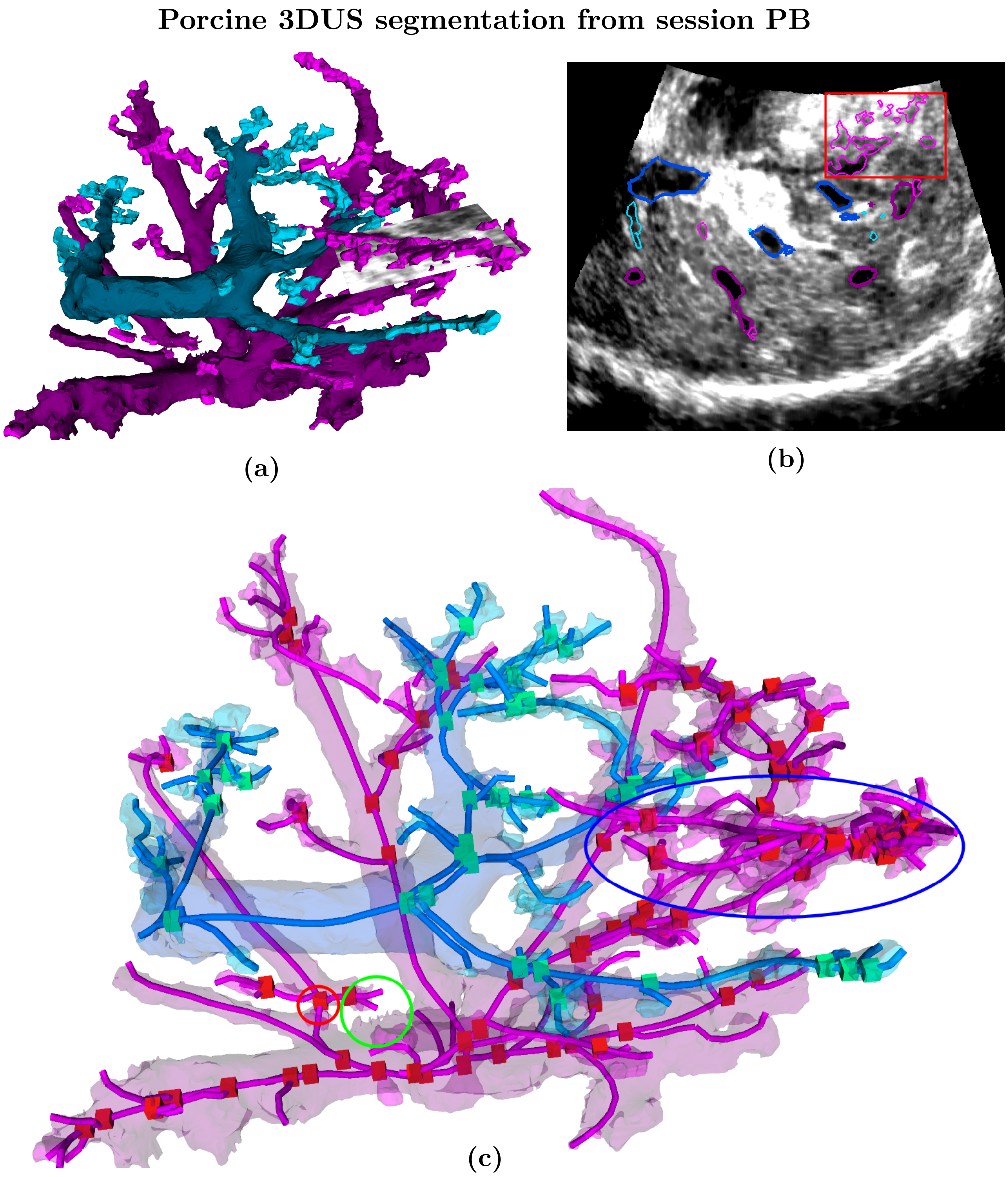

**Porcine 3DUS segmentation from session PB**

(a)

(b)

(c)

**Figure III.10:** Automatic segmentation and graph extraction from US. a) The HV and PV segmentations are shown in magenta and blue, respectively. In brighter color are the *MBVS S* segmentations which are prone to errors, as shown by the cross-sectional US plane. b) The likely noisy segmentation is inside the red rectangle in the complete cross-sectional plane. c) The extracted HV graph shows again high concentration of bifurcations and likely noise inside the blue ellipse. It also shows a topological segmentation error, where a branch is disconnected from the principal HV (inside the green circle) and it is connected by some noisy segmentation (inside the red circle).

**Disconnected porcine 3DUS segmentation**

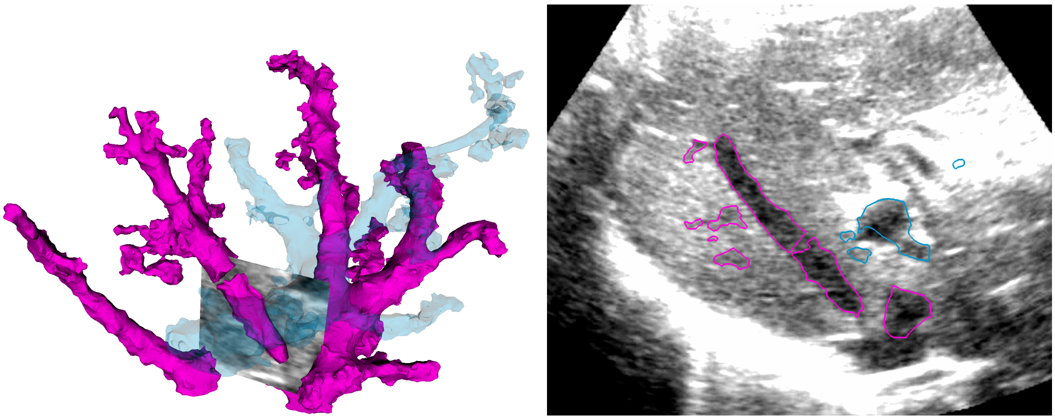

**Figure III.11:** The second US acquisition from session PB has less contrast than the first one. a) shows the 3D reconstruction of segmented vessels, where the HV (in pink) is disconnected into 3 parts. b) the cross-sectional plane shows where one branch of the HV is not segmented and disconnected from the principal vessel.

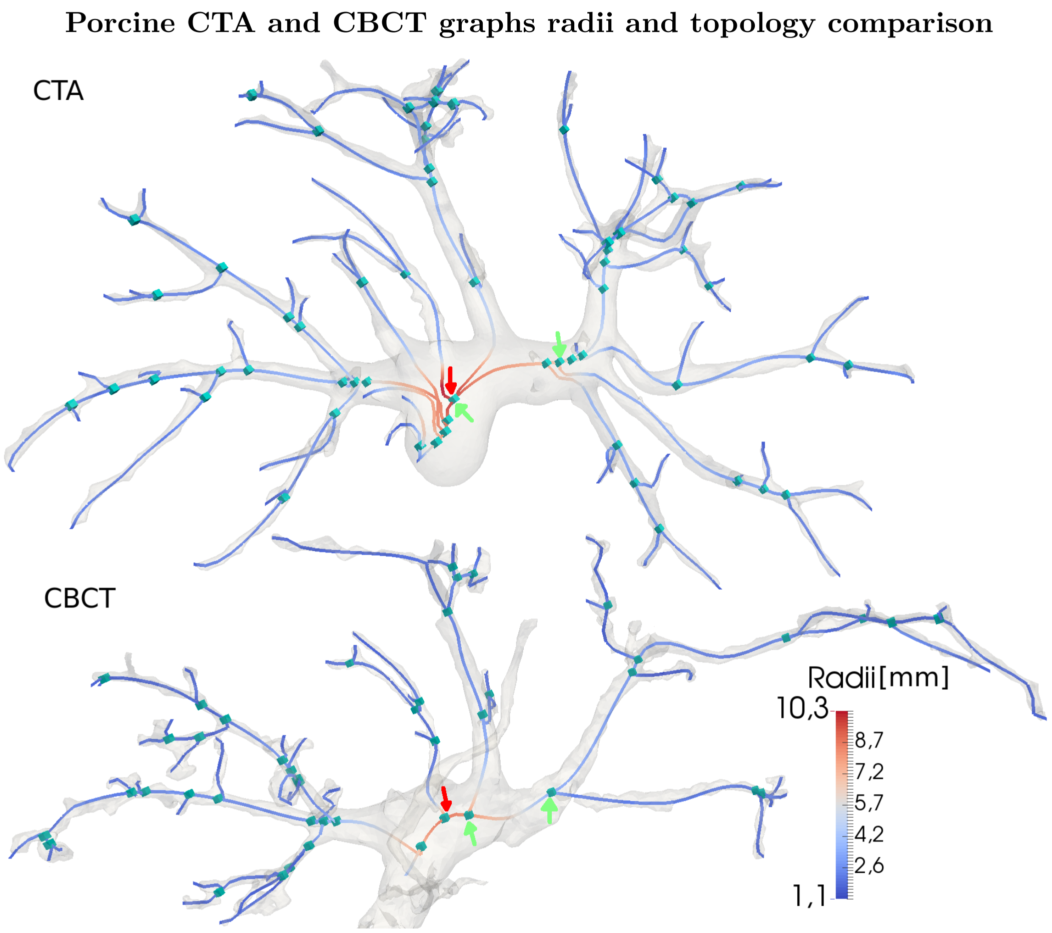

**Figure III.12:** CTA and CBCT segmentations of the PV, obtained from the session PA. Their respective graphs have color-mapped the radii. In each modality, the green arrows point at corresponding bifurcations, whose geodesic distances differ by 6 mm. The red arrows also point at corresponding bifurcations but their positions, with respect to the neighbor bifurcation (pointed by the green arrow), do not coincide.

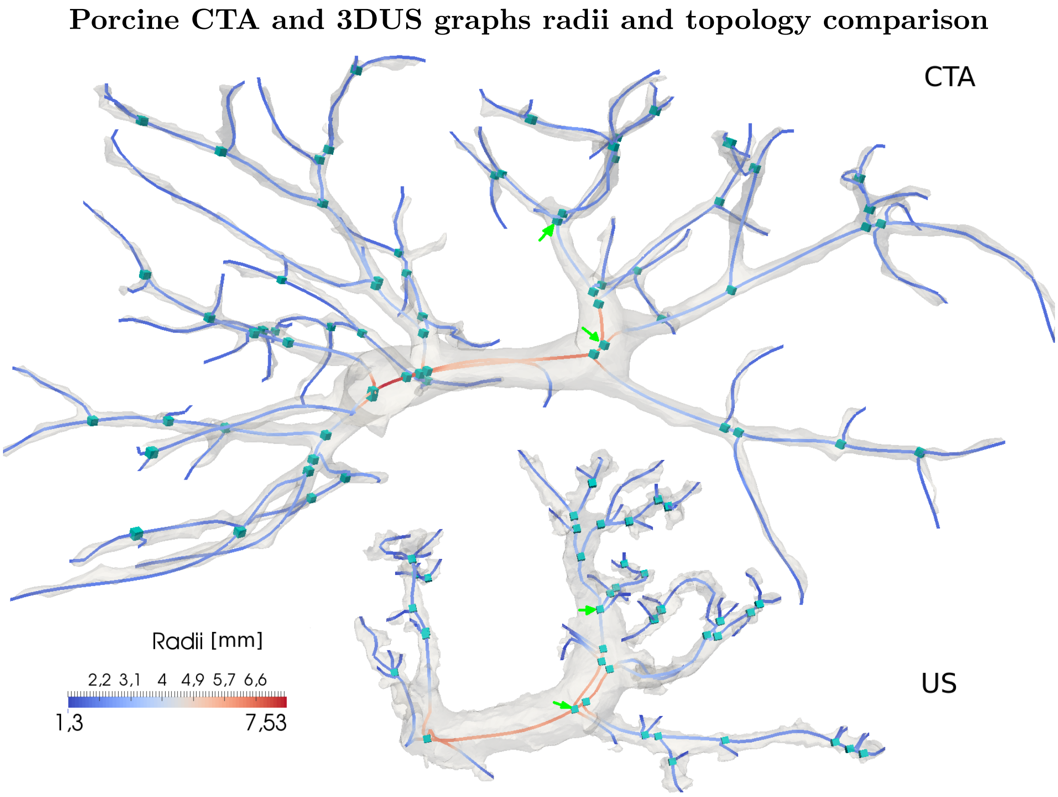

**Figure III.13:** CTA and 3DUS segmentations of the PV obtained from the session PB. Their respective graphs have color-mapped the radii. In each modality the green arrows point at corresponding bifurcations, whose geodesic distances distances differ by 7.9 mm.

CHAPTER IV

# Graph matching

Graph structures are common in medical images and can be obtained from blood vessels, airway trees, or neuronal fibers. Robustly registering such graphs is thus a key enabling technology for pre-operative planning, intra-operative navigation, follow-up or group-wise analysis (Matl et al., 2017). These tubular thin structures lack distinguishing local appearance features in bifurcations or edges. Thus, feature-based correspondence techniques are impractical. A more effective approach is to detect vascular graphs and use the geometrical and topological properties shared across modalities to match them.

The Section IV.1 is a brief survey of recent graph matching (GM) methods used in computer vision which rely on distinctive local appearance features. The Section IV.2 reviews relevant GM methods that deal with the lack of distinctive local appearance in vascular images. Still as shown in Section III.3, the intra-operative acquisition leads to very noisy, deformed, partial and topologically altered vascular graph and this makes the matching challenging.

From the reviewed methods, the GPR matching presented by Serradell et al. (2015) is the more appropriate according to the intra-operative conditions considered and so it is described in Section IV.3. However, this method has two critical limitations: high matching time and low accuracy with the considered data. To deal with the first limitation, the Section IV.4 presents an improvement of the method that reduces its computation time. Finally, experiments with synthetic and real data compare, evaluate and show the limitations of these GPR matching methods.

## IV.1 Graph matching state-of-the-art

In computer vision tasks, GM is crucial to establish correspondences between two sets of visual features, which are usually detected by descriptors (Lowe, 2004; Bay et al., 2006). Due to the lack of rich details in vascular images, these descriptors can not detect useful features. Instead, the vessels radii or shape at bifurcations are the local appearance features commonly used. Matching using only similarity between these local features might lead to undesirable results because they are usually not discriminative enough.

GM formulates the correspondence problem as solving the matching between two graphs. A graph $\mathcal{G} = (\vec{X}, \vec{E})$ is composed by the nodes $(\vec{X})$ and edges $(\vec{E})$ sets, where each node $(\mathbf{x}_i \in \vec{X})$ is a detected feature point in $\mathbb{R}^D$ and each edge $(\mathbf{e}_j \in \vec{E})$ connects two nodes. Besides local appearance of nodes, GM incorporates pairwise node similarities (e.g., edges length or orientation) which are important features when matching structural objects. This added pairwise information constraints the matching problem and allows to find better correspondences. Given that vascular images lack distinctive nodes local appearance, the euclidean or geodesic distances between nodes become a crucial pairwise similarity, which are commonly used in the methods described in Section IV.2.

This section is inspired from Zhou et De la Torre (2015) and similarly formulates the GM problem incorporating pairwise constraints as a quadratic assignment problem (QAP). Given a source $\mathcal{G}^S = (\vec{X}^S, \vec{E}^S)$ and target $\mathcal{G}^T = (\vec{X}^T, \vec{E}^T)$ graphs with $N_S$ and $N_T$ nodes, respectively, the problem of GM consists in finding the optimal correspondence $(\pi)$ between source and target nodes, such that the sum of the node and edge compatibility is maximized.

$$\begin{aligned} &\pi^* = \arg\max_{\pi} \pi^T \mathbf{W} \pi, && \pi \in \{0,1\}^{N_S \times N_T} \\ &\Pi = \{\pi \mid \pi \in \{0,1\}^{N_S \times N_T}, \pi \mathbf{1}_{N_T} \leq \mathbf{1}_{N_S}, \pi^T \mathbf{1}_{N_S} = \mathbf{1}_{N_T}\} \end{aligned} \tag{IV.1}$$

where $\pi \in \Pi$ is constrained to be a one-to-one mapping, and the symmetrical matrix $\mathbf{W} \in \mathbb{R}^{N_S N_T \times N_S N_T}$ encodes the similarity between nodes along its diagonal elements, whereas the edges similarity is encoded in the off-diagonal ones. Due to the combinatorial nature, globally optimizing GM is NP-hard. Approaches to this large scale problem focus on finding an inexact matching between graphs with weighted attributes on nodes and edges. Therefore, the main body of research in GM has focused on devising more accurate algorithms to solve it approximately. A relaxation of the permutation constraints (Eq. IV.1) is necessary to find an approximation to the problem. However, this is challenging because the objective function is in general non-convex and thus existing methods are prone to local optima.

Leordeanu et Hebert (2005) approximated Eq. IV.1 by relaxing $\pi$ to be of unit length. The optimal $\pi$ can then be efficiently computed as the leading eigen-vector of $\mathbf{W}$. This spectral matching (SM) method has low complexity due to the relaxation during optimization step and is robust to noise and outliers. Cour et al.

(2007) extended SM and modified the original quadratic score, while incorporating an affine constraint during optimization, hence finding better approximations. However, these spectral techniques can only match few tens of nodes.

Another approach useful for interpreting and solving GM problems are probabilistic frameworks. Cho et al. (2010) casted graph matching into a node ranking and selection problem on an association graph whose nodes represent candidate correspondences between the graphs to match. For this ranking, they introduced an affinity-preserving and reweighted random walks. The former derives in a ranking based on its quasi-stationary distribution, while the later obtains the solution by simulating random walks with re-weighting jumps enforcing matching constraints. This method is more robust to noise than SM but also slower.

The performance of GM methods in real applications is often limited by the initial quality of the graphs to match. To resolve this issue, Cho et Lee (2012) proposed a progressive framework which combines graph matching and probabilistic graph progression. First, the best matching between current active graphs is found. Based on this the graph progression reestimates in a Bayesian manner the most plausible target graphs and their similarity matrix to boost the score in the next matching. The method handles realistic large graphs, and is robust to appearance variation as well as outliers.

A novel interpretation of the large pairwise affinity matrix ($\mathbf{W}$) was proposed by Zhou et De la Torre (2015). Here, the topology of each graph and the edges pairwise affinity are locally encoded with smaller matrices that are factorized from $\mathbf{W}$. This avoids the costly computation of $\mathbf{W}$, allowing better optimization strategies and improving the matching results. In addition, factorization makes it possible to incorporate geometric transformations constraints (rigid and non-rigid) during the matching.

The methods reviewed in this section do not need any initial estimates. However, all these methods use the nodes' descriptors (Lowe, 2004; Bay et al., 2006) to define the graphs' similarity. Given that the considered vascular images lack distinctive local appearance information, these methods can not be directly used for our targeted application.

## IV.2 Graph matching for vessels registration

To overcome the lack of discriminative local appearance features in the considered vessel images, the GM methods presented in this section use other vascular image properties or approaches to register vessels. In this thesis, the GM methods are classified in three categories accordingly to the approach used to reduce the matching complexity. The first class uses initialization, the second uses the topological and geometrical graph properties and the last one simultaneously searches for correspondences and updates the transformation. The following GM methods are described and their compatibility with the targeted application is reviewed.

In the first class, the problem complexity is reduced through initialization of the matching. Motivated by liver applications, Charnoz et al. (2005) iteratively matched edges and nodes starting from an initial alignment of the tree root. The set of matching hypotheses generated is updated to keep matches that minimizes a cost function between pairs of nodes/edges. It requires explicit tree topology to accurately capture the underlying vasculature and was tested on mono-modal registration of high quality images. Moreover, the manual initialization is a burden during intra-operative procedures.

Nam et al. (2011) rigidly initialized the matching using the Viterbi algorithm to determine the vessels correspondences based on the similarity of edges directions. Then, an affine ICP-based registration refined the alignment of the vessels and the liver surface. This pre- and intra-operative (CT and 3D B-mode US) registration assumed small deformation. Obviously this affine transformation can not guarantee a correct recovery of non linear deformation, specially if this is large.

The second class of techniques relies on the geometrical and topological structure of the graphs, which are crucial properties shared across modalities. Graph matching have been formulated by considering compatibilities between edges or nodes, for example by comparing their Euclidean or geodesic distances (Deng et al., 2010; Smeets et al., 2010). These methods allow for a non-parametric formulation of the problem and are valid for slight pulmonary or retinal vessels deformation. However, they are very sensitive to the small length changes of the inter-nodal distances and require local appearance information.

Robben et al. (2013) also used pairwise distances and bifurcations descriptors for labeling Circle of Willis (CoW) vessels from different subjects. They matched the graph with a probabilistic attributed graph atlas which was generated from an annotated training set of graphs. The matching is done in a Maximum A Posteriori way and is formulated as a quadratic binary programming problem. This approach can handle non treelike vasculature and large topological differences. However, the liver vasculature considered in our work has much more bifurcations and matching ambiguity than the CoW. Thus, it is not guaranteed that a relatively small training set would be enough to handle it.

To overcome the lack of local appearance, Pinheiro et al. (2017) incorporated a path descriptor of connected nodes to efficiently match large graphs. They proposed a Monte Carlo tree search which balances the exploration of new possible matches and extends existing matches. Its efficiency relies in the path descriptor and an implicit transformation model that assume a rigid transformation with small nonlinear deformation. Thus, this method is not suitable for large deformations.

Also incorporating non local features, Moriconi et al. (2018) used the over-connected distances between the edges points which are around nodes within a neighborhood of a given radius. These over-connected distances and related node-attributes were used as extra graph features and matched with several of the GM methods described in Section IV.1. These added features compensate for topological inaccuracies or deformation of branches. However, robustness to large deformation is not guaranteed since nothing can ensure that the established correspondences are physically coherent with the elasticity of the organ.

All the methods that use geodesic distance constraints, including the methods presented by Moriconi et al. (2018); Pinheiro et al. (2017) rely on connectivity, thus they are unable to match disconnected graphs.

In the third class, the methods alternate between the correspondences search and the transformation update. Assuming a known initialization, Serradell et al. (2011) used an a priori parametric model of the transformation in a Kalman filter-like approach to progressively add matches and fit the deformation. This rapidly reduced the set of matched hypotheses, making the search complexity manageable. However, the required model is difficult to generalize to arbitrary deformations.

Following a similar approach that progressively reduces the number of potential correspondences but does not require an a priori parametric deformation model. Serradell et al. (2015) used a Gaussian Process Regression (GPR) deformation model to determine whether a new pair of correspondences is compatible with the current set of matching hypotheses. This method iteratively generates hypotheses while the search space is refined. The search space defines the most likely correspondences to explore at every step, without relying on local similarity. On several examples and without initialization, this method handled topological differences and deformation. Nonetheless, the GPR mapping can not handle large non-linear deformations and thus it may lead to incomplete solutions. Moreover, the matching time with large graphs does not satisfy intra-operative constraints.

To have a more discriminative deformation model without a prohibitive computational cost at each iteration, Pinheiro et Kybic (2018) recently proposed to use a B-spline deformation model which is updated incrementally using a Kalman filter. While this process saves time, B-splines are not able to properly describe elastic properties of the organs.

From the GM state-of-the-art presented, the method developed by Serradell et al. (2015) is not far to comply with intra-operative registration constraints. Thus, this method is described in Section IV.3 and experiments with hepatic data are presented in Section IV.5.

## IV.3 Gaussian process graph matching (GPR)

Serradell et al. (2015) presented a robust graph matching algorithm (GPR) that relies on Gaussian process regression (GPR) which is a nonparametric kernel-based probabilistic model used to compute a smooth geometric mapping. GPR priors embody beliefs about typical properties of the shape and the kernel $k(x, x')$ specifies the correlation of two function values corresponding to two different inputs $x$ and $x'$ (Rasmussen et Williams (2006)). The method does not require a manual initialization and handles partial matching and topological differences.

The GPR graph matching algorithm is presented in Alg. 1. It matches a source graph $\mathcal{G}^S = (\vec{X}^S, \vec{E}^S)$ to a target graph $\mathcal{G}^T = (\vec{X}^T, \vec{E}^T)$. Where $\vec{X}^S = \{\mathbf{s}_n \in \mathbb{R}^D,\ n = 1...N_S\}$ and $\vec{X}^T = \{\mathbf{t}_n \in \mathbb{R}^D,\ n = 1...N_T\}$ are the sets of source and target nodes (tree bifurcations that are points in $\mathbb{R}^D$, assuming $D \in \{2, 3\}$). Similarly, $\vec{E}^S = \{\mathbf{se}_m,\ m = 1...M_S\}$ and $\vec{E}^T = \{\mathbf{te}_m,\ m = 1...M_T\}$ are the sets of source and target edges.

The algorithm 1 recursively constructs a set of hypotheses, where each hypothesis $\pi_t$ is a set of $n_c$ source and target bifurcation matching pairs $(\mathbf{s}_i \leftrightarrow \mathbf{t}_j)$, starting with a random hypothesis (line 1). Using these correspondences, the GPR estimates the mean $m_{\pi_t}$ location with a covariance $\sigma^2_{\pi_t}$ of $\mathbf{s}_i$ that corresponds to $\mathbf{t}_j$ ; this operation is performed by procedure *ComputeMapping* (line 3) of Alg. 1; where

$$\begin{aligned} m_{\pi_t}(\mathbf{s}_i) &= \mathbf{k}^t C_{\pi_t}^{-1} \vec{X}^T_{\pi_t} \\ \sigma^2_{\pi_t}(\mathbf{s}_i) &= k(\mathbf{s}_i, \mathbf{s}_i) + \beta^{-1} + \mathbf{k}^t C_{\pi_t}^{-1} \mathbf{k} \end{aligned} \tag{IV.2}$$

with $k$ as kernel function, $\beta^{-1}$ the measurement of noise variance, $C_{\pi_t}$ the $n_c \times n_c$ symmetric matrix with elements $C_{m,n} = k(\mathbf{s}_m, \mathbf{s}_n) + \beta^{-1}\delta_{m,n}$, $\mathbf{k}$ is the vector $[k(\mathbf{s}_l, \mathbf{s}), ..., k(\mathbf{s}_{n_c}, \mathbf{s})]$, and $\vec{X}^T_{\pi_t}$ is the $n_c \times D$ matrix $[\mathbf{t}_1, ..., \mathbf{t}_{n_c}]^t$.

The summation of a squared exponential, a constant and linear term

$$k(\mathbf{s}_m, \mathbf{s}_n) = \theta_0 + \theta_1 \langle \mathbf{s}_m, \mathbf{s}_n \rangle + \theta_2 \exp\{-\frac{\theta_3}{2} ||\mathbf{s}_m - \mathbf{s}_n||^2\} \tag{IV.3}$$

is used as kernel with the $\mathbf{\Theta} = \{\theta_0, \theta_1, \theta_2, \theta_3\}$ GPR hyperparameters (Rasmussen et Williams, 2006).

To find the next matching candidates (line 4) the Mahalanobis distance

$$M^2 = (m_{\pi_t}(\mathbf{s}_i) - \mathbf{t}_j)'(\sigma^2_{\pi_t}(\mathbf{s}_i))^{-1}(m_{\pi_t}(\mathbf{s}_i) - \mathbf{t}_j) \tag{IV.4}$$

is used. Specifically in line 17, the bounded region candidates $(\mathcal{B}_i)$ are defined by the Mahalanobis $(M_{TH})$ and euclidean $(E_{TH})$ distance thresholds, where the current hypothesis $(\pi_t)$ defines the free source and target bifurcations sets as $\vec{X}^{SF} = \{\mathbf{s}_n \colon \vec{X}^S \notin \pi_t\}$ and $\vec{X}^{TF} = \{\mathbf{t}_n \colon \vec{X}^T \notin \pi_t\}$, respectively. Followed by the potential candidates $(\mathcal{P}_i)$ which are the bifurcations for whose target and source geodesic distances are proportionally ($G_{TH}$) similar, where $\mathbf{G}_{t_j} = [g_1, ..., g_{n_c}]$ are the target geodesic distances from the already established correspondences ($\pi_t$) to a new match $\mathbf{t}_j$ and similarly $\mathbf{G}_{s_i}$ for the source geodesic distances. Then, the matching candidates $\mathbf{P}$ found are the free bifurcations $\vec{X}^{SF}$ with the lowest number of potential candidates.

The algorithm continues (line 5) with the computation of the current hypothesis's number of *inliers*. Given the assignment distance cost matrix $C \in \mathbb{R}^{M_S \times M_T}$ built from the euclidean distance between the source and target edge points as

$$C(i,j) = \begin{cases} |m_\pi(\mathbf{se}_j) - \mathbf{te}_j|, & \text{if } |m_\pi(\mathbf{se}_j) - \mathbf{te}_j| < \beta^{-1/2} \\ \infty, & \text{otherwise.} \end{cases} \tag{IV.5}$$

The quality score is the number of matches of $C$ found with the Hungarian algorithm assignment ($H$) (Burkard et al., 2009)

$$S_\pi = |H(C)|. \tag{IV.6}$$

In the nested loops the hypotheses are generated. First, every free bifurcation in the random permutation of the matching candidates ($\mathbf{P}$) is explored. Then, every target candidate ($\mathbf{t}_{j^*}$) with its associated free source bifurcation from the random permutation of $\mathcal{P}_{i^*}$ creates a new hypothesis ($\pi_{t+1}$). Here, the number of target candidates used to create new hypotheses is limited by the number of outliers threshold ($O_{TH}$). The new hypothesis is used to recursively call the matching method until no more matches are found. Finally, when the recursion is completed, the best quality score hypothesis is selected from all the explored ones.

### IV.3.1 Fine Gaussian process graph matching (fineGPR)

Once the coarse bifurcation matching is completed, the best hypothesis ($\pi^*$) is used to initialize an iterative fine-matching step which matches the target ($\vec{E}^T$) and source ($\vec{E}^S$) edge points using the Hungarian algorithm assignment. The matched edges are filtered with geodesic and euclidean distance constraints. These filtered points are part of the paths that connect bifurcations and are used to recompute the GPR priors. Then, the inliers quality metric is computed and the procedure iterates until the metric does not improves.

The GPR matching does not requires an initial pose estimation and it does not rely on local appearance nor on global distance matrices. This method is robust to graphs topological changes and even to variations in the distances between nodes. However, the method can not properly match the considered vessel graphs. The first issue is that the matching time is very high, due to the large number of noisy nodes and its correspondence ambiguity. The Section IV.4 presents a faster version of the GPR matching to comply with **intra-operative timing constraints.** The second

**Algorithm 1** Recursive GPR graph matching $\mathcal{G}^S, \mathcal{G}^T$

```
$\pi_0 \leftarrow \{\mathbf{s}_{i_1} \leftrightarrow \mathbf{t}_{j_1}$ ,..., $\mathbf{s}_{i_D} \leftrightarrow \mathbf{t}_{j_D}\}$ ▷ Random initialization of the first hypothesis
function recursiveGraphMatchingGPR($\pi_t$)
    $\{m_{\pi_t}, \sigma^2_{\pi_t}\}$ = ComputeMapping($\mathcal{G}^S, \mathcal{G}^T, \mathbf{\Theta}, \pi_t$)
    $\mathbf{P}$ = FindCandidates($m_{\pi_t}, \sigma^2_{\pi_t}$)
    $S_{\pi_t}$ = QualityScore($m_{\pi_t}, \beta$)
    if $|\mathbf{P}| \neq 0$ then
        for $\mathcal{P}_{i^*}$ in RandomPermutation($\mathbf{P}$) do
            $n = 0$
            for $\mathbf{t}_{j^*}$ in RandomPermutation($\mathcal{P}_{i^*}$) do
                if $n > O_{TH}$ then
                    break
                $\pi_{t+1} \leftarrow \pi_t \cup \{\mathbf{s}_{i^*} \leftrightarrow \mathbf{t}_{j^*}\}$; $n = n + 1$
                RecursiveGraphMatchingGPR($\pi_{t+1}$)
$\pi^* = \arg\max \{S_{\pi_0}, ..., S_{\pi_T}\}$

function FindCandidates($m_{\pi_t}, \sigma^2_{\pi_t}$)
    for $\mathbf{s}_i$ in $\vec{X}^{SF}$ do
        $\mathcal{B}_i = \{\forall\ \mathbf{t}_j \in \vec{X}^{TF}: \mid M^2(m_{\pi_t}(\mathbf{s}_i),\ \mathbf{t}_j) < M_{TH} \vee |m_{\pi_t}(\mathbf{s}_i) - \mathbf{t}_j| < E_{TH}\}$
        $\mathcal{P}_i = \{\forall\ \mathbf{t}_j \in \mathcal{B}_i: abs(\mathbf{G}_{t_j} - \mathbf{G}_{s_i}) < (G_{TH} \cdot \mathbf{G}_{s_i})\}$
    $\mathbf{P} = \arg\min_i\{|\mathcal{P}_i|\}$ for $|\mathcal{P}_i| \neq 0$
```

issue is that the matching result is incomplete, specially the method is not able to retrieve corresponding branches that are largely deformed. A brute force approach to overcome large deformations would be to increase the Mahalanobis threshold ($M_{TH}$) and thus the search region. However, this highly increase the matching time and does not guarantee that the obtained solution is physically plausible. A biomechanical based solution to match largely deformed branches within intra-operative timing constraints is described in Chapter V.

## IV.4 Improved Gaussian process graph matching (iGPR)

Aiming to reduce the matching time, three improvements over the original GPR (Serradell et al., 2015) method compose the improved Gaussian process graph matching (iGPR). The first two improvements consist in using the bifurcations radii and tree topology as soft features to avoid the exploration of noisy or incorrect ambiguous bifurcations correspondences. The original GPR matching was designed for very generic applications where these features might not be available.

**Covariance search space in GPR and iGPR**

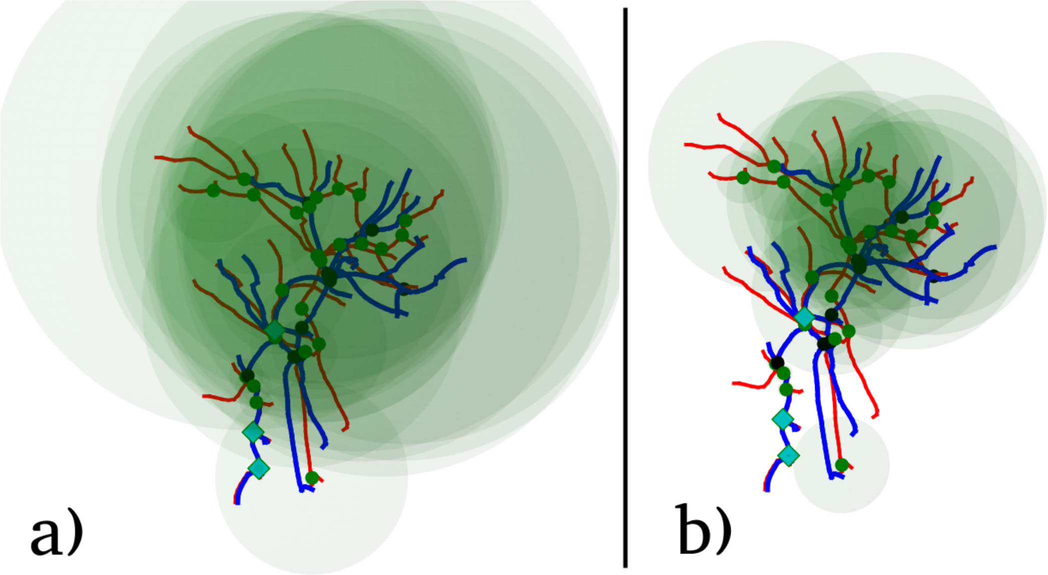

**Figure IV.1:** The target (in blue) and model (in red) graphs matched with 3 bifurcations (in cyan diamonds) at the beginning of the exploration. a) The original GPR (Serradell et al., 2015) uses the covariance Mahalanobis threshold ($M_{TH}$) to compute the bounded region (green transparent spheres). b) The iGPR halves the $M_{TH}$ to reduce the unnecessary large search space.

However, these features are present in the considered data as shown in Section III.3. The third improvement reduces the search space at the beginning of the matching when the GPR covariance is highly unreliable.

**Half first covariance constraint.** Looking at the behavior of GPR based matching, the covariance evaluated with a small number of matched bifurcations largely exceeds the motion that the organ can undergo during deformation, as shown in Figure IV.1.a. This leads to the exploration of many false hypotheses at the beginning of the matching process. To handle this issue, the threshold $M_{TH}$ used to define the bounded region (Eq. IV.4), is halved when the hypothesis to explore has less than 4 bifurcations matched, as shown in Figure IV.1.b.

**Radius constraint.** At every bifurcation the radius of each vessel is averaged over the section between the bifurcation and 20% of the length of the vessel. To assign the branch correspondences, the target ($r^T$) and source ($r^S$) averaged radii of each bifurcation are sorted. Theoretically, the radii should be similar. However, due to the image properties or preprocessing the radii obtained is inaccurate, especially with US modality. To take into account these inaccuracies, the bifurcations are considered for matching if they are below a relaxed threshold ($R_{TH}$):

$$\left|\frac{\min(r^T, r^S)}{\max(r^T, r^S)} - 1.0\right| < R_{TH}. \tag{IV.7}$$

**Topological constraint.** In the case where the target and model graphs have similar structures, topological properties of tree branching patterns of the trees can be used to discard erroneous matching hypotheses. Two topological characteristics are used: the *Horton-Strahler number* ($HS$) of a node and the *centrifugal order* of a segment. The centrifugal order ($CO$) of a segment denotes its geodesic distance to the root segment van Pelt et al. (1989), whereas the $HS$ of a node or a tree is a numerical measure of its branching complexity Devroye et Kruszewski (1995). This number is defined for leaf nodes as $HS_{leaf} = 0$ and for any parent node ($k$) with children nodes ($i$ and $j$) as $HS(k) = \max(HS(i), HS(j)) + \delta_{HS(i),HS(j)}$. The $HS$ of each graph is here normalized with respect to its maximum. Two thresholds $CO_{TH}$ and $HS_{TH}$ are specified to discard from the matching hypotheses trees which have highly different topological properties. Bifurcations are considered for matching if:

$$|CO^T - CO^S| < CO_{TH} \quad \text{and} \quad |HS^T - HS^S| < HS_{TH} \tag{IV.8}$$

These constraints were only used in a first initialization matching of the large noisy graphs from real data experiments in Sections IV.5.2, V.2.1 and V.4.2. This is crucial to reduce the space of possible combinations when the number of bifurcations is large. In this initialization matching, only 30 bifurcations with the highest $HS$ and big vessels mean radii are used. Even in the presence of noise, as long as the trees have a few similar main branches these constraints allow to drastically decrease the matching time in the considered data. The typical values used for the constraints thresholds are: $R_{TH} = 0.4$, $CO_{TH} = 4$ and $HS_{TH} = 0.6$. Once initialized, the complete set of bifurcations is used to find a second coarse match (iGPR$_{Full}$).

## IV.5 Evaluating the GPR and iGPR algorithms.

This section presents the case of registering intra-operative Cone Beam Computed Tomography (CBCT) images with preoperative computed tomography angiography (CTA) data. The fusion approach proposed is based on the matching of pre- and intra-operative vascular trees according to the GPR and iGPR methods and evaluated on both synthetic and real data. All the results and computation times were obtained with a regular desktop computer (4GHz eight-core, 16 GB RAM).

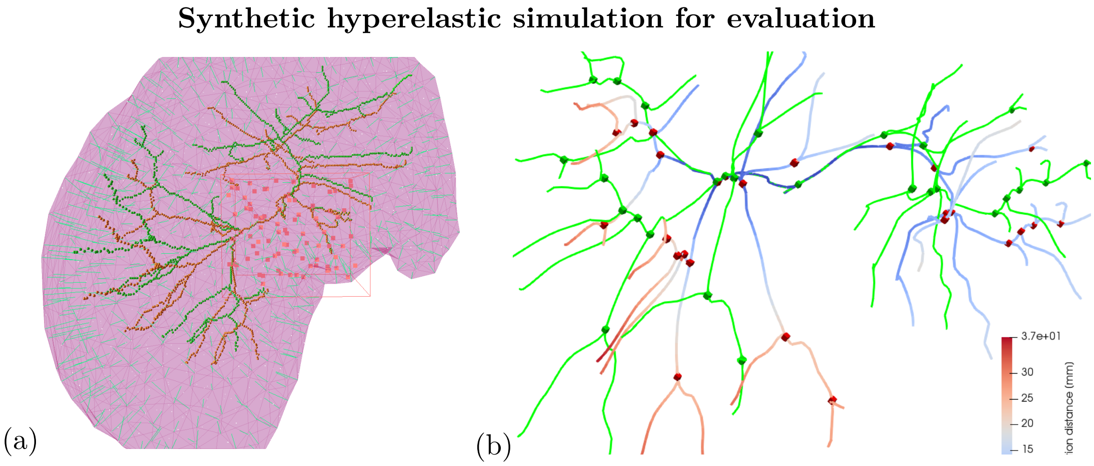
**Synthetic hyperelastic simulation for evaluation**

**Figure IV.2:** a) Hyperelastic FE simulation setup used to obtain the medium deformation for evaluation. b) The original graph (in green) and the synthetic deformation distance color mapped graph.

### IV.5.1 Experiments on synthetic data

First, simulated realistic deformations and vessels removal was done on the CT graphs to resemble CBCT. This ground truth data is used to evaluate and compare the matching methods described.

The liver FEM and portal vein tree used for validation are extracted from the IRCAD human dataset[1]. A StVenant Kirchhoff hyperelastic constitutive model is used to simulate realistic deformations of the liver model. Constant pressure is applied to the model to simulate a pneumoperitoneum. Dirichlet boundary conditions are set near the portal vein. Fig. IV.2.a illustrates the simulation setup. Three different levels of deformations were simulated, using the same pressure value (1.6 kPa) and varying Young modulii (15.0 kPa, 7.0 kPa and 3.5 kPa) leading to small, medium and large displacement fields. The medium deformation is shown in Fig. IV.2.b. Here, the original graph is in green and the deformed graph is color mapped with the deformation displacement. From this deformed CTA graph, leaf vessels were iteratively removed until only 60% remained, as a way to mimic the partial graph usually segmented from CBCT images.

The Fig. IV.3 shows coarse matching results of the model and target medium synthetic deformation level graphs which have 28 and 16 bifurcations, respectively. Here, the original GPR algorithm (in cyan) is compared against the iGPR (in blue) and the Half first covariance improvement shown (in purple). The GPR algorithm depends mainly on the Mahalanobis ($M_{TH}$), geodesic ($G_{TH}$), and the outlier tol-

---

[1] https://www.ircad.fr/research/3dircadb/

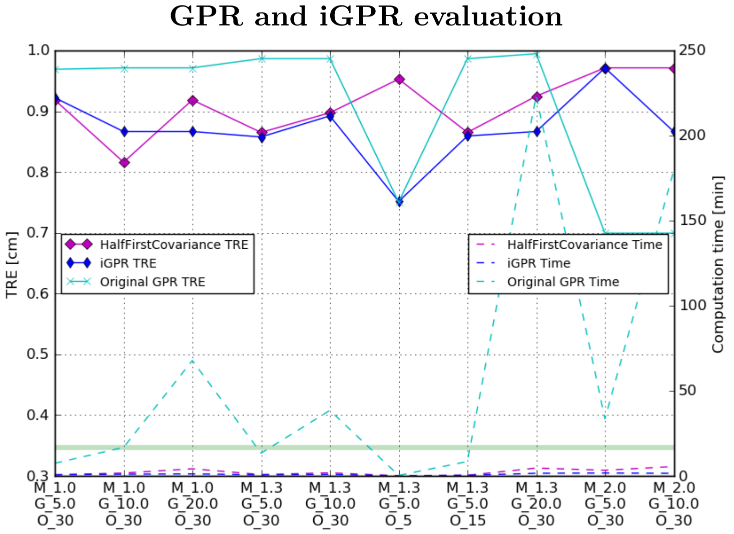

**Figure IV.3:** Comparison of original GPR (cyan), Half first covariance (purple) and iGPR (blue) matching methods on the medium synthetic deformation. The TRE are in solid lines whereas the times are in dashed lines. The proposed improvements (Half first covariance and iGPR) have similar TRE while being much faster than the original GPR matching(Serradell et al., 2015).

erance ($O_{TH}$) thresholds. Thus, the algorithms are evaluated with representative commonly used parameters (Serradell et al., 2015). The target registration error (TRE) is computed using every edge point in the original graph, including the 40% removed vessel branches. The green thick horizontal line marks the ground truth coarse matching TRE, it is computed using the ground truth bifurcation matches in the target and model graphs. Given that 40% target bifurcations were removed, coarse ground truth TRE using only bifurcations does not reach zero. The TRE of each method is plotted in solid lines whereas the matching time is indicated with dashed lines. The three methods have similar TRE results about 6 mm higher than the ground truth. However, the improved versions are up to 1000 times faster than the original one.

### IV.5.2 Experiments on real data

From the two porcine liver datasets (PA and PB), each real dataset has one CTA image acquired preoperatively in supine position and one CBCT image acquired after pneumoperitoneum on flank position (see Section III.3.4 for more details). These intra-operative conditions generated a large deformation. From each modality the portal vein is segmented and a graph is extracted as described in Chapter III. The portal veins graphs are matched to register the CTA data onto the CBCT.

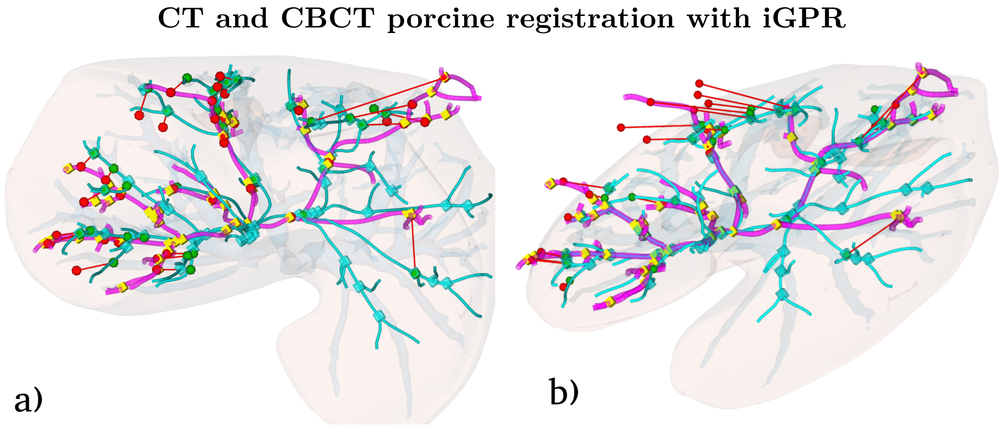

**Figure IV.4:** For the PA porcine dataset, the target CBCT (in pink) and source CTA (in cyan) portal vein graphs are rendered with tubular structures. The graph nodes (bifurcations) are shown as cubic markers (in yellow for the target, cyan for the source and green for the matched). The augmented hepatic vein, which was only visible in the CTA image, is in transparent blue behind the portal veins graphs. The 37 target evaluation landmarks (red spheres) and their corresponding connected source landmarks (green spheres) and the liver structures are rigidly aligned in a). These depict the large intra-operative non-linear deformation. The result of iGPR$_{Full}$ after fine matching (fineGPR) and the 27 registered landmarks with an error larger than 4 mm are shown in b). The middle target portal vessels, which are uncovered by the registered liver surface, show the GPR inability to extrapolate deformations.

Although the number of bifurcations (in Table III.2) is similar in both modalities, several false bifurcations are detected due to noise in the CBCT.

The matching is evaluated with reliable and unambiguous manually selected landmarks that are clearly visible in both modalities. These landmarks include inserted tumors, distinctive vessel points and bifurcations (3, 15 and 19 for PA, while 6, 5 and 11 for PB, respectively). The registration error (RE) is computed using all these evaluation landmarks, while the matching only uses the bifurcations. Therefore, the RE cannot reach zero in these experiments. Given that in some cases these landmarks can not be accurately selected we make a difference with respect to TRE where the simulation gives accurate and abundant ground truth correspondences for evaluation.

The Table IV.1 presents the registration results for each dataset. Given the large number of bifurcations in the real data, the first iGPR initialization matching uses only the 30 bifurcations with higher radii and $HS$, as described in Section IV.4. Using the matches obtained with this iGPR initialization, a rigid transformation is computed to quantify the RE and to depict the nonlinear deformation magnitude, as shown in Fig. IV.4.a. This iGPR initialization only required 2.1 minutes for matching, while the original GPR matching ran 24 hours and did not finish the exploration due to the large number of bifurcations and matching ambiguity.

Then, a second iGPR$_{Full}$ coarse matching was done starting with the iGPR initialization and using all the bifurcations. For PA, the RE with the iGPR$_{Full}$ matching is slightly worst than the rigid alignment because there are several missing matches which do not allow the regression to correctly recover the deformation. Even after the fineGPR matching the RE does not improve producing unrealistic deformation specially far from the matched vessels, as shown in the Fig. IV.4.b where the liver surface does not cover the target portal vein. For PB, the iGPR$_{Full}$ has a slight 2.70 mm TRE improvement compared to the rigid alignment, still the error is not ideal for intra-operative accurate applications.

**Table IV.1:** Matching results for the rigid iGPR initialization as deformation reference and iGPR$_{Full}$ that matches the complete set of bifurcations.

| Porcine dataset | Matching Method | Number of matches | RE [mm] $\mu \pm \sigma$(max) | time [min] |
|---|---|---|---|---|
| PA<br>37 landmarks | iGPR$_{Rigid}$ | 6 | 9.46±11.93 (65.3) | 2.1 |
| | iGPR$_{Full}$ | 15 | 12.51 ± 12.44 (42.2) | 11.6 |
| PB<br>22 landmarks | iGPR$_{Rigid}$ | 4 | 13.71±8.10 (33.6) | 0.42 |
| | iGPR$_{Full}$ | 9 | 11.01 ± 9.85 (33.7) | 1.2 |

## IV.6 Conclusion

The GPR matching algorithm (Serradell et al. (2015)) has two principal limitations: first, the data considered (specially the real vasculature) requires large matching time, which is inadequate for intra-operative conditions. As shown by the experiments, the iGPR initialization (proposed in the Section IV.4) reduces the matching time, however a high TRE remains.

The second limitation is that the GPR smooth geometrical mapping is not capable of finding correct matches when large nonlinear deformations occur. Moreover, the regression using few matches produces a large registration error and unrealistic deformation especially far from the matched structures. This limitation is undesirable for intra-operative applications and is addressed using a biomechanical model in Chapter V.

Chapter V

# Biomechanical graph matching

The original GPR matching (Serradell et al., 2015) is relatively generic and depending on the values of the hyperparameters it may theoretically adapt to large range of deformations. Nevertheless, the deformations which occur in soft tissues during surgical manipulations display a high level of non-linearity due to their complex characteristics. Typically, internal structures such as vessels introduce heterogeneity and anisotropy, these cannot properly be taken into account without a biomechanical model. The Section V.1 describes the parenchyma and the vascularized biomechanical liver models used by the biomechanics-based graph matching (BGM) and compliance matching methods, respectively.

The Section V.2 presents BGM which extends the GPR matching with the fast biomechanical model of soft tissue which increases the robustness and performance of matching since it is capable of handling large nonlinear deformations while preserving their physical nature. Experiments of synthetic and real data that compare the iGPR and the BGM are also presented.

To overcome the BGM large computation time and lack of robusteness on noisy datasets, the Section V.3 presents the VCGM and ACGM methods which use the efficient biomechanical vascularized liver model to compute the organ's transformation and the vessels bifurcations compliance. This allows to efficiently find the best graph matches with a novel compliance-based search. It also presents the adaptive rigid-to-soft approach used by the ACGM.

Finally, the Section V.4.2 compares all the biomechanical graph matching methods presented, which register synthetic datasets and CT preoperative data into intra-operative CT-CBCT and 3DUS. This shows that having a physically correct model allows to find large deformations and using an accurate hypotheses search space reduces the matching time.

## V.1 Fast biomechanical liver model

Two fast biomechanical liver model methods were used in the matching methods. The first one is a co-rotational linear model of the liver paranchyma used by BGM to compute the transformation of the pre-operative data given the actual hypothesis. The second is a composite efficient biomechanical vascularized model used by the VCGM and ACGM compliance graph matching methods. The purpose of this vascularized model, besides the pre-operative data deformation, is to compute the compliance which replaces the covariance from the original GPR matching algorithm.

### V.1.1 Parenchyma model

The biomechanical model used by BGM is based on the co-rotational formulation of linear elasticity (Nesme et al., 2005). Although this approach relies on a linear stress-strain relationship, it provides a good approximation of large deformations including rotations.

The parenchyma is modeled with linear P1 tetrahedral elements where for each element $p$, the local 12×12 stiffness matrix $\mathbf{K}_p$ is computed as

$$\mathbf{K}_p = \mathbf{R}_p(\mathbf{u}_p)^\top \left\{ \int_{V_p} \mathbf{B}_p^\top \mathbf{D}_p \mathbf{B}_p dV \right\} \mathbf{R}_p(\mathbf{u}_p) \tag{V.1}$$

where $\mathbf{B}_p$ and $\mathbf{D}_p$ are, respectively, the strain-displacement and stress-strain matrices which remain constant during the simulation, and $\mathbf{R}_p$ is a matrix composed of the element rotation matrix which depends on the actual displacement $\mathbf{u}_p$ of the parenchyma mesh nodes thus introducing a non-linearity into the formulation (Nesme et al., 2005). The FE mesh of liver composed of linear tetrahedra has been generated (Boltcheva et al., 2009) from a 3D mask segmented from the preoperative image. Moreover, it allows to specify a set of points located inside the mask which become nodes of the mesh.

A matching hypothesis $\pi$ is given by pairs of bifurcations $\mathbf{s}_i \leftrightarrow \mathbf{t}_j$. As the positions in set $\vec{X}^S$ defined in section IV.3 are known preoperatively, the mesh is generated so that each point from this set coincides with a node $n_i$ of the FE mesh. In this case, the deformation of the model is driven by the set of non-homogeneous Dirichlet conditions where for each matching pair, the displacement of node $n_i$ is prescribed as $\mathbf{u}_{n_i} = \mathbf{p}_i = \mathbf{t}_j - \mathbf{s}_i$.

The Dirichlet conditions are imposed via penalty method: physically, this method can be interpreted as adding a set of elastic linear springs which pull each node $n_i$ from its initial position $\mathbf{s}_i$ to the target position $\mathbf{t}_j$. Similarly, the deformation is computed as a dynamic process given by the system $\mathbf{M}\ddot{\mathbf{u}} + \mathbf{B}\dot{\mathbf{u}} + \mathbf{K}(\mathbf{u}) = \mathbf{p}$

where $\mathbf{M}$ is a mass matrix, $\mathbf{K}$ is the nonlinear co-rotational stiffness with contributions from elastic springs, $\mathbf{B}$ is a damping matrix approximated using Rayleigh stiffness $r_K$ and Rayleigh mass $r_M$ as $\mathbf{B} = r_M\mathbf{M} + r_K\mathbf{K}$ and $\mathbf{p}$ is a vector gathering the prescribed displacements given by the actual matching pairs (Plantefève et al., 2016). The system is integrated by implicit Euler method with single linearization per integration step with $r_K = r_M = 0.1$. The simulation is completed as soon as the simulation achieves the static equilibrium.

The model reconstructed from patient-specific anatomy is reliable for physics-based augmented reality (Plantefève et al., 2016). The proposed matching method is not limited to the chosen FE model which can be replaced by another elastic model, including non-linear ones (Marchesseau et al., 2017a).

The FE model is used in a *displacement-zero traction* scenario. In this case, no forces are applied to the model, however, the deformation is induced by non-homogeneous Dirichlet boundary conditions. In case of homogeneous isotropic model, the resulting deformation does not depend on the mechanical parameters which are usually not known accurately due to the patient-specific modeling (Wittek et al., 2009).

### V.1.2 Vascularized model

The biomechanical model is a composite FE approach which accounts for the mechanics of both of parenchyma and vessels (Peterlík et al., 2012b; Plantefève et al., 2016) is used to model vascularized tissue. Besides adding anisotropy to the transformation of the pre-operative data given the actual hypothesis, this vascularized model computes the compliance which is used in the VCGM and ACGM algorithms to define the matching search space.

The parenchyma is modeled with linear tetrahedral elements as done in Section V.1.1, where the stiffness matrix of each element is also defined by Eq. V.1. The vascular structures are modeled as trees composed of serially-linked Timoshenko beam elements, mimicking the biomechanics of hollow tubes parametrized with Young's modulus, diameter and wall thickness. The beam mechanics includes both positional and rotational degrees of freedom (DoF). Hence, each beam element $v$ is modeled with a 12×12 local stiffness matrix $\mathbf{K}_v$ which depends on the actual displacements and orientations of the beam nodes (Przemieniecki, 1985; Duriez et al., 2006).

Despite the identical size, the element matrices $\mathbf{K}_p$ and $\mathbf{K}_v$ have a completely different structure: the former describes mechanics of an element given by 4 nodes each determined by 3 positional DoFs, while the latter determines the behavior of element having two nodes, each equipped with 3 positional and 3 rotational DoFs. The coupling mechanism (Peterlík et al., 2012b) uses a mapping that defines a Jacobian matrix $\mathbf{J}_{v\rightarrow p}$ which is used to compute a composite stiffness matrix $\mathbf{K}_e$ as

$$\mathbf{K}_e = \mathbf{K}_p + \mathbf{J}_{v\to p}^{\top}\mathbf{K}_v\mathbf{J}_{v\to p}. \tag{V.2}$$

The generation of tetrahedral mesh of the parenchyma is the same as the one described in Section V.1.1, while the beam tree representing the vascular structure is extracted as described in Section III.2.

Given the biomechanical FE model represented by a global stiffness matrix $\mathbf{K}$ assembled from composite local matrices $\mathbf{K}_e$, the matching hypothesis $\pi$ determines non-homogeneous Dirichlet condition that drives the deformation model as done in Section V.1.1. Since the local stiffness matrices of parenchyma and vascular elements depend on the actual displacement vector $\mathbf{u}$, the problem is non-linear, and the final equilibrium must be computed iteratively. A damped Newton-Raphson method is used: in each iteration $k$, the update $\Delta\mathbf{u}^{(k+1)}$ of nodal positions is computed by solving a system of linear equations

$$\left[\tau\mathbf{I} + \hat{\mathbf{K}}_{\pi}(\mathbf{u}^{(k)})\right]\Delta\mathbf{u}^{(k+1)} = -\mathbf{g}_{\pi}(\mathbf{u}^{(k)}) \tag{V.3}$$

where $\hat{\mathbf{K}}_{\pi}$ is the global system matrix after imposition of non-homogeneous Dirichlet boundary conditions corresponding to the hypothesis $\pi$, $\tau$ is a damping parameter, $\mathbf{I}$ identity matrix having the identical size as $\hat{\mathbf{K}}$ and the vector $\mathbf{g}$ of the right side gathers the internal elastic forces and prescribed displacements given by the hypothesis $\pi$. The displacement vector is updated in each step of the method as $\mathbf{u}^{(k+1)} = \mathbf{u}^{(k)} + \Delta\mathbf{u}^{(k+1)}$, until the equilibrium displacement is obtained for hypothesis $\pi$ (Peterlík et al., 2018). Since the aim is to minimize the time needed for the computation of the transformation, preconditioning is used: In the first iteration of the Newton-Raphson method, the Eq. V.3 is solved with an algorithm based on the sparse Cholesky decomposition[1]. In the following iterations, preconditioned conjugate gradients are used to compute the update $\Delta\mathbf{u}$ employing the decomposition constructed in the first iteration.

Besides the elastic transformation, the FE model is employed to obtain the compliance in the *free source bifurcations* ($\vec{X}^{SF}$) which is used in both the VCGM and ACGM algorithms. According to the mathematical definition, compliance is defined as the inverse of the stiffness matrix. It is evaluated in an arbitrary node $n$ of the FE mesh where it is given by a 3×3 symmetric tensor $\mathbf{C}^n$ extracted from the global compliance matrix. Eigenvectors of the compliance tensor define the principal axes of an ellipsoid and the eigenvalues determine its scale along each axis. From the mechanical point of view, this ellipsoid characterizes the flexibility of $n$, i. e., it is proportional to the volume to which the node can be displaced under constant unit force applied to the node $n$ in an arbitrary direction. The source bifurcations coincide with a mesh node $i$ hence its compliance $\mathbf{C}_{\pi}^{i}$ corresponds to the block

---

[1] `https://www.pardiso-project.org/`

extracted from $\hat{\mathbf{K}}_\pi^{-1}$ at the position indexed by $i$. Since the proposed method is adapted to large deformations, it is necessary that the compliance $\mathbf{C}_\pi^i$ is computed using the stiffness matrix $\hat{\mathbf{K}}_\pi$ computed using the equilibrium displacement vector $\mathbf{u}_\pi$. Therefore, the elastic transformation corresponding to hypothesis $\pi$ is computed before the $\mathbf{C}_\pi^i$ is obtained for each *free source bifurcation*.

The compliance has been used in other applications to produce structures having desirable physical properties Martínez et al. (2015). Whereas, in Section V.3 the matching algorithms use the compliance to define an improved metric for the generation hypotheses.

## V.2 Biomechanics-based graph matching (BGM) and fine alignment

The bifurcations coarse matching using the parenchyma co-rotational model is described in Alg. 2. This BGM method is similar to the GPR matching described in Section IV.3, however it has two important differences:

- BGM replaces the mean from the original GPR matching with the parenchyma biomechanical model transformation (line 4). While the physically plausible FE transformation avoids the exploration of false hypotheses and finds more correct hypotheses, it is too computationally expensive to be employed from the beginning of the matching. On average, the time required to compute the FE transformation is 1000 times larger than the time required by the GPR.
- To overcome the computation time increase, instead of the random initialization, the FE-based matching is initialized with the result of iGPR (line 1), thus providing, within a feasible time, a correct but often incomplete set of matched bifurcations considering small or medium-sized deformations. Starting from this solution, the BGM generates a set of hypotheses recursively and is able to find the matches that were not discovered with the iGPR.

The FE model-based fine-alignment (fineBGM) is similar to fineGPR described in IV.3.1 but replaces the mean mapping by a nonrigid transformation using the liver biomechanical model. It also removes the matched graph points that are closer than the mean tetrahedral size of the FEM mesh.

### V.2.1 Comparing the iGPR and the BGM methods

This section registers intra-operative CBCT images with preoperative CTA data. The expected benefit is an improved visualization of the patient's tumor(s), vascular system and other internal structures of interest. CBCT is an imaging modality

**Algorithm 2** Recursive FEM matching (BGM) $\mathcal{G}^S, \mathcal{G}^T$

```
$\pi_{iGPR} \leftarrow \{\mathbf{s}_1 \leftrightarrow \mathbf{t}_1 ,..., \mathbf{s}_k \leftrightarrow \mathbf{t}_k\}$        ▷ iGPR matching initialization
function recursiveGraphMatchingBGM($\pi_t$)
    $\sigma^2_{\pi_t}$ = ComputeMapping($\pi_t, \mathcal{G}^S, \mathcal{G}^T, \Theta$)
    $\mathcal{T}_{\pi_t}$ = simulationFEM($\pi_t, \mathcal{G}^S, \mathcal{G}^T$)
    $\mathbf{P}$ = FindCandidates($\mathcal{T}_{\pi_t}, \sigma^2_{\pi_t}$)
    $S_{\pi_t}$ = QualityScore($\mathcal{T}_{\pi_t}$)
    if $|\mathbf{P}| \neq 0$ then
        for $\mathcal{P}_{i^*}$ in RandomPermutation($\mathbf{P}$) do
            $n = 0$
            for $\mathbf{t}_{j^*}$ in RandomPermutation($\mathcal{P}_{i^*}$) do
                if $n > O_{TH}$ then
                    break
                $\pi_{t+1} \leftarrow \pi_t \cup \{\mathbf{s}_{i^*} \leftrightarrow \mathbf{t}_{j^*}\}$; $n = n + 1$
                RecursiveGraphMatchingBGM($\pi_{t+1}$)
$\pi^* = \arg\max \{S_{\pi_0}, ..., S_{\pi_T}\}$

function FindCandidates($\mathcal{T}_{\pi_t}, \sigma^2_{\pi_t}$)
    for $\mathbf{s}_i$ in $\vec{X}^{SF}$ do
        $\mathcal{B}_i = \{\forall\ \mathbf{t}_j \in \vec{X}^{TF} :\ |\ M^2(\mathcal{T}_{\pi_t}(\mathbf{s}_i),\ \mathbf{t}_j) < M_{TH} \vee |\mathcal{T}_{\pi_t}(\mathbf{s}_i) - \mathbf{t}_j| < E_{TH}\}$
        $\mathcal{P}_i = \{\forall\ \mathbf{t}_j \in \mathcal{B}_i : abs(\mathbf{G}_{t_j} - \mathbf{G}_{s_i}) < (G_{TH} \cdot \mathbf{G}_{s_i})\}$
    $\mathbf{P} = \arg\min_i\{|\mathcal{P}_i|\}$ for $|\mathcal{P}_i| \neq 0$
```

that is more available in the operating room than CTA or MRI. However, CBCT cannot image certain lesions nor complete anatomy. These deficiencies are compensated if preoperative data augment the intra-operative image. The fusion approach proposed is based on the registration of pre- and intra-operative vascular trees using the iGPR and the BGM matching methods and evaluated on both synthetic and real data. All the results and computation times were obtained with a regular desktop computer (4GHz eight-core, 16 GB RAM).

### Experiments on synthetic data

Using the three synthetic deformations with 40% random branches removed (described in Section IV.5.1) the efficiency of the BGM method for medium and large deformations is proved in these experiments. It is important to note that the FEM model used for matching is linear which makes the computation faster and uses a 1.5 kPa Young Modulus which is different from the ground truth simulations. The TRE computed using every edge point in the original graph is used to measure the coarse matching accuracy. A second metric used is the convex hull volume

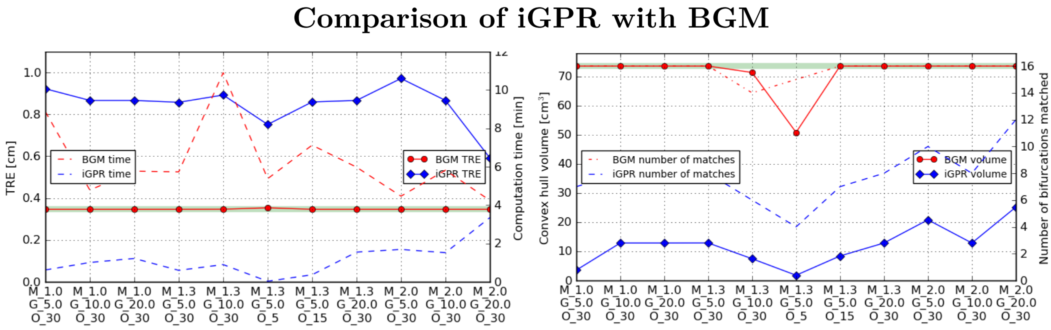

**(a)** **(b)**

**Figure V.1:** Accuracy and search space using different Mahalanobis (M), Geodesic (G) and Outliers (O) thresholds. In a) The TRE is plotted in solid lines. The iGPR (in blue) although is fast it is far from the ground truth (green thick horizontal line) and has high variability on the parameters used. The BGM TRE (in red) converges to the coarse TRE ground truth. In b) Similarly, the BGM convex hull volume and its number of bifurcations matches mostly converge to the ground truth values.

of the matched bifurcations. The convex hull volume gives a better idea of the global matching; a bigger volume ensures that the computed deformation is valid on a larger domain. Fig. V.1.a shows the TRE of the iGPR and the BGM on the commonly used parameters for the medium deformation transformation. As can be seen on the figure, the results of the iGPR step is dependent on the parameters whereas the results of the BGM are more accurate (4.2 mm against 12.2 mm) and limitedly dependent on the parameters used in the first iGPR step. Times required by the two processes are shown in the graph (time scale is on the right of the figure). In addition, much more bifurcations are matched with BGM and the convex hull volume of the set of matched bifurcations (Fig. V.1.b) is larger for the BGM whereas the iGPR method tends to provide only incomplete solution sets which are in fact only a partial graphs match. This is an important strength of the BGM algorithm. Note that large deformation matchings give similar results, summarized in Fig. V.3.

The Fig. V.2 compares TRE and timing of the fineGPR and the fineBGM matching methods on the medium deformation. Here again, the TRE is noticeably smaller with the fineBGM matching and the results are largely independent of the parameters. Note that fineGPR has small computation times because it uses the iGPR matching.

The Fig. V.3 summarizes the results on the three synthetic deformations. It shows a significant TRE improvement and less sensitiveness to parameters of the fineBGM compared to the fineGPR method. These results are specially important in the medium and large deformations. Still the fineBGM keeps computation times

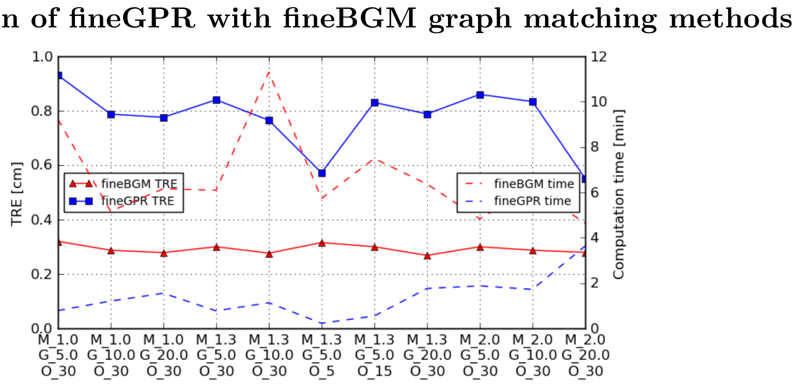

**Figure V.2:** The TRE is plotted in solid lines. The fineGPR (in blue) is faster but has bigger TRE (8 mm) and has high variance depending on the parameters used. The fineBGM TRE (in red) only has 3 mm error with small dependence on the parameters.

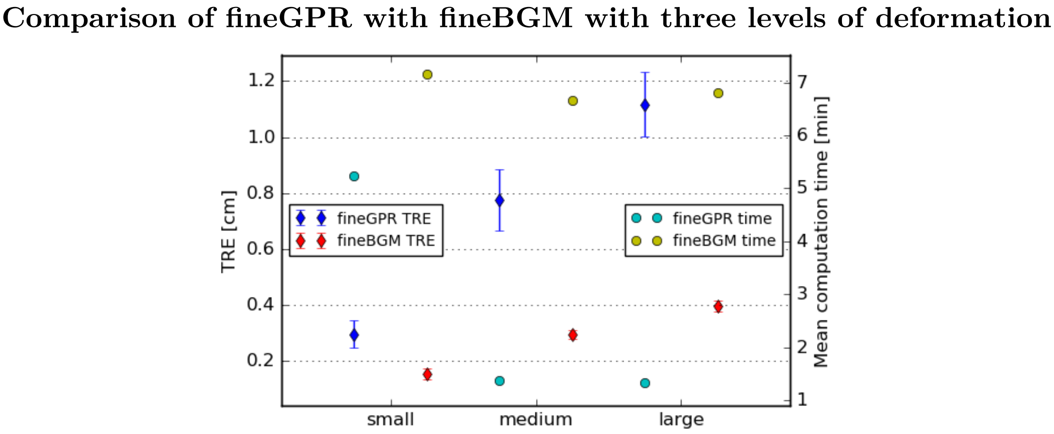

**Figure V.3:** The fineGPR is faster but has bigger TRE and high variance specially in the medium and large deformations. The TRE and dependence on the parameters in the fineBGM is small and it has an acceptable computation time increase.

within an acceptable intraoperative tolerance.

### Experiments on real data

For the first porcine dataset (PA), the Fig. V.4 shows the registration of the two vessel trees after a rigid registration (a) and the fineBGM registration (b). In the CT image 60 bifurcations (green cubes) are extracted while 47 (pink cubes) in CBCT. In total there are 20 correct matched bifurcations (purple cubes). The two trees are globally well registered except a vessel (indicated with an arrow in Fig. V.4.b) which is not transformed well because some bifurcations are missing in the target segmentation. Despite the differences between the trees, the superposition of the

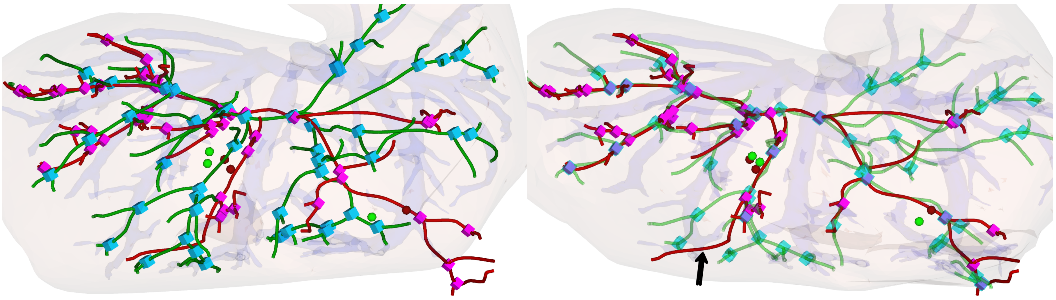

**BGM registration of CBCT and CTA from PA dataset**

**(a)** **(b)**

**Figure V.4:** The target CBCT and model CT graphs plotted, respectively, in red and green. Similarly the bifurcations are shown with cubes and three inserted landmarks centroids with spheres. The augmented hepatic vein shown in transparent blue. The model is rigidly aligned (a) to get an idea of the deformation. The fineBGM matching (b) shows matched bifurcations with purple cubes.

inserted landmarks is very good. The TRE is computed using reliable and unambiguous manually selected landmarks, as described in IV.5.2. The BGM method has a TRE of 5.38 mm. While only using iGPR matching has a TRE of 12.51 mm.

The computation time was 2.1, 39.3 and 0.5 minutes for the iGPR, the BGM and fineBGM, respectively. The matching is implemented in single thread and could be parallelized if the explored hypotheses are tracked in shared memory.

The result of the second porcine dataset (PB) is shown in Fig. V.5. The acquisition and deformation conditions were similar to the previous experiment. But this CBCT image is much noisier and only few vessels are visible and segmented. The target CBCT graph has 36 bifurcations but several false bifurcations (non matched pink cubes in Fig. V.5.b) are due to noise. Given that the vein is partially visible in CBCT, only the corresponding partial model CT graph with 39 bifurcations was used for matching. The matching is evaluated using 22 reliable landmarks, resulting in 7.61±7.34 mm TRE. The time needed for the iGPR is 0.42 minutes plus 55.6 minutes for the BGM. Finally, the CBCT view augmented with the CT vessel tree is showed in Fig. V.5.c.

The proposed biomechanics-based graph matching (BGM) outperforms existing state-of-the-art method (GPR) both in terms of accuracy and by its ability to handle large deformations. Since the matching time is directly linked to the number of vascular trees bifurcations, the surgeon could adjust automatic segmentation parameters that result in fewer bifurcations so the matching can be completed within intra-operative timing constraints. The method relies on the definition of several parameters. Some of them related to the biomechanichal model, while others have geometrical nature. At this stage the method is more sensitive to the geometri-

**BGM augmented CBCT from PB dataset**

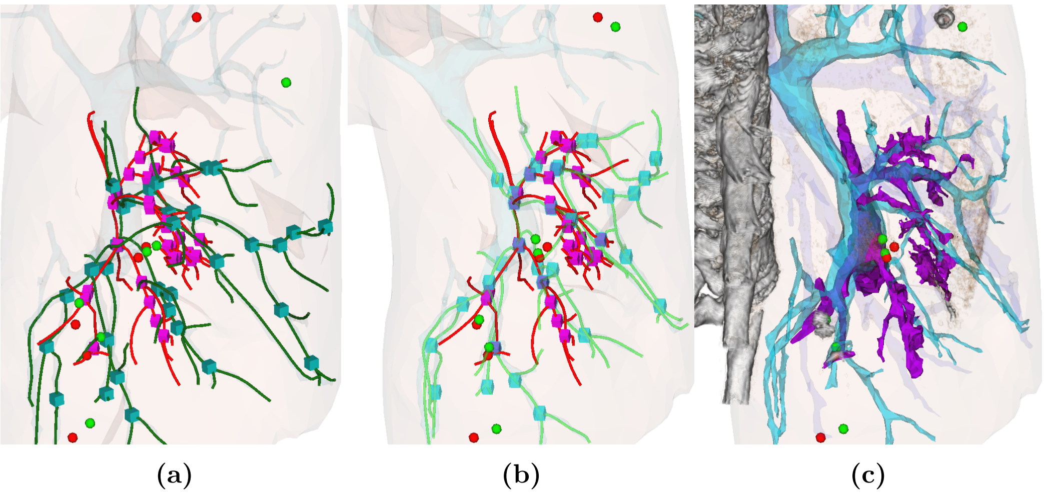

**Figure V.5:** The target and model graphs plotted, respectively, in red and green. Similarly the bifurcations are shown with cubes and six inserted landmarks centroids with spheres. The model is rigidly aligned (a). The fineBGM matching (b) shows matched bifurcations with purple cubes. An augmented view with the target and model portal vein in purple and blue respectively (c).

cal parameters, than the biomechanical ones. So some tunning when using real data still remains necessary for optimal results. Chapter V.3 presents a method that matches noiser graphs with more bifurcations within intra-operative timing constraints reducing the parameters and data quality dependence.

## V.3 Compliance Graph Matching

The biomechanical graph matching method (BGM) allowed to recover additional matches compatible with the elasticity of the organ even when large elastic deformations were considered. However, it was not robust to noise, only matched limited size graphs and the computation time was still above intra-operative constraints.

Several contributions with respect to BGM are presented in this section: i) the use of a more advanced biomechanical model to handle heterogeneities and anisotropy due to the vascularization, which was described in Section V.1.2; ii) the definition of a better metric for generating improved graph-matching hypotheses, based on the notion of compliance, the inverse of the stiffness, which is presented in Section V.3.1. iii) the generation of matching hypotheses using an adaptive search region, with the objective to further reduce computation time by predicting first the most plausible matching hypotheses, which is presented in Section V.3.2. These

**Covariance and compliance bounded region comparison**

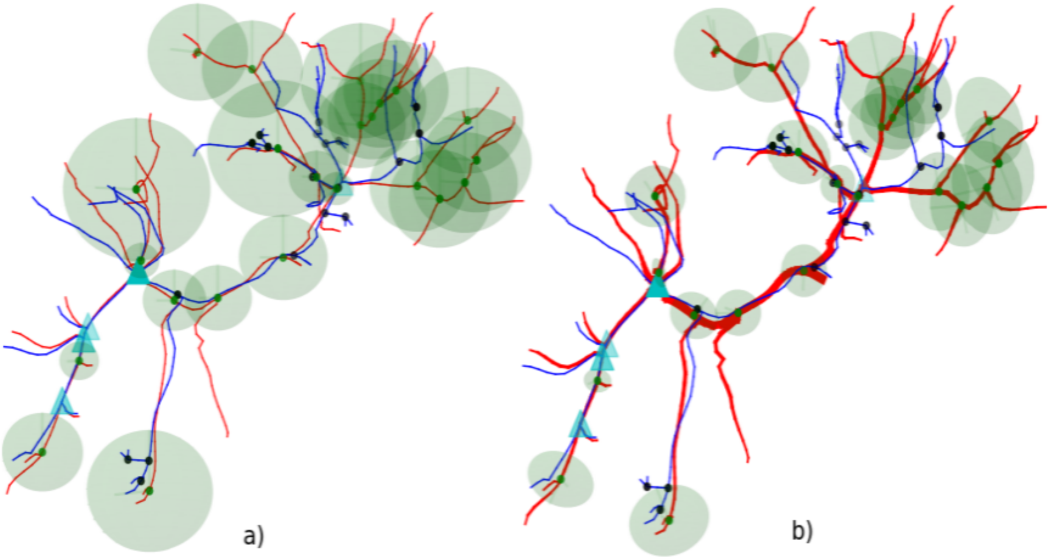

**Figure V.6:** Using the initially matched bifurcations (triangles), the bounded regions (spheres) are computed in the free bifurcations (green dots) of the source graph (in red). The free bifurcations (black dots) of the target graph (in blue) inside the bounded regions define the next matching candidates. The bounded regions are defined (a) in BGM with the GPR covariance and (b) in VCGM with the compliance of the varying radii vessels. In the later case, the stiff thick vessels have smaller compliance. This, along with the tensors shape and orientation reduce the matching search space.

contributions improve both the quality and computation time of the matching as shown in Section V.4, which presents a series of results on both synthetic and real data, including a sensitivity analysis highlighting its robustness and genericity.

## V.3.1 Vessels Compliance Graph Matching (VCGM)

BGM uses the GPR covariance to define the hypotheses search space and is able to find correct bifurcation matches even when large nonlinear deformations occur. However, the covariance produces large bounded regions for new correspondence search, shown in Fig. V.6.a, and large computation time. This makes the algorithm incompatible with intra-operative deployment. To overcome this crucial limitation, the first improvement proposed is VCGM which is described in Algorithm 3. Similarly to BGM, the matching is initialized with an incomplete hypothesis ($\pi_{iGPR}$) and then generates a set of hypotheses recursively.

VCGM's contribution starts by using $\pi_t$ with the vascularized FE simulation to compute the transformation ($\mathcal{T}_{\pi_t}$) and the compliance ($\mathbf{C}_{\pi_t}$) at $\vec{X}^{SF}$ (line 3).

**Algorithm 3** Recursive vessels compliance graph matching (VCGM) $\mathcal{G}^S, \mathcal{G}^T$

```
1: $\pi_{iGPR} \leftarrow \{s_1 \leftrightarrow t_1, ..., s_K \leftrightarrow t_K\}$        ▷ iGPR matching initialization
2: function recursiveGraphMatchingVCGM($\pi_t$)
3:     $\mathcal{T}_{\pi_t}, \mathbf{C}_{\pi_t}$ = simulationVascularizedFEM($\pi_t, \mathcal{G}^S, \mathcal{G}^T$)
4:     $\mathbf{P}$ = FindCandidatesCompliance($\mathcal{T}_{\pi_t}, \mathbf{C}_{\pi_t}$)
5:     $S_{\pi_t}$ = QualityScore($\mathcal{T}_{\pi_t}$ )
6:     if $|\mathbf{P}| \neq 0$ then
7:         for $\mathcal{P}_{i^*}$ in RandomPermutation($\mathbf{P}$) do
8:             for $\mathbf{t}_{j^*}$ in RandomPermutation($\mathcal{P}_{i^*}$) do
9:                 $\pi_{t+1} \leftarrow \pi_t \cup \{\mathbf{s}_{i^*} \leftrightarrow \mathbf{t}_{j^*}\}$
10:                RecursiveGraphMatchingVCGM($\pi_{t+1}$)
11: $\pi^* = \arg\max \{S_{\pi_{iGPR}}, ..., S_{\pi_T}\}$

12: function FindCandidatesCompliance($\mathcal{T}_{\pi_t}, \mathbf{C}_{\pi_t}$)
13:     for $\mathbf{s}_i$ in $\vec{X}^{SF}$ do
14:         $\mathcal{B}_i = \{\forall\, \mathbf{t}_j \in \vec{X}^{TF} :\ | M^2_{comp}(\mathcal{T}_{\pi_t}(\mathbf{s}_i),\ \mathbf{t}_j) < MC_{TH} \vee |\mathcal{T}_{\pi_t}(\mathbf{s}_i) - \mathbf{t}_j| < E_{TH}\}$
15:         $\mathcal{P}_i = \{\mathbf{t}_j : \mathbf{t}_j \in |\mathbf{G}_{t_j} - \mathbf{G}_{s_i}| < (G_{TH})(\mathbf{G}_{s_i}) \wedge \mathbf{t}_j \in \mathcal{B}_i\}$
16:     $\mathbf{P} = \arg\min_i \{|\mathcal{P}_i|\}$ for $|\mathcal{P}_i| \neq 0$
```

Here, the $\mathcal{T}_{\pi_t}$ and $\mathbf{C}_{\pi_t}$ replace, respectively, the GPR mean and covariance from Algorithm 1, removing completely this dependency.

To find the next matching candidates $\mathbf{P}$ (line 4) the Mahalanobis distance

$$M^2_{comp} = (\mathcal{T}_{\pi_t}(\mathbf{s}_i) - \mathbf{t}_j)^T (\mathbf{C}^i_{\pi_t})^{-1} (\mathcal{T}_{\pi_t}(\mathbf{s}_i) - \mathbf{t}_j) \tag{V.4}$$

computed with the compliance $\mathbf{C}_{\pi_t}$ is used. Here, $M^2_{comp}$ is equivalent to the virtual work needed to add a candidate match. The biomechanical simulation is important because $\mathcal{T}_{\pi_t}$ transforms the source bifurcations close to the target ones and the beam model correctly simulates the deformation along the graph edges. In addition, the compliance tensor filters candidates that require high energy to match. Especially, the beam model introduces additional stiffness and anisotropy that leads to smaller compliance in thicker vessels. This reduces the bounded region of these rigid vessels while keeping higher compliance and bounded regions on thin flexible vessels. These compliance-based bounded regions are shown in Fig. V.6.b.

For each free bifurcation in $\vec{X}^{SF}$, the bounded region candidates ($\mathcal{B}_i$) are the target free bifurcations ($\vec{X}^{TF}$) within Mahalanobis ($MC_{TH}$) or strict euclidean ($E_{TH}$) distance thresholds (line 14). From here, the algorithm is again similar to BGM.

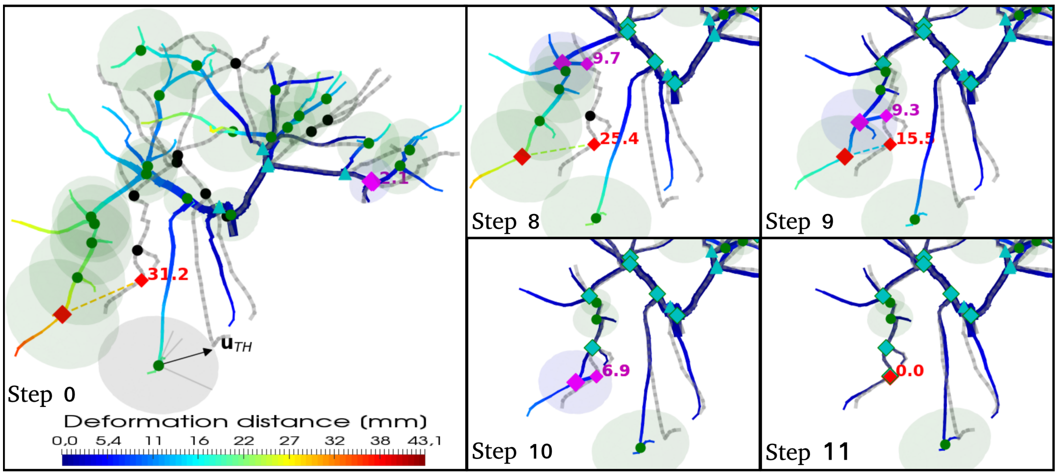

**Incremental graph matching hypotheses generation**

**Figure V.7:** The source and target graphs are color-coded with the registration error magnitude and in gray, respectively. In the first recursive step, the $\pi_{iGPR}$ initialization (cyan triangles matches) and the FE simulation determine the most flexible bifurcation (inside the gray bounded region). This bifurcation's compliance $\mathbf{C}_{max}$ and the maximum incremental displacement $\mathbf{u}_{TH}$ define the $MC_{TH}$ threshold. Then, every recursive step adds a new match (connected diamonds in pink with its displacement magnitude $|\mathcal{T}_{\pi_t}(\mathbf{s}_{i^*}) - \mathbf{t}_{j^*}|$) to the current hypothesis. This incremental hypotheses generation progressively reduces the source graph's registration error, including the bifurcations match ($\mathbf{s}_{maxDef} \leftrightarrow \mathbf{t}_{maxDef}$) initial maximum deformation ($|\mathcal{T}_{\pi_{iGPR}}(\mathbf{s}_{maxDef}) - \mathbf{t}_{maxDef}|$) of the connected diamonds match in red.

## Setting the Mahalanobis compliance threshold

In BGM, the covariance Mahalanobis threshold ($M_{TH}$) specifies a level of confidence given by the GPR covariance. In VCGM, the $MC_{TH}$ threshold represents an upper bound of the work needed to match bifurcations. The optimal $MC_{TH}$ depends on the FE model, deformation magnitude, initialization and incremental hypotheses generation (depicted in Fig. V.7).

We propose to define $MC_{TH}$ as a function of the maximum incremental displacement's magnitude ($U_{TH} = |\mathbf{u}_{TH}|$):

$$MC_{TH} = f(U_{TH}) = (\mathbf{u}_{TH}^T (\mathbf{C}_{max})^{-1} \mathbf{u}_{TH})^{1/2}, \tag{V.5}$$

where $\mathbf{C}_{max}$ is obtained using the FE simulation at the initialized stage ($\pi_{iGPR}$) by selecting the bifurcation whose compliance ellipsoid volume is the maximum, i.e. the most "flexible" bifurcation. Since the free bifurcations can move in any direction, the maximum incremental displacement $\mathbf{u}_{TH} = (U_{TH}/\sqrt{3})(\hat{e}_1 + \hat{e}_2 + \hat{e}_3)$ is assumed isotropic with respect to the eigenvectors ($\hat{e}_1, \hat{e}_2, \hat{e}_3$) of $\mathbf{C}_{max}$.

The $U_{TH}$ threshold remains dependent on the incremental hypotheses generation and the deformation magnitude. Still, it is assumed that $U_{TH}$ is smaller than the initial maximum match's deformation ($|\mathcal{T}_{\pi_{iGPR}}(\mathbf{s}_{maxDef}) - \mathbf{t}_{maxDef}|$) and bigger than the new matches' displacements ($|\mathcal{T}_{\pi_t}(\mathbf{s}_{i^*}) - \mathbf{t}_{j^*}|$). Where the bifurcations matches with maximal initial deformation ($\mathbf{s}_{maxDef} \leftrightarrow \mathbf{t}_{maxDef}$) and the ones added each matching step ($\mathbf{s}_{i^*} \leftrightarrow \mathbf{t}_{j^*}$) are depicted in Fig. V.7. In practice, setting $U_{TH} = 14\ mm$ (about 40% of the largest bifurcation's deformation) allowed to match successfully several experiments, which have a wide range of initial maximum displacements.

Since $MC_{TH}$ is larger than required in some recursive steps of the algorithm, using a constant $U_{TH}$ unnecessarily increases the search space. ACGM alleviates this issue.

### V.3.2 Matching based on adaptive Mahalanobis distance (ACGM)

In VCGM, only the bifurcations that require less than a given amount of work, bounded by the constant compliance Mahalanobis threshold ($MC_{TH}$), are matched. Although the compliance tensor filters some incorrect matches, this constant upper bound unnecessarily increases the search space. This is because the incremental matching (in Fig. V.7) does not always need the constant upper bound at every recursive step.

Instead of setting a constant threshold, ACGM uses the range $[MC_{Low}, MC_{High}]$. As presented in the Algorithm 4, the rigid-to-soft approach starts by adding the bifurcation matches that require the least amount of work ($MC_{Low}$) and when no more matches are found, instead of exploring other alternative hypotheses, the work bound is gradually increased. Hence, the matches that require more work are gradually added until a maximum allowed work ($MC_{High}$) is reached (lines 6 to 9).

In most cases, the rigid-to-soft strategy finds an appropriate set of correspondences before exploring an alternative matching path. Thus, when the exploration of the first matching path is finished, $MC_{High}$ is reduced to save time (line 14).

$MC_{High}$ can be set higher than the optimal value (overestimated) to guarantee that it covers a wide range of deformation, scale, or incremental exploration dependencies. Thanks to the rigid-to-soft approach, an overestimated $MC_{High}$ produces only a small increase in computation time.

When there are outlier matches that require less work to be matched than the correct matches, $MC_{Low}$ is a critical parameter. In this specific case, $MC_{Low}$ should be large enough to include the correct matches.

**Algorithm 4** Recursive Adaptive compliance graph matching (ACGM) $\mathcal{G}^S, \mathcal{G}^T$

```
$\pi_{iGPR} \leftarrow \{\mathbf{s}_1 \leftrightarrow \mathbf{t}_1, ..., \mathbf{s}_K \leftrightarrow \mathbf{t}_K\}$        ▷ **iGPR matching initialization**
**function** RECURSIVEGRAPHMATCHINGACGM($\pi_t$)
    $\mathcal{T}_{\pi_t}, \mathbf{C}_{\pi_t}$ = **simulationVascularizedFEM**($\pi_t, \mathcal{G}^S, \mathcal{G}^T$)
    $S_{\pi_t}$ = QualityScore($\mathcal{T}_{\pi_t}$ )
    $MC_{\pi_t} = MC_{Low}$
    **while** $MC_{\pi_t} < MC_{High} \wedge |\mathbf{P}| = 0$ **do**
        $\mathbf{P}$ = **FindCandidatesCompliance**($\mathcal{T}_{\pi_t}, \mathbf{C}_{\pi_t}$)
        $MC_{\pi_t} = MC_{\pi_t} + (MC_{High} - MC_{Low})/6$
    **if** $|\mathbf{P}| \neq 0$ **then**
        **for** $\mathcal{P}_{i^*}$ in RandomPermutation($\mathbf{P}$) **do**
            **for** $\mathbf{t}_{j^*}$ in RandomPermutation($\mathcal{P}_{i^*}$) **do**
                $\pi_{t+1} \leftarrow \pi_t \cup \{\mathbf{s}_{i^*} \leftrightarrow \mathbf{t}_{j^*}\}$
                RECURSIVEGRAPHMATCHINGACGM($\pi_{t+1}$)
            $MC_{High} = (MC_{High} + MC_{\pi_t})/2$

$\pi^* = \arg\max \{S_{\pi_{iGPR}}, ..., S_{\pi_T}\}$
```

#### Setting Mahalanobis compliance threshold range for ACGM method

ACGM also uses Eq. V.5 to define the range $[MC_{Low}, MC_{High}]$ as a function of $[U_{Low}, U_{High}]$. The initialization, FE model and $U_{Low}$ help to define a correct $MC_{Low}$. Therefore, even in the specific case of outliers that are not geodesic-filtered, $U_{Low}$ is a less critical parameter. $U_{High}$ is similar to $U_{TH}$, they indirectly depend on deformation and scale because of the incremental hypotheses generation. The advantage of $U_{High}$ is that it is overestimated to cover a wide range of cases without a high increase in computation time.

## V.4 Comparing BGM, VCGM and ACGM methods

Besides registering CBCT and CTA, this section also presents an experiment that augments intra-operative 3DUS with preoperative CTA vascular trees. All the biomechanical graph matching methods presented (BGM, VCGM and ACGM) are evaluated on both synthetic and real data.

### V.4.1 Experiments on synthetic data

To evaluate the methods, synthetic (target) graphs that resemble CBCT were generated from a real vascular graph which was segmented from a CTA image. First as done in Section IV.5.1, the original CTA graph was deformed using a realistic

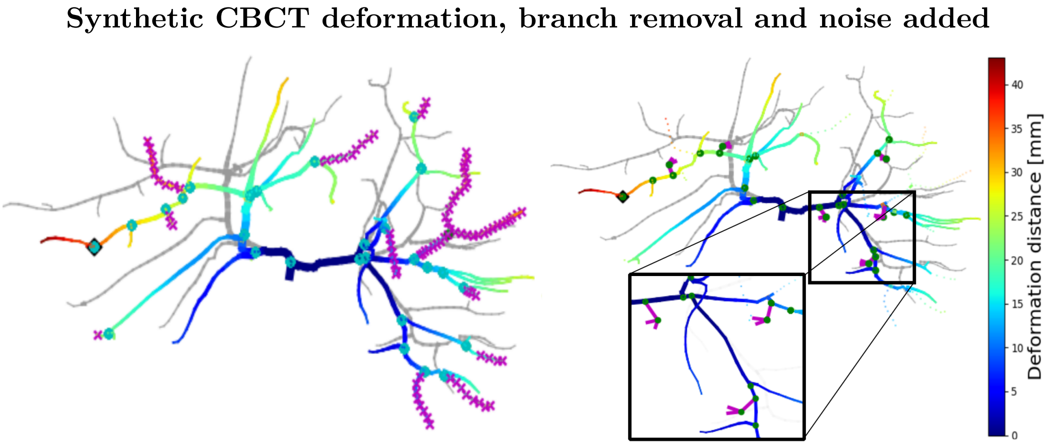

**Figure V.8:** The initial vascular graph (in gray) and the synthetic target graph (color-coded on deformation amplitude) are used for evaluation of the method. On the left, the magenta crosses represent the removed branches (40% of the initial graph). On the right, noisy branches (in magenta) are added to the deformed and reduced target graphs.

hyperelastic FE simulation that simulates the effect of the pneumoperitoneum on the liver. Again it is important to note that the FEM model used for matching is linear which makes the computation faster and uses a 1.5 kPa Young Modulus which is different from the ground truth simulations. Similarly, to resemble segmentation problems due to poor image quality, 40% random bifurcations were removed. Then, noisy bifurcations were added (50% or 80% of the bifurcations remaining from the previous step). An example of the synthetic data generated is shown in Fig. V.8. The original CTA graph and the deformed, reduced, and noisy target graphs were used to evaluate and compare the matching methods presented in this article. The target registration error (TRE) is computed in the complete original graph, including the 40% of vessels that were removed (therefore the TRE cannot reach zero in these experiments).

### Accuracy and search space size with increasing Mahalanobis thresholds

The first experiment evaluates the search space size and accuracy as a function of the bound region used. Matching was repeated 10 times per method with increasing Mahalanobis thresholds. $MC_{TH}$, $MC_{Low}$ and $MC_{High}$ were set without using Eq. V.5. These different matchings were only used to study the methods' Mahalanobis threshold sensitivity. Increasing thresholds were tested in one synthetic dataset (28 source and 16 target bifurcations) with 4 different initializations (named $E_n$ with $n \in [1, 4]$). Initialization $E_3$ has 6 matches while the other initializations have 5 matches, that is why $E_3$ explores fewer hypotheses. The three evaluated

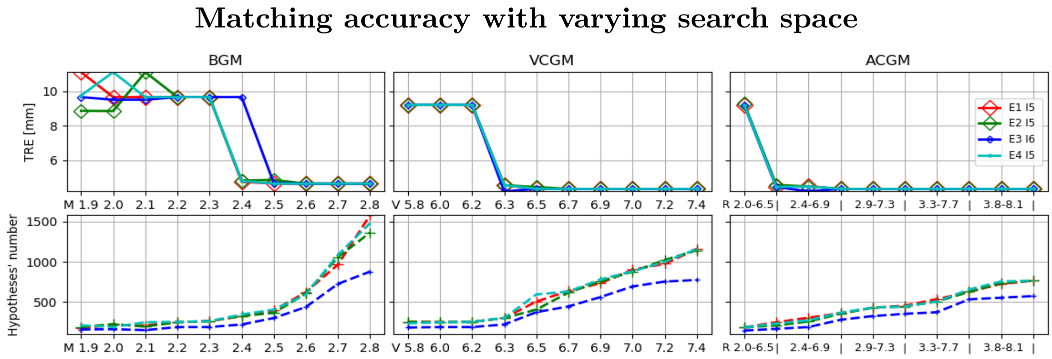

**Figure V.9:** Matching accuracy and search space size with increasing Mahalanobis thresholds in one synthetic dataset without noise. $MC_{TH}$ and $MC_{Low}$-$MC_{High}$ were set without using Eq. V.5 and are specified in the horizontal axis. The top row shows the TRE for each method with four different matching initializations ($E_n$) and the initial number of matches ($I_k$). Similarly, the bottom row shows the respective required number of hypotheses explored. The search space is better pruned with the VCGM and ACGM methods while the exploration highly increases with higher Mahalanobis thresholds in BGM.

methods use the same realistic Euclidean ($E_{TH} = 4\ mm$) and geodesic thresholds ($G_{TH} = 20\%$).

For every method, as shown in Fig. V.9, the TRE remains high when a small Mahalanobis threshold is used, but decreases as the threshold increases. However, if a high threshold is used the number of explored hypotheses and search time increases without a significant improvement of the TRE. Nevertheless, BGM's search space increase is steeper than for VCGM or ACGM. ACGM does the best pruning of the search space and has the best TRE results with less dependency on the Mahalanobis threshold used.

### Accuracy and search space size at the optimal Mahalanobis threshold

Using the previous experiment, every method is also compared at its optimal performance, i.e. the smallest Mahalanobis threshold at which the TRE reaches a minimum value. The mean and standard deviation for 4 different initializations at the optimal threshold are plotted in Fig. V.10. Similar experiments with added noisy bifurcations (50% and 80%) are also plotted. Without noise, the VCGM and ACGM methods are faster than BGM. When noise is added, the exploration space is highly increased with BGM. This case requires up to 40 minutes to do the matching and sometimes fails to find the correct match, increasing the mean TRE up to 5.8 mm. Differently, the compliance methods require, on average, less than 12 minutes. ACGM is the fastest with less than 8 minutes on average, and has 4.8 mm mean TRE.

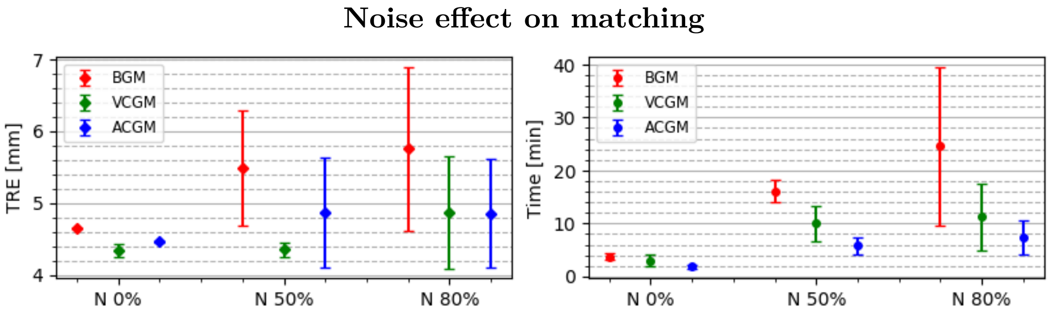

**Figure V.10:** TRE (left) and matching time (right) statistics obtained on 4 different initializations using the optimal Mahalanobis threshold (where $MC_{TH}$ and $MC_{Low}$-$MC_{High}$ were set without using Eq. V.5). Non-noisy graphs as well as graphs with bifurcations noise (50% and 80%) are considered in the study. The VCGM and ACGM methods have better TRE than BGM . When noise is added, these methods require less matching time than BGM. ACGM is the fastest method overall.

**Table V.1:** The graph bifurcations displacements statistics of the ten synthetic deformations.

| Deformation dataset | | D1 | D2 | D3 | D4 | D5 | D6 | D7 | D8 | D9 | D10 |
|---|---|---|---|---|---|---|---|---|---|---|---|
| Bifurcations displacements [mm] | $\mu$ | 10.2 | 12.1 | 13.9 | 13.5 | 8.6 | 11.6 | 14.8 | 12.2 | 9.0 | 11.0 |
| | $\sigma$ | 5.9 | 6.8 | 8.5 | 8.1 | 6.9 | 7.3 | 9.4 | 6.9 | 5.0 | 6.8 |
| | max | 21.2 | 24.7 | 31.3 | 29.2 | 26.7 | 25.1 | 35.6 | 25.8 | 17.7 | 23.9 |

For the 50% noise case in Fig. V.10, ACGM is more sensitive to noise than VCGM because $MC_{min}$ was set without using Eq. V.5. Setting a correct $MC_{min}$ is hard in the presence of noise that cannot be filtered with the geodesic constraint. This specific situation is an ACGM's limitation that was overcome when Eq. V.5 was used to define $MC_{min}$ in the following experiments.

### Synthetic deformations using the same matching parameters

Ten different deformations were generated using different pressure, Young's modulus and gravity orientation (to simulate subject in supine or flank position). Also, a craniocaudal force simulated different respiratory phases. These deformations are summarized in Table V.1 with statistics of the bifurcations' displacements. As in the previous experiments, the graphs have 40% branch removal and two levels of noisy bifurcations added.

Each method uses constant parameters to match all different synthetic datasets deformations. With BGM, the optimal $M_{TH}$ depends on the deformation magnitude and the noise, therefore being potentially difficult to set in clinical scenarios where no information of the deformation is *a priori* known. For this reason, op-

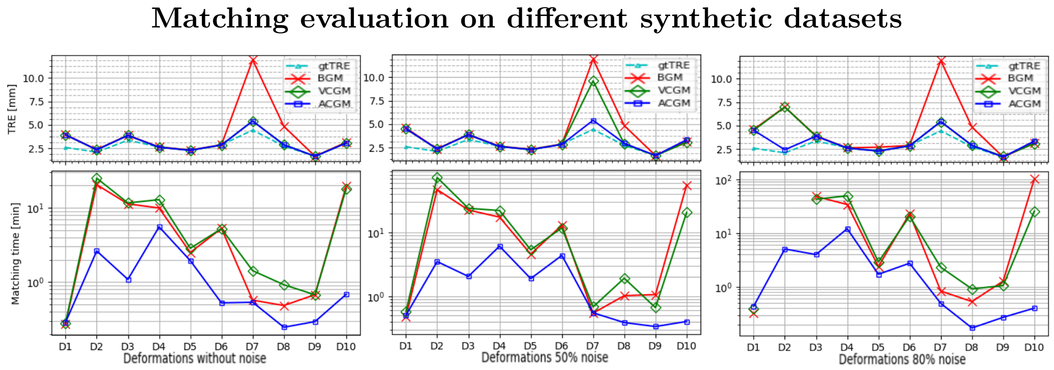

**Figure V.11:** The TRE and the matching time (in logarithmic scale) are evaluated for the three matching methods on ten different deformations using constant covariance Mahalanobis ($M_{TH}$) and maximum exploration displacement thresholds ($U_{TH}$, $U_{Low}$ and $U_{High}$). Each plot has the results of graphs with bifurcations noise (50% and 80%) and without it. The reference TRE (2.76±0.73 (4.42) mm) is computed with the ground truth bifurcations matches and shown in cyan.

timal threshold ($M_{TH} = 2.6$) found from the previous experiments is used. This threshold, using a cumulative chi-squared distribution, represents a 97% confidence region.

For the VCGM and ACGM methods, the parameters selection is simplified since the $MC_{TH}$ takes into account the FE model and the initialization. Thus, the only parameters to set are the maximum incremental displacement magnitudes. Given that the compliance methods are not too sensitive to these parameters, approximate values are sufficient. VCGM uses $U_{TH} = 14\ mm$, whereas ACGM uses $U_{Low} = 9\ mm$ and $U_{High} = 15\ mm$ to define $[MC_{Low}, MC_{High}]$.

The Fig. V.11 presents the matching time and the TRE measured with synthetic ground truth data of each experiment. ACGM has the same or better (in some cases of deformations D2, D7 and D8) TRE and is faster than the other methods.

Table V.2 summarizes the results of the ten deformations at each level of noise. Without noise, the average matching time of ACGM is 1.4 minutes, while it is more than 7 minutes with the other methods. Given that BGM fails to find all the correct matchings, the average TRE is 0.8 mm worse than the other methods. Adding 50% noise, the average matching time of ACGM only increases to two minutes, while it reaches 16 minutes with the other methods. With 80% noise added, the trend is clear. The average matching time of ACGM only increases to 2.7 minutes, while it reaches 23 minutes with BGM. The noise highly affects BGM, with a TRE increasing to 4.5 mm because it did not complete all the experiments as some exhausted the computer RAM memory available. ACGM maintains the best TRE result even with noise.

**Table V.2:** Matching statistics for ten synthetic deformations using constant covariance Mahalanobis ($M_{TH}$) and maximum incremental displacement ($U_{TH}$, $U_{Low}$ and $U_{High}$) thresholds.

| Noise | Without | | 50% | | 80% | |
|---|---|---|---|---|---|---|
| Method | TRE (max) [mm] | Time (max) [min] | TRE (max) [mm] | Time (max) [min] | TRE (max) [mm] | Time (max) [min] |
| BGM | 3.9± 2.8 (11.9) | 7.1± 7.4 (20.4) | 4.0± 2.8 (11.9) | 16.3± 19.1 (55.5) | 4.5± 2.9 (11.9) | 23.7± 32.4 (102.4) |
| VCGM | 3.1± 1.0 (5.4) | 7.9± 8.1 (24.9) | 3.5± 2.2 (9.6) | 16.1± 21.0 (73.1) | 3.6± 1.5 (7.0) | 16.3± 18.3 (49.7) |
| ACGM | 3.1± 1.0 (5.4) | 1.4± 1.6 (5.5) | 3.2± 1.1 (5.4) | 2.0± 1.9 (6.1) | 3.2± 1.1 (5.4) | 2.7± 3.5 (12.1) |

The maximum incremental displacement range $[U_{Low}, U_{High}]$ simplifies the correct setting of the compliance Mahalanobis thresholds. This allowed to use constant parameters ($U_{Low}$ and $U_{High}$) to match correctly a diverse set of synthetic deformations, making ACGM very robust and efficient.

### V.4.2 Experiments on real data

From the two porcine liver datasets (PA and PB), each dataset has one preoperative CTA image and one intra-operative CBCT image which was acquired under large deformation. In both modalities the portal vein is visible and from each modality a graph is extracted as indicated in Chapter III. It is important to notice that the CBCT image has fewer portal vessel branches visible than the CTA and several false branches were segmented due to noise (as shown in Fig. I.5 and Section III.3).

The portal veins graphs are matched to register the CTA data onto the CBCT to augment it. For instance, the hepatic vein is not visible in the CBCT and fusing it from the CTA is clinically useful. The number of CT/CBCT portal vein bifurcations is for PA=60/47 and PB=39/36 as shown in Table III.2. The number of bifurcations is similar in both modalities because of CBCT noise, there are several false bifurcations (most of the non-matched yellow cubes in the second row of Fig. V.12). The TRE is computed using reliable and unambiguous manually selected landmarks (37 for PA, while 22 for PB), as described in IV.5.2.

The Table V.3 presents the registration results for each dataset. First, using the matches obtained with the iGPR initialization, the rigid RE quantifies the nonlinear deformation magnitude. Similarly, the first row of Fig. V.12 depicts this deformation. From this iGPR initialization, matching was repeated 10 times per method with increasing Mahalanobis thresholds to find the optimal. All these matchings are not needed during a normal registration and are only used to provide a meaningful comparison. On average for the real datasets, ACGM has 2.34 mm and 0.58 mm better RE than BGM and VCGM, respectively. Moreover, ACGM is 43.4 and 18.05 minutes faster than BGM and VCGM, respectively. ACGM is about 12 times faster than BGM and significantly improves the RE. While the RE

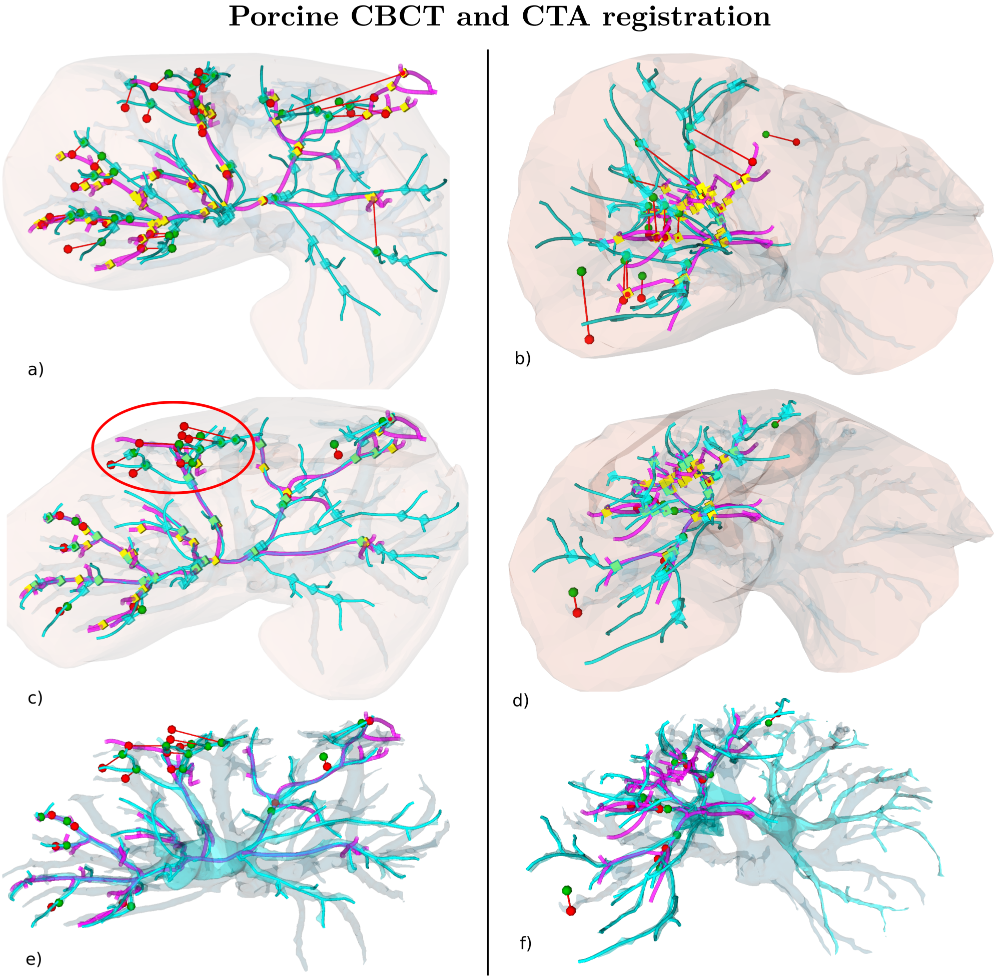

**Figure V.12:** The target CBCT (in pink) and source CTA (in cyan) portal vein graphs are rendered with tubular structures. The graph nodes (bifurcations) are shown as cubic markers (in yellow for the target, cyan for the source and green for the matched). The augmented hepatic vein, which was only visible in the CTA image, is in transparent blue behind the portal veins graphs. In the left and right columns are the PA and PB porcine datasets, respectively. The first row shows the 37 (for PA) and 22 (for PB) target evaluation landmarks (red spheres). It also shows the corresponding connected source landmarks (green spheres) and the liver structures rigidly aligned. These depict the large intra-operative non-linear deformation. The second and third row show the result of ACGM after the fine biomechanical matching fineBGM. They also show the 16 (for PA) and 11 (for PB) evaluation landmarks with an error larger than 3 mm. The third row shows the transformed source portal vein used for matching (in cyan), instead of the augmented liver.

**Table V.3:** Matching results for the BGM, VCGM and ACGM with a rigid initialization as deformation reference.

| Porcine dataset | Matching Method | Number of matches | RE [mm] $\mu \pm \sigma$(max) | time [min] |
|---|---|---|---|---|
| PA<br>37 landmarks | iGPR$_{Rigid}$ | 6 | 9.46±11.93 (65.3) | 2.1 |
| | BGM | 20 | 5.38±9.76 (58.4) | 39.3 |
| | VCGM | 22 | 4.63±4.76 (20.8) | 8.5 |
| | ACGM | 22 | 4.67±4.76 (21.1) | 1.1 |
| PB<br>22 landmarks | iGPR$_{Rigid}$ | 4 | 13.71±8.10 (33.6) | 0.42 |
| | BGM | 11 | 7.61±7.34 (25.1) | 55.6 |
| | VCGM | 15 | 4.84±3.56 (15.3) | 35.7 |
| | ACGM | 15 | 3.71±2.23 (7.6) | 7.0 |

difference in between the compliance methods is small, ACGM is much faster than VCGM.

Globally, ACGM correctly registers the two trees, except for few leaf vessels inside the red ellipse in Fig. V.12c. These few vessels are not well transformed because the corresponding bifurcations are missing in the target segmentation. These errors can be solved after the coarse bifurcation matching presented here, by using the end points of vessels together with the fine matching to improve the registration of high deformation edges.

### Influence of the segmentation of the vessels

Different pre-processing parameters are used to obtain four sets of graphs from a partial side of the *PA* dataset. Since only a partial side was used, the RE was evaluated only in 28 landmarks (two inserted tumors, 13 distinctive points and 13 bifurcations). Using these graphs sets, the influence of the pre-processing steps on the matching methods is studied.

As before, the optimal Mahalanobis threshold per method was searched from ten different increasing thresholds matchings. The second part of Table V.4 shows the optimal result of each method. For a majority of experiments, ACGM was faster, maintaining or even improving the RE. Only in experiment C (4th column of Table V.4), the ACGM matching time was about the same as for BGM. However, here the ACGM maximum RE is 3.4 mm better than for BGM.

The third part of Table V.4 shows the results obtained with the highest Mahalanobis thresholds used. From the optimal threshold to the highest used, BGM increases the 4 segmentations matching time an average of 28.3 minutes. While, the ACGM average matching time only increases 6.6 minutes.

The fourth part of Table V.4 shows the results using the $U_{TH}$ parameters to set the Mahalanobis thresholds. VCGM needs higher matching time than ACGM, up to the point that VCGM did not complete experiments C and D (marked with '-') as they exhausted the available RAM memory. ACGM using the $U_{TH}$ threshold selection is faster than the optimal $MC_{TH}$, the average for the 4 segmentations is 14.6 minutes faster. While, the $U_{TH}$ selection average RE is only 0.2 mm larger than the optimal MC threshold.

**Table V.4:** Matching results evaluated on 28 landmarks of four different preprocessed graphs (obtained from real porcine data PA).

| | A | $\lvert\vec{X}^S\rvert$=28, $\lvert\vec{X}^T\rvert$=27 | | B | $\lvert\vec{X}^S\rvert$=40, $\lvert\vec{X}^T\rvert$=27 | | C | $\lvert\vec{X}^S\rvert$=40, $\lvert\vec{X}^T\rvert$=33 | | D | $\lvert\vec{X}^S\rvert$=40, $\lvert\vec{X}^T\rvert$=34 | |
|---|---|---|---|---|---|---|---|---|---|---|---|---|
| match Func | Mah Th | RE [mm] $\mu \pm \sigma$ (max) | time [min] | Mah Th | RE [mm] $\mu \pm \sigma$ (max) | time [min] | Mah Th | RE [mm] $\mu \pm \sigma$ (max) | time [min] | Mah Th | RE [mm] $\mu \pm \sigma$ (max) | time [min] |
| optimal Mahalanobis threshold | | | | | | | | | | | | |
| BGM | 1.6 | 2.9± 1.7 (8.2) | 7.6 | 1.6 | 3.3± 2.2 (7.9) | 10.1 | 1.4 | 5.5± 4.1 (15.2) | 31.3 | 1.8 | 3.1± 2.3 (8.4) | 98.2 |
| VCGM | 4.4 | 2.9± 1.7 (8.3) | 6.3 | 4.5 | 3.3± 2.3 (8.4) | 5.0 | 3.4 | 5.4± 4.0 (14.9) | 6.2 | 4.2 | 3.0± 2.4 (8.1) | 32.4 |
| ACGM | 3.9-6.6 | 2.9± 1.7 (8.3) | 3.6 | 4.2-6.2 | 3.3± 2.2 (7.3) | 4.7 | 3.9-4.8 | 5.1± 3.4 (12.6) | 32.7 | 4.2-6.2 | 2.9± 2.2 (7.4) | 42.4 |
| Highest Mahalanobis threshold | | | | | | | | | | | | |
| BGM | 2.8 | 2.9± 1.7 (8.2) | 27.9 | 2.4 | 3.3± 2.2 (7.9) | 50.4 | 1.7 | 5.5± 3.9 (15.2) | 84.0 | 1.8 | 3.1± 2.3 (8.4) | 98.2 |
| VCGM | 7.0 | 2.9± 1.7 (8.3) | 21.9 | 6.4 | 3.3± 2.3 (8.4) | 18.9 | 4.1 | 5.5± 3.9 (14.8) | 27.6 | 4.5 | 3.0± 2.4 (8.1) | 45.6 |
| ACGM | 5.0-7.2 | 2.9± 1.7 (8.3) | 8.6 | 5.0-7.2 | 3.3± 2.2 (7.3) | 12.6 | 3.9-4.8 | 5.1± 3.4 (12.6) | 32.7 | 4.5-6.6 | 2.9± 2.2 (7.4) | 55.8 |
| Set MC threshold $U_{TH}$=16 mm, $U_{High}$=17 mm, and $U_{Low}$ 9mm | | | | | | | | | | | | |
| VCGM | 4.8 | 2.9± 1.7 (8.3) | 6.3 | 4.9 | 3.3± 2.4 (8.5) | 10.0 | 5.8 | -± - (-) | - | 4.9 | -± - (-) | - |
| ACGM | 2.7-5.1 | 2.9± 1.7 (8.3) | 0.6 | 2.8-5.2 | 3.4± 2.4 (8.6) | 1.24 | 3.3-6.2 | 5.5±3.9 (14.8) | 17.3 | 2.8-5.2 | 3.3± 2.1 (8.5) | 5.8 |

## Influence of geodesic distance accuracy

Using the graphs from previous experiments A and B, ten matchings are done to evaluate the geodesic influence. Fig. V.13 shows the results using increasing geodesic ($G_{TH}$) and constant Mahalanobis thresholds. When $G_{TH}$ is increased, the VCGM and ACGM methods do not increase the search time as much as BGM.

Due to image noise and pre-processing, the geodesic distance is inaccurate in real data. These inaccuracies represent a problem for BGM, because a small $G_{TH}$ does not allow to match inaccurate geodesic bifurcations (e.g. when $G_{TH}$<25% in Fig. V.13.b). An important advantage of the compliance methods is that the dependence on the geodesic constraint is reduced. This allows to use $G_{TH} = 40\%$ with ACGM, which in experiment B finds an extra correct match and reduces the RE to 2.9 mm.

## Porcine 3DUS and CTA registration

A pre-operative CTA is registered into one intra-operative 3DUS porcine image using the iGPR, BGM, VCGM and ACGM algorithms. These matching methods are evaluated with the RE measured from reliable manually selected landmarks which are visible in both modalities. These landmarks include distinctive vessel points

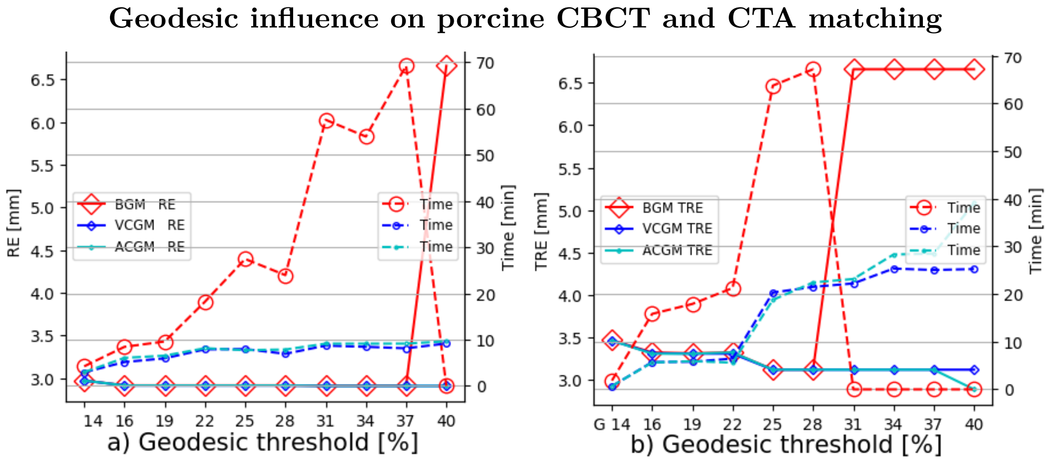

**Figure V.13:** Geodesic dependence of the RE and matching time on two different preprocessed graphs. BGM increases drastically the matching time with higher geodesic threshold ($G_{TH}$). While, the compliance methods depend less on the geodesic constraint.

and bifurcations (11 and 24 from the portal and hepatic portal veins, respectively). Two graphs datasets (PB$_{UP}$ and PB$_{UH}$ described in Section III.3.4) are used for the registration of these images, first matching the portal graphs dataset (PB$_{UP}$) and then the hepatic one (PB$_{UH}$).

The first part of the Table V.5 shows the registration results for the PB$_{UP}$ dataset. The CTA and 3DUS portal vein graphs of this dataset have 66 and 41 bifurcations, respectively. The pipeline starts with the iGPR matching, from this initialization the rigid RE and the alignment in the first column of Fig. V.14 depict the nonlinear deformation. Then from this iGPR initialization, matching was repeated 10 times per method with increasing Mahalanobis thresholds to find the optimal and only used to provide a meaningful comparison. ACGM is about 3 times faster than BGM and significantly improves the RE. While the ACGM has slightly better RE and 3 more bifurcations matched than VCGM, moreover is 2 minutes faster.

The second part of Table V.5 shows the registration results for PB$_{UH}$. The pre and intra-operative hepatic vein graphs of this dataset have 118 and 75 bifurcations, respectively. These graphs are matched using the previous portal vein ACGM results as initialization. The hepatic graphs matched with ACGM in only 3.17 minutes and reduce the RE to 4.71 mm. This combined portal and hepatic graphs matching result after the fineACGM alignment is shown in right column of Fig. V.14. Despite the large difference in field of view size, both pre and intra-operative graphs have similar number of bifurcation. This is because the 3DUS data graph is very noisy, as shown with the non matched hepatic noisy bifurcation (yellow cubes) in Fig. V.14.b. Besides the much smaller 3DUS field of view, the Fig. V.14.c shows

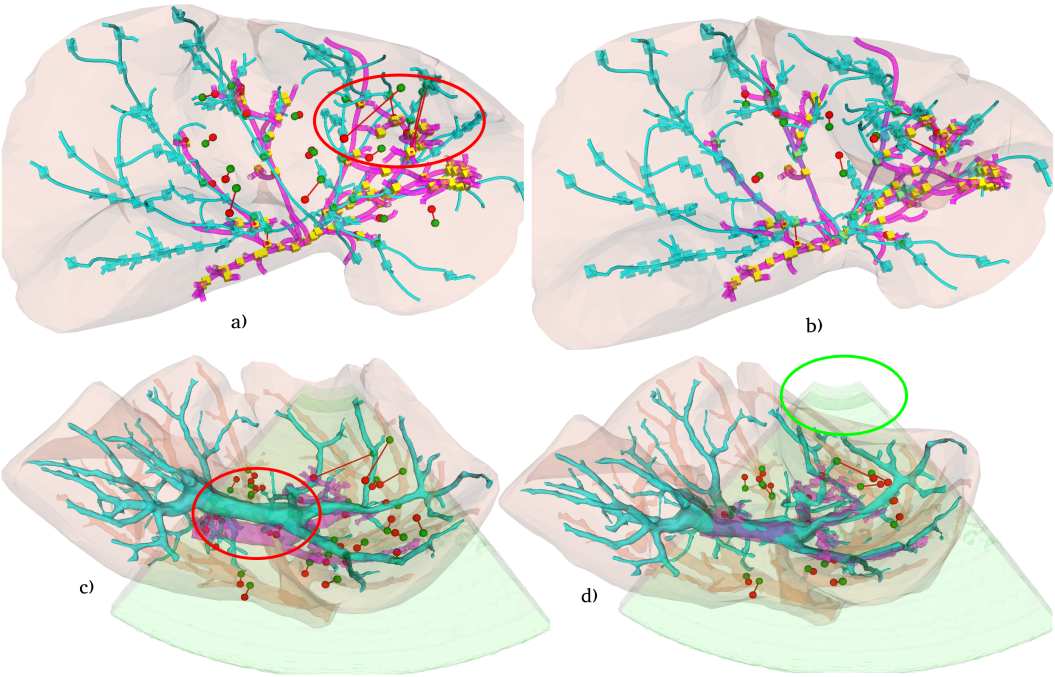
**Porcine 3DUS and CTA registration**

**Figure V.14:** The pre-operative CTA data is registered into the intra-operative 3DUS. Specifically, in the left and right columns are the rigid and the fine biomechanical matching fineACGM results, respectively. For both registrations, the 35 source (green spheres) and their corresponding connected target (red spheres) evaluation landmarks are shown. In the first row, the target US (in pink) and source CTA (in cyan) hepatic vein graphs (from $\text{PB}_{HU}$ dataset) are rendered with tubular structures. Also, the graph nodes (bifurcations) are shown as cubic markers (in yellow for the target, cyan for the source and green for the matched). In the second row, the US field of view (toroidal section in transparent green) and the target portal vein (in pink) are rendered. In the left column, the rigid registration depicts the large intra-operative non-linear deformation. Especially the area inside the red ellipses, in a) the large distance in between the evaluation landmarks and in c) the misaligned source portal vein. In the right column, the fineACGM matching depicts the reduction of landmarks intra-operative error. In b) the hepatic main vessels have good aliment despite the noisy bifurcations (mostly the non matched cubes in yellow). In d) deformation is accurately recovered as shown by realistic bending of the liver surface inside the US FoV (inside the green ellipse) and the good alignment of the pre and intra-operative portal main vessel.

**Table V.5:** Matching results for the BGM, VCGM and ACGM with a rigid initalialization as deformation reference.

| Porcine dataset | Matching Method | Number of matches | RE [mm] $\mu \pm \sigma$(max) | time [min] |
|---|---|---|---|---|
| $PB_{UP}$<br>35 landmarks | $iGPR_{Rigid}$ | 4 | 9.97 ± 4.53 (22.3) | 2.4 |
| | BGM | 8 | 7.22 ± 5.59 (28.4) | 39.2 |
| | VCGM | 9 | 6.84±5.52 (26.7) | 14.1 |
| | ACGM | 12 | 6.74±5.19 (24.3) | 12.7 |
| $PB_{UH}$ & $PB_{UP}$ | ACGM | 12 & 10 | 4.71 ± 4.03 (20.33) | 3.17 |

intra-operative large deformation due to open surgery 3DUS acquisition. Finally, the Fig. V.14.c shows how the ACGM matching overcomes this large intra-operative deformation.

It is hard to directly set the optimal Mahalanobis compliance thresholds. In VCGM, $U_{TH}$ removes the initialization and FE model dependency. However, it still depends on the deformation magnitude, incremental hypotheses generation and scale. A large $U_{TH}$ finds a correct match but increases the matching time. ACGM allows to overestimate $U_{High}$ to guarantee the correct solution and thanks to the rigid-to-soft approach it increases minimally the matching time. This allowed to set an approximate range that matched efficiently a wide variety of experiments. That's why ACGM is considered better than VCGM.

## Chapter VI

# General conclusion

## VI.1 Conclusion

Multi-modality deformable registration has the potential to augment non-visible anatomical structures in the intra-operative imaging which is a very important clinical need. For example, accurate registration could allow surgeons to reach small vessels and tumors during image guided procedures, like TACE.

Among the wide variety of registration methods, graph matching is a promising approach to properly fuse pre-operative data into a intra-operative highly deformed vascular images. As starting point, several real and synthetic experiments with the state-of-the-art GPR graph matching (Serradell et al., 2015) showed high computation time and low registration accuracy.

The two novel biomechanical graph matching methods proposed in this thesis progressively dealt with these limitations. First, BGM reduced the registration error (RE) by using an efficient FE simulation, however the matching time is still high specially in the common intra-operative presence of noise.

ACGM, the second contribution proposed, reduced the matching time while maintaining or even improving the RE, being up to one order of magnitude faster than BGM. ACGM was successful even under very large deformations while using an automatic segmentation method on two porcine liver CT/CBCT dataset. All the parameters of the algorithm are easy to set and can work correctly in a wide range of scenarios. This robustness was also demonstrated by adding several levels of noise and deformations in the synthetic datasets. The efficient ACGM method handles a large number of noise bifurcations, still maintaining the matching time within acceptable intra-operative constraints. This alleviates the need of low noise intra-operative automatic image segmentation.

These results are promising but further evaluation is required to validate the in-vivo applicability. First, the impact of different image acquisition conditions (resolution, contrast injection or artifacts) should be studied. Second, experiments on larger human datasets are required to prove the clinical importance. Although the clinical set-up is relatively common, collecting a large dataset with sufficient expert manual ground truth (to quantify registration error) requires significant amount of work.

This work paves the way towards augmented reality applications on highly deformable vascularized organs. Besides CBCT, ACGM can match other imaging modalities as long as enough vessels are correctly segmented. For example, ACGM was able to correctly register CTA into a good 3DUS acquisition, as the one presented in the experiments. The compliance filtering reduces the dependence on geodesic constraints, and this allowed to match noisier graphs with large topology variations.

## VI.2 Perspectives

There still remains non trivial registration error in some parts that lack bifurcations to guide the matching. This can be improved by matching end points into graph edges before or during the fine matching. According to the clinical gesture, other constraints (visible anatomical landmarks such as the liver surface) can be added as extra features to improve the registration.

It is not common to have complete good 3DUS acquisitions as the one matched in the experiments. The quality and the number of vessels visible in 3DUS is variable and its segmentation usually have disconnected branches. These issues highly increase the combinatory of the matching problem. Even if the hypotheses exploration is reduced with the efficient compliance-based search and ACGM perform better than other methods, the matching time of disconnected noisy graphs would still be incompatible with intra-operative constraints. The need of good 3DUS acquisitions for registration can be removed using a faster implementation of ACGM with parallel implementations and/or faster mechanical models (Brunet et al.). Besides been also very efficient, more complex elastic models (Brunet et al., 2019) could also be used to improve the registration quality.

# Bibliography

[Aja-Fernandez et Alberola-Lopez, 2006] S. Aja-Fernandez et C. Alberola-Lopez. On the estimation of the coefficient of variation for anisotropic diffusion speckle filtering. IEEE Transactions on Image Processing, vol. 15, no. 9, pages 2694–2701, 2006, ISSN 1057-7149.

[Andronache et al., 2008] A. Andronache, M. von Siebenthal, G. Székely et P. Cattin. Non-rigid registration of multi-modal images using both mutual information and cross-correlation. Medical image analysis, vol. 12, no. 1, pages 3–15, 2008.

[Atlanta Vascular and Vein Clinic, 2019] Atlanta Vascular and Vein Clinic. Transarterial Chemoebolization (TACE). `https://atlantavascularandveincenters.com/transarterial-chemoebolization-tace`, 2019, accessed: 2019-09-30.

[Aylward et al., 2003] S. R. Aylward, J. Jomier, S. Weeks et E. Bullitt. Registration and analysis of vascular images. International Journal of Computer Vision, vol. 55, no. 2-3, pages 123–138, 2003.

[Bano et al., 2013] J. Bano, S. A. Nicolau, A. Hostettler, C. Doignon, J. Marescaux et L. Soler. Registration of preoperative liver model for laparoscopic surgery from intraoperative 3d acquisition. In Augmented Reality Environments for Medical Imaging and Computer-Assisted Interventions, pages 201–210, Springer, 2013.

[Bapst et al., 2016] B. Bapst, M. Lagadec, R. Breguet, V. Vilgrain et M. Ronot. Cone beam computed tomography (CBCT) in the field of interventional oncology of the liver. Cardiovascular and interventional radiology, vol. 39, no. 1, pages 8–20, 2016.

[Bauer et Bischof, 2008] C. Bauer et H. Bischof. Edge Based Tube Detection for Coronary Artery Centerline Extraction. 2008.

[Bay et al., 2006] H. Bay, T. Tuytelaars et L. Van Gool. Surf: Speeded up robust features. In Computer vision–ECCV 2006, pages 404–417, Springer, 2006.

[Boltcheva et al., 2009] D. Boltcheva, M. Yvinec et J.-D. Boissonnat. Mesh generation from 3D multi-material images. In Int. Conf. MICCAI, pages 283–290, Springer, 2009.

[Bray et al., 2018] F. Bray, J. Ferlay, I. Soerjomataram, R. L. Siegel, L. A. Torre et A. Jemal. Global cancer statistics 2018: GLOBOCAN estimates of incidence and mortality worldwide for 36 cancers in 185 countries. CA: a cancer journal for clinicians, vol. 68, no. 6, pages 394–424, 2018.

[Brunet et al.] J.-N. Brunet, V. Magnoux, B. Ozell et S. Cotin. Corotated meshless implicit dynamics for deformable bodies. In Computer Science Research Notes.

[Brunet et al., 2019] J.-N. Brunet, A. Mendizabal, A. Petit, N. Golse, E. Vibert et S. Cotin. Physics-based Deep Neural Network for Augmented Reality during Liver Surgery. 2019.

[Burkard et al., 2009] R. E. Burkard, M. Dell'Amico et S. Martello. Assignment problems. Springer, 2009.

[Charnoz et al., 2005] A. Charnoz, V. Agnus, G. Malandain, L. Soler et M. Tajine. Tree matching applied to vascular system. In International Workshop on Graph-Based Representations in Pattern Recognition, pages 183–192, Springer, 2005.

[Chen et al., 2015] E. C. Chen, A. J. McLeod, J. S. Baxter et T. M. Peters. Registration of 3D shapes under anisotropic scaling. International journal of computer assisted radiology and surgery, vol. 10, no. 6, pages 867–878, 2015.

[Cho et Lee, 2012] M. Cho et K. M. Lee. Progressive graph matching: Making a move of graphs via probabilistic voting. In 2012 IEEE Conference on Computer Vision and Pattern Recognition, pages 398–405, IEEE, 2012.

[Cho et al., 2010] M. Cho, J. Lee et K. M. Lee. Reweighted Random Walks for Graph Matching. In Proceedings of the 11th European Conference on Computer Vision: Part V, ECCV'10, pages 492–505, Springer-Verlag, Berlin, Heidelberg, 2010, ISBN 3-642-15554-5, 978-3-642-15554-3.

[Collins et al., 2017] J. A. Collins, J. A. Weis, J. S. Heiselman, L. W. Clements, A. L. Simpson, W. R. Jarnagin et M. I. Miga. Improving registration robustness for image-guided liver surgery in a novel human-to-phantom data framework. IEEE transactions on medical imaging, vol. 36, no. 7, pages 1502–1510, 2017.

[Cotin et al., 2000] S. Cotin, H. Delingette et N. Ayache. A hybrid elastic model for real-time cutting, deformations, and force feedback for surgery training and simulation. The Visual Computer, vol. 16, no. 8, pages 437–452, 2000.

[Cour et al., 2007] T. Cour, P. Srinivasan et J. Shi. Balanced graph matching. In Advances in Neural Information Processing Systems, pages 313–320, 2007.

[Courtecuisse et al., 2010] H. Courtecuisse, H. Jung, J. Allard, C. Duriez, D. Y. Lee et S. Cotin. GPU-based real-time soft tissue deformation with cutting and haptic feedback. Progress in biophysics and molecular biology, vol. 103, no. 2-3, pages 159–168, 2010.

[Debbaut et al., 2014] C. Debbaut, P. Segers, P. Cornillie, C. Casteleyn, M. Dierick, W. Laleman et D. Monbaliu. Analyzing the human liver vascular architecture by combining vascular corrosion casting and micro-CT scanning: a feasibility study. Journal of anatomy, vol. 224, no. 4, pages 509–517, 2014.

[Deng et al., 2010] K. Deng, J. Tian, J. Zheng, X. Zhang, X. Dai et M. Xu. Retinal fundus image registration via vascular structure graph matching. Journal of Biomedical Imaging, vol. 2010, page 14, 2010.

[Devroye et Kruszewski, 1995] L. Devroye et P. Kruszewski. A note on the Horton-Strahler number for random trees. Information Processing Letters, vol. 2, no. 56, pages 95–99, 1995.

[Duriez et al., 2006] C. Duriez, S. Cotin, J. Lenoir et P. Neumann. New approaches to catheter navigation for interventional radiology simulation. Computer Aided Surgery, vol. 11, no. 6, pages 300–308, 2006.

[Frankel et al., 2012] T. L. Frankel, R. K. G. Do et W. R. Jarnagin. Preoperative imaging for hepatic resection of colorectal cancer metastasis. Journal of gastrointestinal oncology, vol. 3, no. 1, page 11, 2012.

[Fuerst et al., 2014] B. Fuerst, W. Wein, M. Müller et N. Navab. Automatic ultrasound-MRI registration for neurosurgery using the 2D and 3D LC2 Metric. Med Image Anal, vol. 18, no. 8, pages 1312–1319, 2014, ISSN 13618423.

[Garcia Guevara et al., 2018] J. Garcia Guevara, I. Peterlik, M.-O. Berger et S. Cotin. Biomechanics-based graph matching for augmented CT-CBCT. IJCARS, 2018, ISSN 1861-6429.

[Garcia Guevara et al., 2019] J. Garcia Guevara, I. Peterlik, M.-O. Berger et S. Cotin. Elastic Registration Based on Compliance Analysis and Biomechanical Graph Matching. Annals of Biomedical Engineering, pages 1–16, 2019.

[Haouchine et al., 2015] N. Haouchine, S. Cotin, I. Peterlik, J. Dequidt, M. S. Lopez, E. Kerrien et M.-O. Berger. Impact of soft tissue heterogeneity on augmented reality for liver surgery. IEEE transactions on visualization and computer graphics, vol. 21, no. 5, pages 584–597, 2015.

[Haouchine et al., 2016] N. Haouchine, F. Roy, L. Untereiner et S. Cotin. Using Contours as Boundary Conditions for Elastic Registration during Minimally Invasive Hepatic In International Conference on Intelligent Robots and Systems, Daejeon, South Korea, 2016.

[Heinrich et al., 2012] M. P. Heinrich, M. Jenkinson, M. Bhushan, T. Matin, F. V. Gleeson, M. Brady et J. A. Schnabel. MIND: Modality independent neighbourhood descriptor for multi-modal deformable registration. Medical Image Analysis, vol. 16, no. 7, pages 1423–1435, 2012.

[Heiselman et al., 2017] J. S. Heiselman, L. W. Clements, J. A. Collins, J. A. Weis, A. L. Simpson, S. K. Geevarghese, T. P. Kingham, W. R. Jarnagin et M. I. Miga. Characterization and correction of intraoperative soft tissue deformation in image-guided laparoscopic liver surgery. Journal of Medical Imaging, vol. 5, no. 2, page 021,203, 2017.

[Heizmann et al., 2010] O. Heizmann, S. Zidowitz, H. Bourquain, S. Potthast, H.-O. Peitgen, D. Oertli et C. Kettelhack. Assessment of intraoperative liver deformation during hepatic resection: prospective clinical study. World journal of surgery, vol. 34, no. 8, pages 1887–1893, 2010.

[Iwazawa et al., 2013] J. Iwazawa, S. Ohue, N. Hashimoto, O. Muramoto et T. Mitani. Clinical utility and limitations of tumor-feeder detection software for liver cancer embolization. European journal of radiology, vol. 82, no. 10, pages 1665–1671, 2013.

[Jomier et Aylward, 2004] J. Jomier et S. R. Aylward. Rigid and deformable vasculature-to-image registration: A hierarchical approach. In International Conference on Medical Image Computing and Computer-Assisted Intervention, pages 829–836, Springer, 2004.

[Kim et al., 2012] P. N. Kim, D. Choi, H. Rhim, S. E. Rha, H. P. Hong, J. Lee, J.-I. Choi, J. W. Kim, J. W. Seo, E. J. Lee et al.. Planning ultrasound for percutaneous radiofrequency ablation to treat small ($<$ 3 cm) hepatocellular carcinomas detected on computed tomography or magnetic resonance imaging: a multicenter prospective study to assess factors affecting ultrasound visibility. Journal of Vascular and Interventional Radiology, vol. 23, no. 5, pages 627–634, 2012.

[Kingham et al., 2018] T. P. Kingham, L. M. Pak, A. L. Simpson, U. Leung, A. Doussot, M. I. D'Angelica, R. P. DeMatteo, P. J. Allen et W. R. Jarnagin. 3D image guidance assisted identification of colorectal cancer liver metastases not seen on intraoperative ultrasound: results from a prospective trial. HPB, vol. 20, no. 3, pages 260–267, 2018.

[Klein et al., 2008] S. Klein, U. A. Van Der Heide, I. M. Lips, M. Van Vulpen, M. Staring et J. P. Pluim. Automatic segmentation of the prostate in 3D MR images by atlas matching using localized mutual information. Medical physics, vol. 35, no. 4, pages 1407–1417, 2008.

[Krissian et al., 2000] K. Krissian, G. Malandain, N. Ayache, R. Vaillant et Y. Trousset. Model-Based Detection of Tubular Structures in 3D Images. Computer Vision and Image Understanding, vol. 80, no. 2, pages 130 – 171, 2000, ISSN 1077-3142.

[Lange et al., 2003] T. Lange, S. Eulenstein, M. Hünerbein et P.-M. Schlag. Vessel-based non-rigid registration of MR/CT and 3D ultrasound for navigation in liver surgery. Computer Aided Surgery, vol. 8, no. 5, pages 228–240, 2003.

[Lange et al., 2009] T. Lange, N. Papenberg, S. Heldmann, J. Modersitzki, B. Fischer, H. Lamecker et P. M. Schlag. 3D ultrasound-CT registration of the liver using combined landmark-intensity information. Int J Comput Assist Radiol Surg., vol. 4, no. 1, pages 79–88, 2009.

[Lehmann, 2007] G. Lehmann. Label object representation and manipulation with ITK. 2007.

[Leordeanu et Hebert, 2005] M. Leordeanu et M. Hebert. A Spectral Technique for Correspondence Problems using Pairwise Constraints. In International Conference of Computer Vision (ICCV), vol. 2, pages 1482 – 1489, 2005.

[Lindseth et al., 2013] F. Lindseth, T. Langø, T. Selbekk, R. Hansen, I. Reinertsen, C. Askeland, O. Solheim, G. Unsgård, R. Mårvik et T. A. N. Hernes. Ultrasound-based guidance and therapy. In Advancements and breakthroughs in ultrasound imaging, InTech, 2013.

[Lowe, 2004] D. G. Lowe. Distinctive image features from scale-invariant keypoints. International journal of computer vision, vol. 60, no. 2, pages 91–110, 2004.

[Luu et al., 2018] H. M. Luu, A. Moelker, S. Klein, W. Niessen et T. van Walsum. Quantification of nonrigid liver deformation in radiofrequency ablation interventions using image registration. Physics in Medicine & Biology, vol. 63, no. 17, page 175,005, 2018.

[Malbrain et al., 2016] M. L. Malbrain, Y. Peeters et R. Wise. The neglected role of abdominal compliance in organ-organ interactions. Critical Care, vol. 20, no. 1, page 67, 2016.

[Marchesseau et al., 2017a] S. Marchesseau, S. Chatelin et H. Delingette. Non linear Biomechanical Model of the Liver. In Biomechanics of Living Organs, edited by Y. Payan et J. Ohayon, page 602, Elsevier, 2017a.

[Marchesseau et al., 2017b] S. Marchesseau, S. Chatelin et H. Delingette. Nonlinear Biomechanical Model of the Liver. In Biomechanics of Living Organs, pages 243–265, Elsevier, 2017b.

[Martínez et al., 2015] J. Martínez, J. Dumas, S. Lefebvre et L.-Y. Wei. Structure and Appearance Optimization for Controllable Shape Design. ACM Trans. Graph., vol. 34, no. 6, pages 229:1–229:11, 2015, ISSN 0730-0301.

[Matl et al., 2017] S. Matl, R. Brosig, M. Baust, N. Navab et S. Demirci. Vascular image registration techniques: A living review. Medical Image Analysis, vol. 35, pages 1–17, 2017.

[Mauri et al., 2015] G. Mauri, L. Cova, S. De Beni, T. Ierace, T. Tondolo, A. Cerri, S. N. Goldberg et L. Solbiati. Real-time US-CT/MRI image fusion for guidance of thermal ablation of liver tumors undetectable with US: results in 295 cases. Cardiovascular and interventional radiology, vol. 38, no. 1, pages 143–151, 2015.

[Moccia et al., 2018] S. Moccia, E. De Momi, S. El Hadji et L. S. Mattos. Blood vessel segmentation algorithms-Review of methods, datasets and evaluation metrics. Computer methods and programs in biomedicine, vol. 158, pages 71–91, 2018.

[Moriconi et al., 2018] S. Moriconi, M. Zuluaga, H. Rolf Jäger, P. Nachev, S. Ourselin et M. Jorge Cardoso. Elastic Registration of Geodesic Vascular Graphs. In MICCAI 2018, pages 810–818, 2018.

[Morin et al., 2017] F. Morin, H. Courtecuisse, I. Reinertsen, F. Le Lann, O. Palombi, Y. Payan et M. Chabanas. Brain-shift compensation using intraoperative ultrasound and constraint-based biomechanical simulation. Medical image analysis, vol. 40, pages 133–153, 2017.

[Nam et al., 2011] W. H. Nam, D.-G. Kang, D. Lee, J. Y. Lee et J. B. Ra. Automatic registration between 3D intra-operative ultrasound and pre-operative CT images of the liver based on robust edge matching. Phys Med Biol., vol. 57, no. 1, page 69, 2011.

[Nesme et al., 2005] M. Nesme, Y. Payan et F. Faure. Efficient, Physically Plausible Finite Elements. In Eurographics 2005, Short papers, August, 2005, edited by J. Dingliana et F. Ganovelli, 2005.

[Oktay et al., 2013] O. Oktay, L. Zhang, T. Mansi, P. Mountney, P. Mewes, S. Nicolau, L. Soler et C. Chefd'hotel. Biomechanically Driven Registration of Pre- to Intra-Operative 3D Images for Laparoscopic Surgery. In Int. Conf. MICCAI, pages 1–9, Springer, 2013.

[Paul et al., 2015a] J. Paul, A. Chacko, M. Farhang, S. Kamali, M. Tavanania, T. Vogl et B. Panahi. Ultrafast cone-beam computed tomography: a comparative study of imaging protocols during image-guided therapy procedure. BioMed research international, vol. 2015, 2015a.

[Paul et al., 2015b] J. Paul, T. J. Vogl et A. Chacko. Detectability of hepatic tumors during 3D post-processed ultrafast cone-beam computed tomography. Physics in Medicine & Biology, vol. 60, no. 20, page 8109, 2015b.

[Peterlík et al., 2012a] I. Peterlík, C. Duriez et S. Cotin. Modeling and real-time simulation of a vascularized liver tissue. In International Conference on Medical Image Computing and Computer-Assisted Intervention, pages 50–57, 2012a.

[Peterlík et al., 2012b] I. Peterlík, C. Duriez et S. Cotin. Modeling and real-time simulation of a vascularized liver tissue. In Int. Conf. MICCAI, pages 50–57, Springer, 2012b.

[Peterlík et al., 2018] I. Peterlík, H. Courtecuisse, R. Rohling, P. Abolmaesumi, C. Nguan, S. Cotin et S. Salcudean. Fast elastic registration of soft tissues under large deformations. Medical image analysis, vol. 45, pages 24–40, 2018.

[Peters et Cleary, 2008] T. Peters et K. Cleary. Image-guided interventions: technology and applications. Springer Science & Business Media, 2008.

[Pinheiro et Kybic, 2018] M. A. Pinheiro et J. Kybic. Incremental B-spline deformation model for geometric graph matching. In ISBI, 2018.

[Pinheiro et al., 2017] M. A. Pinheiro, J. Kybic et P. Fua. Geometric graph matching using Monte Carlo tree search. IEEE Trans Pattern Anal Mach Intell., vol. 39, no. 11, pages 2171–2185, 2017.

[Plantefève et al., 2016] R. Plantefève, I. Peterlik, N. Haouchine et S. Cotin. Patient-Specific Biomechanical Modeling for Guidance During Minimally-Invasive Hepatic Surgery. Ann Biomed Eng., vol. 44, no. 1, pages 139–153, 2016.

[Plantefève et al., 2017] R. Plantefève, S. Kadoury, A. Tang et I. Peterlik. Robust Automatic Graph-Based Skeletonization of Hepatic Vascular Trees. In Intravascular Imaging and Computer Assisted Stenting, and Large-Scale Annotation of Biomedical Data and Expert Label Synthesis, pages 20–28, Springer, 2017.

[Przemieniecki, 1985] J. S. Przemieniecki. Theory of Matrix Structural Analysis. Dover, 1985.

[Ramos-Llorden et al., 2015] G. Ramos-Llorden, G. Vegas-Sanchez-Ferrero, M. Martin-Fernandez, C. Alberola-Lopez et S. Aja-Fernandez. Anisotropic diffusion filter with memory based on speckle statistics for ultrasound images. IEEE Transactions on Image Processing, vol. 24, no. 1, pages 345–358, 2015, ISSN 10577149.

[Rasmussen et Williams, 2006] C. Rasmussen et C. Williams. Gaussian processes for machine learning. MIT Press, 2006.

[Reaungamornrat et al., 2016] S. Reaungamornrat, T. De Silva, A. Uneri, S. Vogt, G. Kleinszig, A. J. Khanna, J.-P. Wolinsky, J. L. Prince et J. H. Siewerdsen. MIND demons: symmetric diffeomorphic deformable registration of MR and CT for image-guided spine surgery. IEEE transactions on medical imaging, vol. 35, no. 11, pages 2413–2424, 2016.

[Reinertsen et al., 2007] I. Reinertsen, M. Descoteaux, K. Siddiqi et D. L. Collins. Validation of vessel-based registration for correction of brain shift. Medical image analysis, vol. 11, no. 4, pages 374–388, 2007.

[Rivaz et al., 2015] H. Rivaz, S. J.-S. Chen et D. L. Collins. Automatic deformable MR-ultrasound registration for image-guided neurosurgery. Medical Imaging, IEEE Transactions on, vol. 34, no. 2, pages 366–380, 2015.

[Robben et al., 2012] D. Robben, D. Smeets, D. Ruijters, M. Hoffmann, L. Antanas, F. Maes et P. Suetens. Intra-patient non-rigid registration of 3D vascular cerebral images. In Workshop on Clinical Image-Based Procedures, pages 106–113, Springer, 2012.

[Robben et al., 2013] D. Robben, S. Sunaert, V. Thijs, G. Wilms, F. Maes et P. Suetens. Anatomical labeling of the Circle of Willis using maximum a posteriori graph matching. In International Conference on Medical Image Computing and Computer-Assisted Intervention, pages 566–573, Springer, 2013.

[Roche et al., 1998] A. Roche, G. Malandain, X. Pennec et N. Ayache. The correlation ratio as a new similarity measure for multimodal image registration. In Medical Image Computing and Computer-Assisted Intervention — MICCAI'98, edited by W. M. Wells, A. Colchester et S. Delp, pages 1115–1124, Springer Berlin Heidelberg, Berlin, Heidelberg, 1998.

[Ronot et al., 2016] M. Ronot, M. Abdel-Rehim, A. Hakimé, V. Kuoch, M. Roux, M. Chiaradia, V. Vilgrain, T. de Baere et F. Deschamps. Cone-beam CT angiography for determination of tumor-feeding vessels during chemoembolization of liver tumors: comparison of conventional and dedicated-software analysis. Journal of Vascular and Interventional Radiology, vol. 27, no. 1, pages 32–38, 2016.

[Rueckert et al., 1999] D. Rueckert, L. I. Sonoda, C. Hayes, D. L. Hill, M. O. Leach et D. J. Hawkes. Nonrigid registration using free-form deformations: application to breast MR images. IEEE transactions on medical imaging, vol. 18, no. 8, pages 712–721, 1999.

[Schneider et al., 2011] C. Schneider, J. Guerrero, C. Nguan, R. Rohling et S. Salcudean. Intra-operative "pick-up" ultrasound for robot assisted surgery with vessel extraction and registration: A feasibility study. pages 122–132, 2011, ISBN 9783642215032, ISSN 03029743.

[Serradell et al., 2011] E. Serradell, A. Romero, R. Leta, C. Gatta et F. Moreno-Noguer. Simultaneous correspondence and non-rigid 3D reconstruction of the coronary tree from single X-ray images. In 2011 International Conference on Computer Vision, pages 850–857, IEEE, 2011.

[Serradell et al., 2015] E. Serradell, M. A. Pinheiro, R. Sznitman, J. Kybic, F. Moreno-Noguer et P. Fua. Non-rigid graph registration using active testing search. IEEE Trans Pattern Anal Mach Intell., vol. 37, no. 3, pages 625–638, 2015, ISSN 01628828.

[Smeets et al., 2010] D. Smeets, P. Bruyninckx, J. Keustermans, D. Vandermeulen et P. Suetens. Robust matching of 3D lung vessel trees. In MICCAI workshop on pulmonary image analysis, vol. 2, pages 61–70, 2010.

[Smistad et Løvstakken, 2016] E. Smistad et L. Løvstakken. Vessel detection in ultrasound images using deep convolutional neural networks. In Deep Learning and Data Labeling for Medical Applications, pages 30–38, Springer, 2016.

[Smistad et al., 2014] E. Smistad, A. C. Elster et F. Lindseth. GPU accelerated segmentation and centerline extraction of tubular structures from medical images. Int J Comput Assist Radiol Surg., vol. 9, no. 4, pages 561–575, 2014, ISSN 18616429.

[Smithuis, 2014] R. Smithuis. CT contrast injection and protocols. `http://www.radiologyassistant.nl/en/p52c04470dbd5c/ct-contrast-injection-and-protocols.html`, 2014, accessed: 2019-04-01.

[Song et al., 2015] Y. Song, J. Totz, S. Thompson, S. Johnsen, D. Barratt, C. Schneider, K. Gurusamy, B. Davidson, S. Ourselin, D. Hawkes et al.. Locally rigid, vessel-based registration for laparoscopic liver surgery. International journal of computer assisted radiology and surgery, vol. 10, no. 12, pages 1951–1961, 2015.

[Sotiras et al., 2013] A. Sotiras, C. Davatzikos et N. Paragios. Deformable Medical Image Registration: A Survey. IEEE Transactions on Medical Imaging, vol. 32, no. 7, pages 1153–1190, 2013, ISSN 0278-0062.

[Speidel et al., 2011] S. Speidel, S. Roehl, S. Suwelack, R. Dillmann, H. Kenngott et B. Mueller-Stich. Intraoperative surface reconstruction and biomechanical modeling for soft tissue registration. In Proc. Joint Workshop on New Technologies for Computer/Robot Assisted Surgery, pages 0–0, 2011.

[Suh et al., 2010] J. W. Suh, D. Scheinost, X. Qian, A. J. Sinusas, C. K. Breuer et X. Papademetris. Serial nonrigid vascular registration using weighted normalized mutual information. In 2010 IEEE international symposium on biomedical imaging: from nano to macro, pages 25–28, IEEE, 2010.

[Suwelack et al., 2014] S. Suwelack, S. Röhl, S. Bodenstedt, D. Reichard, R. Dillmann, T. dos Santos, L. Maier-Hein, M. Wagner, J. Wünscher, H. Kenngott et al.. Physics-based shape matching for intraoperative image guidance. Medical physics, vol. 41, no. 11, page 111,901, 2014.

[Tacher et al., 2015] V. Tacher, A. Radaelli, M. Lin et J.-F. Geschwind. How I Do It: Cone-Beam CT during Transarterial Chemoembolization for Liver Cancer. Radiology, vol. 274, no. 2, pages 320–334, 2015.

[Torresani et al., 2008] L. Torresani, V. Kolmogorov et C. Rother. Feature correspondence via graph matching: Models and global optimization. In European Conference on Computer Vision, pages 596–609, Springer, 2008.

[Tortora et Derrickson, 2008] G. J. Tortora et B. H. Derrickson. Principles of anatomy and physiology. John Wiley & Sons, 2008.

[Torzilli et al., 2014] G. Torzilli, G. Costa et F. Botea. Exploring the Liver by Ultrasound Along its Anatomy. In Ultrasound-Guided Liver Surgery, pages 25–40, Springer, 2014.

[Tschirren et al., 2005] J. Tschirren, G. McLennan, K. Palágyi, E. A. Hoffman et M. Sonka. Matching and anatomical labeling of human airway tree. IEEE transactions on medical imaging, vol. 24, no. 12, pages 1540–1547, 2005.

[Tsutsumi et al., 2013] N. Tsutsumi, M. Tomikawa, M. Uemura, T. Akahoshi, Y. Nagao, K. Konishi, S. Ieiri, J. Hong, Y. Maehara et M. Hashizume. Image-guided laparoscopic surgery in an open MRI operating theater. Surgical endoscopy, vol. 27, no. 6, pages 2178–2184, 2013.

[van Pelt et al., 1989] J. van Pelt, R. W. H. Verwer et H. B. M. Uylings. Centrifugal-order distributions in binary topological trees. Bulletin of Mathematical Biology, vol. 51, no. 4, pages 511–536, 1989.

[Vercauteren et al., 2009] T. Vercauteren, X. Pennec, A. Perchant et N. Ayache. Diffeomorphic demons: Efficient non-parametric image registration. NeuroImage, vol. 45, no. 1, pages S61–S72, 2009.

[Verscheure et al., 2013] L. Verscheure, L. Peyrodie, A.-S. Dewalle, N. Reyns, N. Betrouni, S. Mordon et M. Vermandel. Three-dimensional skeletonization and symbolic description in vascular imaging: preliminary results. International journal of computer assisted radiology and surgery, vol. 8, no. 2, pages 233–246, 2013.

[Wein et al., 2008] W. Wein, S. Brunke, A. Khamene, M. R. Callstrom et N. Navab. Automatic CT-ultrasound registration for diagnostic imaging and image-guided intervention. Medical image analysis, vol. 12, no. 5, pages 577–585, 2008.

[Wittek et al., 2009] A. Wittek, T. Hawkins et K. Miller. On the unimportance of constitutive models in computing brain deformation for image-guided surgery. Biomech model mechanobiol., vol. 8, no. 1, pages 77–84, 2009.

[Yushkevich et al., 2016] P. A. Yushkevich, Y. Gao et G. Gerig. ITK-SNAP: An interactive tool for semi-automatic segmentation of multi-modality biomedical images. In 2016 38th Annual International Conference of the IEEE Engineering in Medicine and Biology Society (EMBC), pages 3342–3345, IEEE, 2016.

[Zhou et De la Torre, 2015] F. Zhou et F. De la Torre. Factorized graph matching. IEEE transactions on pattern analysis and machine intelligence, vol. 38, no. 9, pages 1774–1789, 2015.